

**The Autoignition Characteristics of Turbocharged Spark
Ignition Engines with Exhaust Gas Recirculation**

by
Jacob Elijah McKenzie

B.S., University of California, Berkeley (2009)
S.M., Massachusetts Institute of Technology (2012)

Submitted to the Department of Mechanical Engineering
in partial fulfillment of the requirements for the degree of

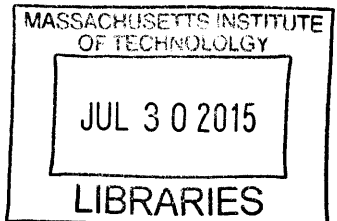
Doctor of Philosophy in Mechanical Engineering

at the
MASSACHUSETTS INSTITUTE OF TECHNOLOGY

June 2015

© Massachusetts Institute of Technology 2015. All rights reserved.

ARCHIVES



Signature redacted

Author
Department of Mechanical Engineering
May 10, 2015

Signature redacted

Certified by
Wai K. Cheng
Professor of Mechanical Engineering
Thesis Supervisor

Signature redacted

Accepted by
David Hardt
Professor of Mechanical Engineering
Chairman, Department Committee on Graduate Theses

The Autoignition Characteristics of Turbocharged Spark Ignition Engines with Exhaust Gas Recirculation

by

Jacob Elijah McKenzie

Submitted to the Department of Mechanical Engineering
on May 10, 2015, in partial fulfillment of the
requirements for the degree of
Doctor of Philosophy in Mechanical Engineering

Abstract

The societal demand for vehicles with high efficiency and low emissions has spurred considerable changes to the automotive internal combustion engine within the past decade. Reductions in the displacement volume and increases in maximum output per unit of displacement are among the characteristics adopted to meet the fuel economy targets of world governments. However, the extent to which these changes in engine configuration may be pursued in search of efficiency is limited by several fundamental phenomena. The intent of this research project is to investigate the modeling of one of these phenomena – the *autoignition* of an unburned portion of the air-fuel mixture – and a potential strategy intended to delay the occurrence of this frequently damaging type of combustion reaction. The autoignition abatement approach studied entails the recirculation of burned exhaust gasses which serve to dilute the air-fuel mixture and reduce maximum unburned gas temperatures.

Experimental testing was performed on two different types of exhaust gas recirculation (EGR) system – one which extracts exhaust gases from upstream of the catalytic converter and another which extracts gases from downstream – in order to determine if the changes in composition that occur across the catalyst affect the autoignition abatement characteristics of the recirculated exhaust. This testing indicated that differences between the alternative installations are dominated by changes in the flow dynamics of the exhaust system, with no definite changes attributable to compositional differences. An empirical method of predicting the occurrence of autoignition using experimental data was then developed based on an approach originally proposed by Livengood and Wu. Ignition delay correlations were developed that provide accurate autoignition prediction over a range of speeds, loads, air-fuel equivalence ratios and dilution rates. Additionally, a new statistical model for autoignition is proposed that captures the cycle-to-cycle variation in autoignition intensity and relates these variations to the thermodynamic state of the charge.

Thesis Supervisor: Wai K. Cheng
Title: Professor of Mechanical Engineering

Acknowledgments

I would like to thank the members of my thesis committee Professor Wai K. Cheng, Professor John B. Heywood and Professor William H. Green, for their insightful guidance and helpful analysis of the often complex but always interesting internal combustion engine. Thanks to the members of the Engine and Fuels Research Consortium: Borg-Warner, Chrysler, Ford Motor Company and General Motors who sponsored this research project and Rick Davis of GM, Tom Leone of Ford and David Roth of Borg-Warner who all provided invaluable feedback, suggestions and practical advice. Additional thanks go to my many colleagues at the Sloan Automotive Laboratory who have helped to make this work a success. Finally, my deepest appreciation goes to Emma Duong, whose support and love has made this document possible.

Contents

1 Introduction	21
1.1 Motivation	21
1.2 Background and Literature Review	23
1.3 Research Objectives	31
2 Experimental Apparatus and Procedures	33
2.1 Engine	33
2.2 Dynamometer and Auxiliary Systems	40
2.3 Data Acquisition and Processing	42
2.4 Experimental Procedures	44
3 Effects of EGR Source on Engine Operation	47
3.1 Recirculated Exhaust Composition	48
3.2 Thermo-physical Effects of EGR Source	51
3.3 Combustion Effects of EGR Source	56
4 Knock Onset and Intensity Correlation	75
4.1 Chemical and Empirical Autoignition Models	75
4.2 Computational Formulation of the Knock Integral and Ignition Delay	88
4.3 Stoichiometric Knock Integral Correlation	97
4.4 Non-Stoichiometric Knock Integral Correlation	103
4.5 Statistical Autoignition Model	110
5 Summary and Conclusions	125
5.1 Pre-Catalyst and Post-Catalyst EGR	125
5.2 Knock Modeling and Prediction	126
5.3 Recommendations for Future Work	128
Acronyms	135

List of Figures

1-1 A substantial portion of the work extracted from the combustion of fuel is used to draw air through the throttle restriction, significantly reducing efficiency at low loads.	22
1-2 The maximum torque output of a naturally aspirated engine is illustrated by the curve (a). If the displacement is reduced the shape of the maximum output curve (b) is scaled to smaller values. The addition of a turbocharger increases the maximum output from (b) to (c), which is similar to (a).	23
1-3 The ignition delays predicted by Eq. 1.8 and Eq. 1.6 differ in their sensitivity to temperature with Eq. 1.8 exhibiting considerably stronger temperature dependence.	27
1-4 The percentage difference between ignition delays predicted by Eq. 1.8 and Eq. 1.6 is shown. As indicated the range within which these expressions agree to $\pm 10\%$ is limited to a very narrow temperature band. The region of the pressure and temperature map studied by He et. al. provides some potential insight into the reason for the observed differences. The best fit form of the ignition delay function depends strongly on the region of the p - T map over which the fit is computed. The fit used by Douaud and Eyzat relied heavily on testing in CFR research engines which cause the end gas to reach higher pressures prior to autoignition.	27
1-5 An uncooled high-pressure EGR loop (a), and a cooled low-pressure EGR loop (b) are shown on a schematic diagram of a turbocharger spark ignition engine.	28
1-6 The spatial and temporal evolution of exothermic centers (ETCs) is shown in this image produced by Maly which shows the extent of burned regions during the autoignition event. ETCs such as B develop into deflagrations, this is the dominant mode by which the end gas is consumed. Alternatively the center which is marked A proceeds into a developing detonation. The combined effect of the rapid combustion of the end gas forces the main flame produced by the spark plug backward. Reproduced with permission from The Combustion Institute ^[45]	30

2-1	Positions of sensors in the intake air path. Only sensors connected to the data acquisition system are shown. The factory installed sensors connected to the engine control module (ECM) and used for engine control exist alongside these data acquisition sensors.	35
2-2	Diagram of the direct injection system on the LNF. Under some light-load conditions the side-mounted injector spray interacts with the piston bowl. During most high-load operation this interaction does not occur as the fuel is injected while the piston is lower in the stroke. Image © General Motors.	36
2-3	Diagram of fuel system. Fuel leaving either of the two tanks proceeds through a low pressure pump, secondary fuel filter and pressure regulator before reaching the fuel source selection valve. Fuel from the selected tank flows into a fuel delivery selection valve which directs the fuel to either a purge outlet or the engine. Fuel flowing to the engine enters a small damping tank before proceeding through the high pressure fuel pump. The high pressure fuel is then delivered to the direct injectors.	36
2-4	The cylinder pressure transducer is located within the cylinder head between the intake and exhaust valves. The transducer is approximately 20 mm from the cylinder wall.	37
2-5	Positions and types of sensors in the exhaust and EGR system. The dotted line between the point just downstream of the catalyst and the EGR cooler represents an alternative configuration of the EGR loop that draws exhaust gasses from downstream of the catalyst.	38
2-6	Gaseous fuels were added to a point in the intake path between the air heater and throttle plate. Fuel gasses were delivered through a flow proportioning valve and flame arrestor.	39
2-7	Diagram of the cooling system used with the LNF engine. Coolant is supplied from a tank and a portion of the flow through the engine is directed through the EGR cooler. The coolant temperature is reduced using a heat exchanger fed with municipal water or increased using an electric heater.	42
3-1	The mole fractions of carbon dioxide, water vapor, oxygen, carbon monoxide and hydrogen as a function of air-fuel equivalence ratio.	50
3-2	A spark sweep performed with the EGR system installed in the pre-catalyst location results in a higher net indicated fuel conversion efficiency than when the EGR system is installed in the post-catalyst configuration or removed entirely. This installation effect occurs in the absence of recirculation flow (with the EGR valve fully closed).	52
3-3	The majority of the efficiency improvement realized by installing the EGR system in the pre-catalyst location is attributable to an overall increase in pressures in the pre-catalyst configuration. This potentially indicates a change in charge composition.	53

3-11 The burn duration at fixed CA50 of 14° aTDC increases uniformly for EGR rates higher than 1.25%. The magnitude of the observed changes in burn duration is on the order of 2° for a change in EGR rate of 8.75%.	60
3-12 The relationship between spark timing and CA50 appears to be uniform over the range of EGR rates and combustion phasing values studied. The spark timing must be advanced just over 2° to maintain constant CA50 when the EGR rate is increased from 0% to 10%. The range of variation in CA50 that is observed at constant spark timing is considerable which complicates the interpretation of data that is presented with spark timing as the abscissa.	61
3-13 The gross indicated mean effective pressure (GIMEP) plotted as a function of CA50 shows only a slight dependence on EGR rate. The reduction in peak GIMEP from the 0% EGR case is accounted for by a reduction in the combustion efficiency.	61
3-14 The efficiency improvements that are offered by EGR take the form of improvements that alter the thermodynamic characteristics of the charge and improvements that alter the autoignition behavior, which allow more favorable combustion phasing.	64
3-15 The knock limited CA50 is indicated on a normalized plot of GIMEP. Increasing the EGR rate from 0% to 6.25% decreases the knock limited CA50 by just over 3°. If a conservative strategy is adopted as would be required in a production engine due to cycle-to-cycle variation in CA50 the improvement in GIMEP is approximately 1.4%. The <i>aggressive</i> CA50 limit indicates the CA50 at which the engine could operate with only 10% knocking cycles if there was no cycle-to-cycle variation in CA50.	65
3-16 As EGR is first introduced the initial effect is to slow the early phases of flame development without changing the knock limited CA50. However, beyond EGR rates of 2.5% the majority of the spark advance is used to advance the CA50 to take advantage of the improved knock tolerance of the charge.	66
3-17 During rich operation ($\lambda = 0.95$) the response of GIMEP to increasing EGR rates is similar to the stoichiometric case. Maximum brake torque (MBT) output appears to decrease with increasing EGR rate.	66
3-18 Burn duration are very similar between rich and stoichiometric operation (cf. Figure 3-10), although a larger range of EGR rates was possible.	67
3-19 The burn duration at a fixed combustion phasing of 14° aTDC increases along similar lines as the stoichiometric case, however beyond 7.5% EGR the burn duration appears to stabilize. Because such EGR rates could not be obtained at this combustion phasing it is not known whether this is a feature unique to rich EGR.	67

3-20 The change in knock limited spark advance up to 6.25% EGR is very close to the change observed under stoichiometric conditions, however the change in the knock limited CA50 is reduced from 3° in the stoichiometric case to 2°. This may indicate that at the same dilution rate rich EGR provides less knock abatement however the fact that the knock limited CA50 has already been advanced 1.6° due to the change in air-fuel ratio may contribute to this difference in behavior.	68
3-21 The smaller change in knock limited CA50 and more optimal initial combustion phasing under rich operation mean that improvements in GIMEP are smaller than the stoichiometric case.	68
3-22 The MBT CA50 and overall characteristics of the GIMEP profiles are unchanged from the conditions observed with pre-catalyst EGR.	69
3-23 Burn durations and their dependence on EGR rate is also very similar to the pre-catalyst EGR conditions, however the data indicates that spark to 10% burn durations are reduced by 3° across all conditions.	70
3-24 The relationship between spark timing and CA50 demonstrates the change that has occurred in the early stages of flame development when the EGR system was changed. The post-catalyst configuration results in shorter flame development periods. This is believed to be caused by an increase in scavenging during valve overlap which tends to enrich the charge.	70
3-25 Changes in the knock limited spark advance and knock limited CA50 are similar to those observed with pre-catalyst EGR at a slightly higher external EGR rate. This may be due to displacement of residual gasses in the pre-catalyst configuration that does not occur using the post-catalyst installation.	71
3-26 The knock limited CA50 with no EGR is close to MBT timing, thus improvements in efficiency due to improvements in autoignition tolerance result in a considerably lower efficiency gain.	71
3-27 The replacement of gasoline with hydrogen fuel in the percentages indicated above each point indicate that the initial effect of hydrogen addition is to decrease the spark to 50% burn duration without substantial changes in the knock limited CA50. Beyond 3% hydrogen by energy the additional hydrogen reduces changes in the unburned gas temperature resulting in improved knock resistance and earlier knock limited CA50 values.	72

3-28 The addition of CO initially results in shortened spark to 50% burn durations and a modest improvement in the knock limited combustion phasing (1°). Beyond 4.5% of the fuel energy no additional improvement in the knock limit is realized however the burn durations continue to be reduced. It is unlikely that CO in the fractions present in EGR is capable of altering the gross combustion characteristics.	73
3-29 Nitric oxide appears to degrade the knock resistance of the air-fuel mixture despite relatively minute concentrations. This effect, although possible, is not likely to occur in practice because the formation rate of NO in engines operating with EGR is low.	74
4-1 Schematic diagram of a combustion bomb (adapted from Keck ^[31]) and a rapid compression machine showing their construction and key parts. The combustion bomb is filled with an air-fuel mixture which is ignited by the extended spark plug electrodes. The spherical flame that develops compresses the end gas near the chamber walls which may cause it to autoignite. The rapid compression machine (RCM) is filled with an air-fuel mixture and the hydraulic section is pressurized to hold the piston at the bottom of its stroke. A pneumatic pressure is then applied to a driving piston pre-loading the piston shaft. Once the hydraulic pressure is removed the piston is driven forward at high speed, compressing the air fuel mixture.	76
4-2 Schematic representation of two-stage ignition in a rapid compression machine. The temperature of the mixture may rise by 75 K during the cool flame stage which represents the release of well under 5 % of the total fuel energy.	76
4-3 The ignition delay isobars that are described by Eq. 4.4 are shifted upward by increasing a , downward by increasing b and increasing c increases the slope of the line while maintaining the same y-intercept.	79
4-4 Ignition delay data from Fieweger ^[22] for primary reference fuel (PRF) 90. The exponential temperature dependence in τ can only accurately model a portion of the ignition delay characteristics of a real fuel.	79
4-5 The reciprocal of the ignition delay is accumulated until the area under the curve equals unity. Errors accumulated up to t_c must be balanced by an additional area between t_c and $t_c + \Delta t_c$	81
4-6 Contour plot of $(\Delta\tau/\tau)(1/(\tau + \Delta\tau))$ which is the controllable factor that influences uncertainty in ignition delay prediction (Δt_c). The upper left portion of the map represents the most damaging situation per unit integration time and the lower right is the least damaging. Contours are spaced logarithmically with units of ms^{-1}	82

4-7 Three functional relationships between τ and $\Delta\tau$ are explored that result in identical values of U from Eq. 4.18 and therefore are expected to result in similar errors in autoignition prediction. A slight improvement in accuracy near the autoignition conditions allows considerably more latitude for errors at higher ignition delays. A comparison of these functions with contours over which the integrand of U is constant indicate that when $\Delta\tau \propto \tau^2$ the integrand of U is nearly independent of τ and thus errors are accumulated uniformly over time.	84
4-8 A fit to ignition delay data observed in shock tubes experimentally by Fieweger ^[22] was computed by weighting the data according to $(\tau - 2.5 \text{ ms})^{-2}$. The center of the weighting function is dictated by the operating characteristics of a particular apparatus, with ignition delays of 2 ms to 3 ms being common near the time of autoignition in CFR engines ^[17] . For an engine that operates at higher temperatures and pressures the weighting target would be shifted to the left resulting in a higher slope.	85
4-9 The cylinder pressure transducer is located in the cylinder head between the intake and exhaust valves.	89
4-10 The high-pass filtered cylinder pressure (\hat{p}) oscillates during an autoignition event. The first 1 bar threshold crossing, indicated by the square, occurs roughly 50 μs after anomalous pressure fluctuations are first observed.	93
4-11 Comparing the measured cylinder pressure (p) to the low-pass filtered cylinder pressure aids in the manual identification of knock onset time, indicated by the circle, which is placed at the first sign of pressure rise beyond the smoothed curve that is followed by oscillatory ringing.	93
4-12 The three stages of autoignition are distinguishable on an i_o contour. During normal combustion i_o has a low, consistent slope which increases rapidly to a maximum value during the active autoignition stage. Following the active stage of autoignition the pressure oscillations are damped out, causing the slope to decay towards the value present during normal combustion.	95
4-13 Two intersecting lines are fit to the i_{po} contour for a cycle in the region surrounding the maximum filtered pressure. The intersection of the two fit lines is identified as the time of knock onset as indicated by a circle. Note that adjustment of the fit window to incorporate only normal combustion and active autoignition does not materially affect the identified knock onset time.	96
4-14 The difference between manually and automatically identified knock onset time for the proposed algorithm ($\mu = 20 \mu\text{s}$, $\sigma = 37 \mu\text{s}$) and the thresholding approach ($\mu = -72 \mu\text{s}$, $\sigma = 300 \mu\text{s}$).	96

4-15 Correlation between the experimentally observed knock time (t_{ke}) correlates well with the knock time predicted by the autoignition model (t_{km}). Each cluster of points represents a different engine speed. Total of 4219 knocking cycles ($\max \hat{p} \geq 1$) under 336 steady state operating conditions.	99
4-16 The data presented on a time basis (cf. Figure 4-15) may be plotted in terms of crank angles to collapse differences in timescale due to engine speed variation.	99
4-17 Histogram of error between modeled and experimental knock time. The distribution has a mean of 26 μs and a standard deviation of 53 μs . The positive mean value indicates that the model consistently predicts autoignition slightly before it is observed.	100
4-18 Iso-delay contours are plotted for 0.5 ms to 250 ms on the p - T plane with $w_d = 0$. The pressures and temperatures observed at autoignition are indicated as points and a representative p - T trajectory for an adiabatic and isentropic compression is shown. Ignition delays ranging from 0.5 ms to 1 ms are most common at the autoignition conditions. Alternative iso-delay contours for non-zero dilution rates may be constructed by multiplying the contour levels by $(1 - w_d)^{-0.618}$	101
4-19 Error in the knock integral correlation is initially uncorrelated with CA50 for early combustion phasing, however near MBT combustion phasing the errors begin to deviate from the mean value. This can be traced back to the longer induction times when the engine is operated with late combustion phasing.	102
4-20 The best correlation is found between the ignition delay at knock and the error. Such a correlation most likely arises due to oversimplification of the mathematical form of the ignition delay. Recalling the typical shapes of ignition delay measurements (cf. Figure 4-4) the direction of the observed errors is consistent with the expected overestimation of smaller ignition delays and underestimation of larger delays.	102
4-21 The iso-delay contours on the p - T map are very similar for Eq. 4.48 (black) and for Eq. 4.50 (red, dashed). They are particularly similar near the conditions at autoignition which are shown as points.	103
4-22 Correlation between the experimentally observed knock crank angle (θ_{ke}) and the crank angle of knock predicted by the autoignition model (θ_{km}). This correlation is not as strong as the stoichiometric correlation indicating that there is some work still to do in the identification of appropriate correlating parameters.	110
4-23 Histogram of error between modeled and experimental knock time. The distribution has a mean of 32 μs and a standard deviation of 59 μs . The positive mean value indicates that the model consistently predicts autoignition slightly before it is observed.	110

4-24 The error in autoignition prediction is correlated with the ignition delay at knock. This correlation is consistent with a mathematical ignition delay model that overestimates the ignition delay when it is lower than typical values at autoignition and overestimates ignition delay values that are larger.	110
4-25 Variation in CA50 alone is insufficient to describe the presence of both knocking and non-knocking cycles at a steady state operating point.	111
4-26 Variation of knock intensity from one cycle to the next.	113
4-27 Some of the variation in knock intensity may be attributed to variation in CA50. However, as evidenced by the vertical spread, combustion phasing alone does not account for all of the CA50 variation.	114
4-28 The probability density histogram of experimental data agrees well with a lognormal fit.	114
4-29 If the values of the autoignition integral for macro-scale end gas parcels are normally distributed a portion of the end gas will cross the autoignition limit in time Δt . The factors that govern the rate at which the available fuel crosses the autoignition limit are primarily the rate of change of I_μ and the distribution width I_σ	117
4-30 The intensity of knock does not appear to be correlated with the available mass of fuel at the inception of autoignition.	118
4-31 The mean knock intensity scales with the ignition integral slope ($1/\tau_k$), the mean knock intensity appears to increase exponentially.	119
4-32 Frequency distributions for ranges of $1/\tau_k$. As $1/\tau_k$ increases the center of the distribution moves towards higher knock intensities and the length of the distribution tail to the right is increased. This behavior mirrors the behavior of a lognormal distribution with increasing scale parameter (μ).	119
4-33 Correlation between the ignition integral slope and location parameter is nearly linear for knocking cycles.	121
4-34 Cycles below with an ignition integral slope of below 800 s^{-1} are very unlikely to knock, thus the data in this range is of limited use.	121
4-35 The scale parameter is approximately constant for values of the ignition integral slope greater than 800 s^{-1}	122
4-36 The probability that a cycle will exceed 1 bar in knock intensity grows according to the cumulative density function $p_k = 1 - F(1, 1/\tau_{k,m})$	123
4-37 Similarly the probability that a cycle will exceed 5 bar in knock intensity is modeled by $p_k = 1 - F(5, 1/\tau_{k,m})$	123

List of Tables

2.1	The geometry and characteristics of the General Motors LNF engine are typical of many turbo-downsized four cylinder engines produced between 2007 and 2015.	34
2.2	The cam phasers can adjust the intake and exhaust cam phasing by 50°. The default or parked position of the intake and exhaust cams are given as well as the fully phased position. The intake cam timing is advanced and the exhaust cam timing is delayed with increased phaser activity.	40
2.3	Fixed valve timing values used to collect the experimental data presented in this document except where alternative valve timing is specifically stated. This cam phasing has moderate overlap at 52° using the 0.25 mm lift definition of opening and closing.	40
4.1	Uncertainty types as functions of τ	83
4.2	Experimental conditions for τ determination consist of 4219 individual knocking cycles from 336 unique steady state operating points.	98
4.3	Composition of the exhaust and charge for lean, stoichiometric and rich operation with EGR. Note that δ is negative for the fuel rich case.	108
4.4	Table of operating points for optimization of k_r and k_l , this data set consists of 4537 non-stoichiometric knocking cycles.	109

Chapter 1

Introduction

The design and operation of internal combustion engines has been an area of intense academic and practical research for well over a century. With a history of such length and a device of such ubiquity there is often a temptation to believe that there is little left to do and few improvements to make. However, this is most certainly not the case. The degree to which internal combustion engines have become a part of lives throughout the world has fostered cultural connections to the services that engines provide. This connection between people and engines has driven their development to adapt to the constantly shifting social, political and environmental concerns of world societies. These shifting societal ideals ensure that new technologies, methods and theories are always in demand. Of special interest now, at the beginning of the 21st century, are the carbon dioxide and other gaseous emissions of internal combustion engines. The link between carbon dioxide emissions and changes to the climate of Earth have driven many countries to institute minimum fuel mileage standards throughout the transportation sector, prompting vehicle manufacturers to search for and implement strategies that improve the efficiency with which chemical fuel energy is used to move vehicles about. The research effort detailed in this document seeks to develop a detailed quantitative understanding of the autoignition of air-fuel mixtures – a key factor that limits the efficiencies possible using spark-ignited engines – and a promising method of autoignition abatement that relies on dilution of a combustible mixture with inert chemical species.

1.1 Motivation

The principal motivation for current research on autoignition is the demand for high efficiency, low emission vehicles. Beginning in the mid 1970s concerns regarding vehicle emissions and efficiency began to take legislative hold in the United States. Initially, high levels of harmful gaseous emissions and gross overuse of fuel were the primary concerns, however with the widespread introduction of the three way catalyst and electronic fuel injection systems levels of avoidable emissions have decreased

substantially. The corporate average fuel economy (CAFE) standards, which were imposed in the wake of the 1973 oil crisis to improve the fuel economy of vehicles sold in the United States, require that vehicles offered for sale meet or exceed a fleet averaged fuel efficiency, which is often stated as a number of miles per gallon of fuel consumed. CAFE standards initially rose the minimum fleet averaged fuel economy from 18 mpg in 1978 to 26 mpg by 1983, however over the subsequent 27 years CAFE standards were stagnant, increasing to only 27.5 mpg by 2010. Beginning in 2011 concerns regarding carbon dioxide emissions and fossil fuel consumption in the United States led to the adoption of updated CAFE standards that plan to reach a fleet averaged minimum fuel economy of 54.5 mpg by 2025 for cars and light duty trucks. The task of reducing fuel consumption by nearly half in under 15 years presents many technical and economic challenges.

An approach that has seen widespread adoption over the past five years is the simultaneous reduction of displacement volume and increase in maximum output per unit of displaced volume – which is usually accomplished using a turbocharger. This strategy, which is often called turbo downsizing^[41], replaces a large naturally aspirated engine with a smaller turbocharged engine, and is an effective method of increasing the average engine efficiency achieved during use without compromising maximum torque output. Turbo downsizing accomplishes this by recognizing that automotive engines are frequently operated well below their maximum output. A naturally aspirated engine operating under these conditions restricts the flow of air into the intake manifold, which reduces the intake manifold pressure to a level well below atmospheric pressure. The pumping work associated with maintaining this pressure differential consumes a considerable fraction of the work extracted from combustion at low loads, greatly reducing the net efficiency (cf. Figure 1-1). Alternatively, if the displacement of the engine is reduced, the engine is less throttled for the same torque output; therefore the pumping work is reduced and the efficiency is improved^[50]. A turbocharger is then added to the downsized engine to allow the intake manifold pressure to exceed atmospheric pressure. This allows the turbo downsized engine to burn fuel and air at roughly the same rate as a larger engine, thereby achieving a similar maximum torque output (cf. Figure 1-2).

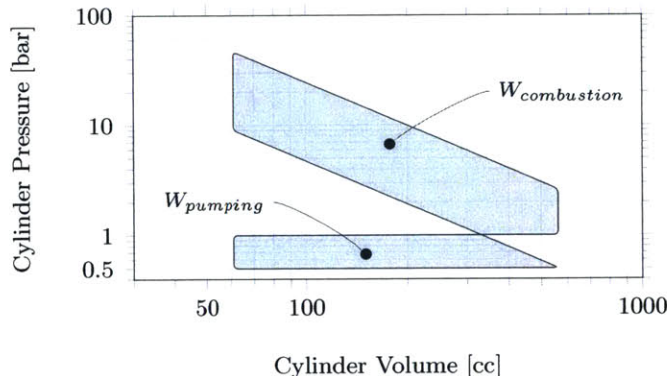


Figure 1-1: A substantial portion of the work extracted from the combustion of fuel is used to draw air through the throttle restriction, significantly reducing efficiency at low loads.

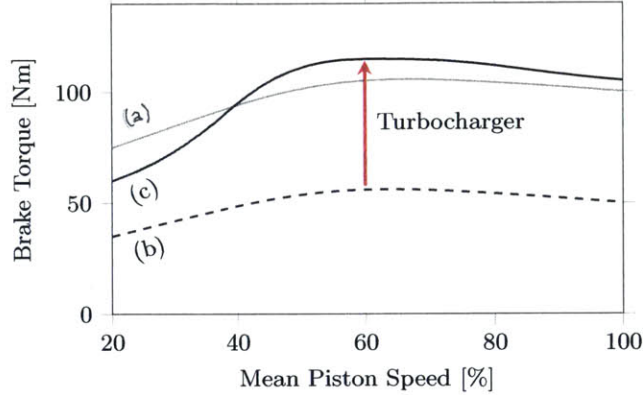


Figure 1-2: The maximum torque output of a naturally aspirated engine is illustrated by the curve (a). If the displacement is reduced the shape of the maximum output curve (b) is scaled to smaller values. The addition of a turbocharger increases the maximum output from (b) to (c), which is similar to (a).

Although the part-load efficiency of a turbo-downsized engine is higher than its naturally aspirated counterpart, several factors limit the efficiency of these engines at medium to high loads^[60]. A challenge of particular importance is the occurrence of autoignition, also known as knock, and the measures required to avoid it. Knock occurs when an unburned mixture of air and fuel (end gas) is compressed, heated and given sufficient time to autoignite independently of the flame initiated by the spark plug. The rapid heat release that occurs during autoignition results in potentially damaging cylinder pressure oscillations and rapidly increases the temperature of critical engine components. This makes the avoidance of severe knock essential to engine durability. As engine displacement is reduced the maximum torque required, which is largely a function of vehicle weight, remains virtually unchanged. This requires that downsized engines operate at a higher output per unit displacement, a requirement which tends to promote autoignition. Thus as turbo downsizing is pursued, autoignition begins to play an increasingly critical role in the design and operation of spark-ignited automotive engines.

1.2 Background and Literature Review

Much research has been performed on the autoignition of air-fuel mixtures with the earliest efforts dating back well over one hundred years. In the early part of the 20th century the majority of research effort was dedicated to the identification of suitable fuel additives that have the ability to delay the occurrence of autoignition. This research effort lead to the identification of tetraethyl lead (TEL) as an anti-knock additive and a great deal of additional effort was expended to understand the source of its anti-knock properties. Although the effectiveness of TEL as an anti-knock additive is beyond question the neurotoxicity of lead presents health risks that are beyond the tolerance of modern society. Beginning in the mid-1970s TEL was phased out of most fuels in the United States although it still remains in limited use for piston-powered aircraft engines. Unfortunately, many of

the additives that have the capability to prevent autoignition also present toxicity risks to humans, and thus the research focus has shifted towards making the best possible use of available fuels.

Mathematical Autoignition Models

Beginning in the 1950s several methods of developing a mathematical model of autoignition were explored. Semenov proposed a series of chemical reactions for a simplified two component fuel known as primary reference fuel (PRF) that when combined result in reproducing the variations in induction time observed during experimental autoignition testing^[21]. The simplified chemical model consists of five or more coupled differential equations along with temperature dependent rate constants to describe each reaction mechanism. This model was refined and further developed by researchers at Hartwell Research Laboratory^[15] and Shell^[26, 53] and shown to agree reasonably well with experimental autoignition data. The primary difficulty encountered in applying autoignition models of this type has been the chemical complexity of realistic fuels. Gasoline, which generally contains hundreds of chemical compounds, behaves somewhat differently than PRF blends and it has been observed that if models based on a representative set of reaction equations are to be used in engines it is often necessary to modify rate and temperature constants to obtain agreement between the model and experimental testing. This presents some difficulty due to the number of rate and temperature constants involved. For this reason much of the autoignition modeling performed on engines uses simpler empirical models.

Experimental evidence has shown that many of the features of autoignition can be modeled using the Livengood-Wu autoignition integral^[44]. This empirical approach suggests that autoignition is a cumulative chemical process that depends on the temperature and pressure history of the unburned gases and the properties of the air-fuel mixture. When an air-fuel mixture is compressed rapidly and held at high pressure and temperature the time between compression and autoignition is often called the *ignition delay*. If the compression process and experimental apparatus are well controlled the temperature and pressure during the ignition delay – which is sometimes called the induction period – are nearly constant. Therefore if t_0 is defined as the end of compression and t_c is defined as the time of autoignition the ignition delay (τ) is given by

$$\tau(\bar{p}, \bar{T}) = t_c - t_0, \quad (1.1)$$

where \bar{p} and \bar{T} are the constant post compression pressure and temperature of the end gas respectively. Livengood and Wu observe that if such testing is performed over a wide range of \bar{p} and \bar{T} values the ignition delay function for a specific air-fuel mixture may be approximated by an expression with the form

$$\tau(p, T) = ap^{-b}e^{c/T}, \quad (1.2)$$

where a , b and c are air-fuel mixture dependent constants. In a real firing engine, unlike the specially designed machines for measuring the ignition delay, the pressure and temperature of the end gas changes smoothly as a function of time. To apply ignition delay measurements to real engines Livengood and Wu suggest that autoignition will occur when the concentration of a hypothetical knock precursor $[x]$ reaches a critical level $[x]_c$. If the reaction that produces the knock precursor is independent of the precursor concentration the relative concentration at time t is given by

$$\frac{[x]}{[x]_c} = \int_{t_0}^t \frac{1}{\tau(p, T)} dt, \quad (1.3)$$

where τ is the empirically determined ignition delay function. If the critical concentration is constant across various operating conditions then autoignition will occur at time t_c where

$$1 = \int_{t_0}^{t_c} \frac{1}{\tau(p, T)} dt. \quad (1.4)$$

If Eq. 1.4 is used in a firing engine t_0 is selected as any time at which the ignition delay is very large, generally a time around intake valve closing (IVC) is used. Alternatively if the conditions of the empirical ignition delay testing are used in which $p(t) = \bar{p}$ and $T(t) = \bar{T}$ the measured induction duration $t_c - t_0$ is recovered.

The empirical method developed by Livengood and Wu has been widely used since its introduction and many researchers have contributed to the development of ignition delay functions for use with different fuels and mixtures. Some of the best known work in this area was done by Douaud and Eyzat of the Institut Français du Pétrole (IFP)^[17, 25]. In their work, which was based on both testing in CFR research engines and real vehicles, they identified an ignition delay expression that works for several blends of PRF

$$\tau_{DE}(p, T) = 0.01869 \left(\frac{ON}{100} \right)^{3.4017} p^{-1.7} e^{\frac{3800}{T}} \quad [\text{s}], \quad (1.5)$$

where ON is a volume fraction of isoctane blended with n-heptane between 80% and 100%, p is a pressure in kgf cm^{-2} and T is a temperature in K. Douaud and Eyzat also observed that the sensitivity – that is the research octane number (RON) minus the motor octane number (MON) – of a fuel appears to affect the numerator of the exponential term which governs the temperature dependence of the ignition delay. The units of the Douaud-Eyzat correlation may be converted to the more frequently used pressure units of bar which yields

$$\tau_{DE}(p, T) = 0.01932 \left(\frac{ON}{100} \right)^{3.4017} p^{-1.7} e^{\frac{3800}{T}} \quad [\text{s}]. \quad (1.6)$$

Recent experimental work has focused on identifying ignition delay functions based on testing in

either a rapid compression machine (RCM), combustion bomb or shock tube^[22, 39, 31, 57, 12]. Several ignition delay expressions have been proposed that include air-fuel ratio effects for simple fuels such as isoctane which has been reported to collapse well over a limited range of pressures and temperatures using the expression^[28]

$$\tau_{IO}(p, T) = 1.3 \times 10^{-4} p^{-1.05} \phi^{-0.77} x_{o_2}^{-1.41} e^{\frac{33700}{RT}} \quad [\text{ms}], \quad (1.7)$$

where p is the pressure in atm, T is the temperature in K, ϕ is the fuel-air equivalence ratio, x_{o_2} is molar percentage of oxygen and $R = 1.987 \text{ cal mol}^{-1} \text{ K}^{-1}$ is the gas constant. Converting the pressure units to bar, assuming stoichiometric operation with no excess oxygen and substituting the value of the gas constant provides the simplified equation

$$\tau_{IO}(p, T) = 1.79 \times 10^{-9} p^{-1.05} e^{\frac{16960}{T}} \quad [\text{s}], \quad (1.8)$$

which has a temperature sensitivity more than four times higher than the Douaud-Eyzat correlation for isoctane ($ON = 100$). Comparing these two ignition delay correlations over the pressure and temperature map reveals the extent to which temperature dominates the predicted ignition delay of Eq. 1.8 in comparison to Eq. 1.6 (cf. Figure 1-3). One of the key difficulties of implementing these or any other ignition delay approximation in an engine originates from the large range of pressures and temperatures experienced by the end gas in the time leading up to autoignition. If a set of representative pressures and temperatures traversed prior to autoignition are indicated on the p - T diagram they will fall very close to a straight line representing the adiabatic and isentropic compression of the end gas. An examination of the percentage difference between the predicted ignition delays of Eq. 1.8 and Eq. 1.6 indicates that these expressions only agree to within $\pm 50\%$ of the ignition delay value over a relatively narrow range of temperatures, a characteristic that suggests that the application of one of these expressions to engines may provide inaccurate prediction results due to the wide range of temperatures traversed (cf. Figure 1-4). Although neither expression can claim to model the ignition delays well over the entirety of the p - T map it is clear that the demands of autoignition prediction in engines present critical choices about the scope over which experimental data is collected and the manner in which this data is fit to a simplified mathematical form.

Autoignition Mitigation Strategies

The most common method of avoiding autoignition during the operation of an engine is to retard (delay) the spark timing, this shifts combustion to a later point in the engine cycle, reducing the peak cylinder pressure, which decreases the amount of adiabatic compression experienced by the end gas, thereby reducing the maximum end gas temperatures. Altering the spark timing in this way

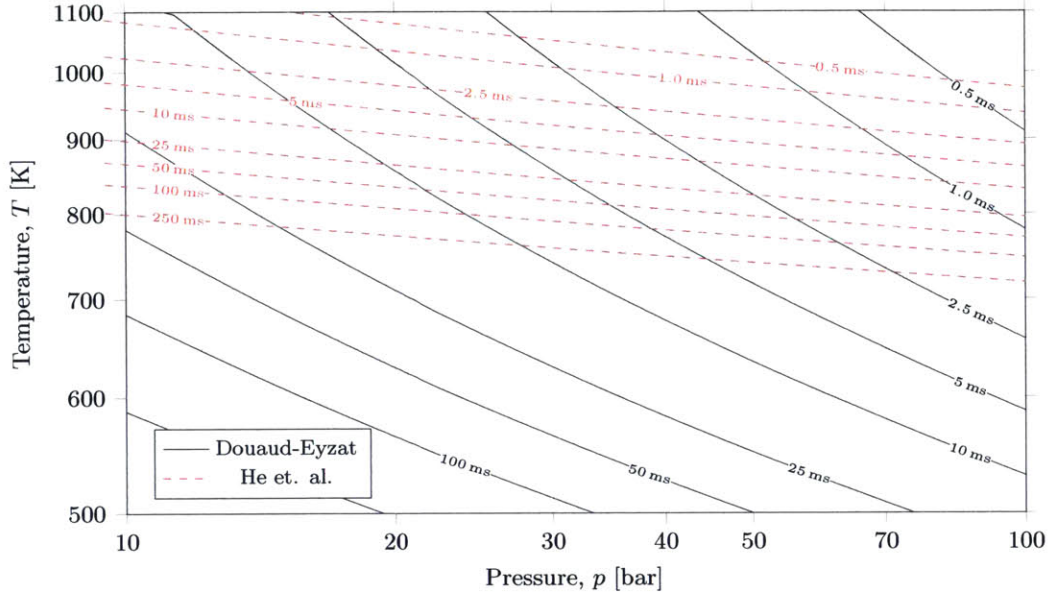


Figure 1-3: The ignition delays predicted by Eq. 1.8 and Eq. 1.6 differ in their sensitivity to temperature with Eq. 1.8 exhibiting considerably stronger temperature dependence.

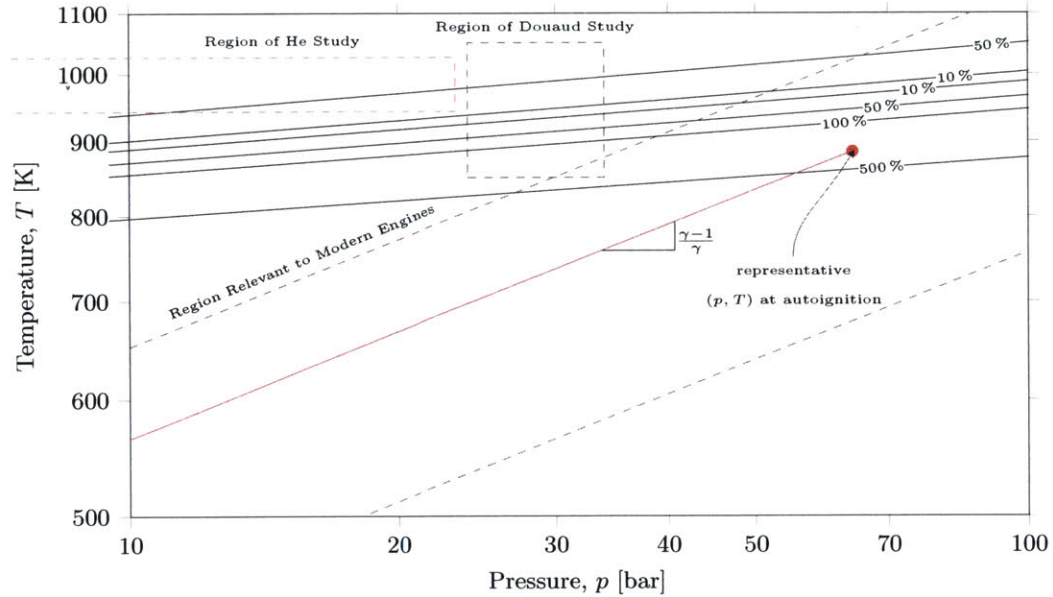


Figure 1-4: The percentage difference between ignition delays predicted by Eq. 1.8 and Eq. 1.6 is shown. As indicated the range within which these expressions agree to $\pm 10\%$ is limited to a very narrow temperature band. The region of the pressure and temperature map studied by He et. al. provides some potential insight into the reason for the observed differences. The best fit form of the ignition delay function depends strongly on the region of the p - T map over which the fit is computed. The fit used by Douaud and Eyzat relied heavily on testing in CFR research engines which cause the end gas to reach higher pressures prior to autoignition.

is an effective method of avoiding knock because it simultaneously reduces the end gas pressures and temperatures which, according to the knock integral and ignition delay models, are the driving factors behind the autoignition process. However, retarding the spark timing is detrimental to engine efficiency because the phasing of combustion is shifted to a less favorable geometric configuration of

the piston-crank mechanism, reducing the ability of the engine to extract work. As a result of less efficient work extraction, retarding the spark timing increases the exhaust gas temperature, which may reach levels that are potentially damaging to downstream components such as the turbine and catalyst. Under some conditions modern engines inject excess fuel to aid in the cooling and protection of these critical components at the expense of fuel efficiency.

A method of avoiding autoignition that has shown experimental promise is the use of exhaust gas recirculation (EGR)^[23, 2, 3, 4, 32, 1]. In an EGR system a portion of the combustion products are extracted from the exhaust and mixed with fresh air, this mixture is then admitted to the cylinder where fuel is added and subsequently burned. The exhaust gases do not participate chemically in combustion, however they alter the specific heat ratio (γ) and the thermal mass of the charge. The increase in charge mass and γ result in an in higher pre-combustion pressures and lower peak end gas temperatures^[30], which tends to reduce the tendency of the end gases to autoignite. To enhance this effect the EGR flow is often cooled before it is mixed with fresh air, this configuration is known as cooled EGR. EGR systems are further classified by their source and sink locations. In a low-pressure EGR system exhaust is extracted from a location downstream of the turbine and admitted upstream of the compressor, alternatively high-pressure EGR may be extracted upstream of the turbine and admitted downstream of the compressor (cf. Figure 1-5). A final type of EGR that has seen considerable use in recent engine designs is internal EGR, in this approach combustion products from the current cycle are retained within the cylinder for inclusion in the next cycle. Of these configurations cooled low-pressure EGR is preferred for knock abatement because internal EGR cannot be cooled and at lower engine speeds (where knock is most prevalent) there is insufficient pressure differential to drive high-pressure EGR flow^[52].

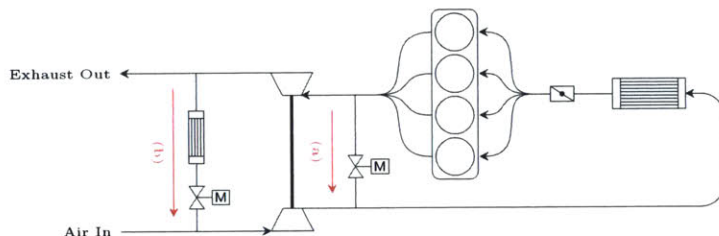


Figure 1-5: An uncooled high-pressure EGR loop (a), and a cooled low-pressure EGR loop (b) are shown on a schematic diagram of a turbocharger spark ignition engine.

The change in the pressures and temperatures of the end gas is not the entire story with regard to the effects of EGR on autoignition. It has been observed that the addition of various species including carbon monoxide, hydrogen, water vapor and oxides of nitrogen affect the ignition delay of automotive fuels^[7, 34, 4]. And although other diluents such as carbon dioxide do not appear to chemically participate in autoignition reactions they do reduce the molar concentration of critical species such as oxygen, resulting in changes in autoignition behavior^[28]. Attempts have been made to quantify the effects of dilution and charge composition – see for example Eq. 1.7 – however the

success of these expressions in engines has been somewhat limited. A possible cause of the inaccuracy of these expressions when used in engines is the limited range of pressures and temperatures over which the ignition delay – along with its dependence on charge composition and dilution – has been explored. Part of the difficulty of expanding the pressure and temperature range of ignition delay testing are the demanding requirements on the experimental apparatus. Due to geometrical and physical limits the range of pressures and temperatures that any individual shock tube, RCM or combustion bomb can explore makes up only a fraction of the region relevant to autoignition prediction in engines.

Recent testing of cooled low-pressure EGR installations has generated several inconsistent conclusions with regard to the effectiveness of EGR as a knock abatement strategy^[52, 5, 4]. In particular some literature sources report that extracting exhaust gasses from upstream of the catalyst and introducing these gases into the cylinder results in a notable change in autoignition behavior in comparison to extracting exhaust gasses after catalysis. It has been argued that combustible species in the pre-catalyst exhaust may aid the early phases of flame development and reduce the burn duration, thereby reducing the time available for knock chemistry to occur^[52] or alter the chemistry of autoignition reactions. However, earlier research has shown that oxides of nitrogen (NO_x) which exist in pre-catalyst exhaust gas, degrade the knock resistance of the air-fuel mixture^[34]. At this stage the difference between pre-catalyst and post-catalyst sourced exhaust gases is not clear, nor is the cause of the inconsistent findings reported within the literature.

Phenomenological Autoignition Observations

Detailed optical studies of autoignition transients in firing engines date back to the early 1990s after new developments in digital imaging allowed video to be captured at rates in excess of 750,000 frames per second. These new high speed imaging tools were used to examine the development of autoignition using schlieren photography techniques which allow density gradients within the charge to be photographed. Maly of Daimler-Benz AG combined schlieren and laser induced fluorescence (LIF) techniques to photograph the spatial and temporal evolution of an end gas autoignition event (cf. Figure 1-6)^[45]. This observation illuminated the degree to which inhomogeneity of the end gas drives the formation of discrete autoignition regions which Maly refers to as exothermic centers (ETCs). The ETCs develop at different times, in various locations and tend to exhibit differences in development following initiation. Maly classifies the modes of autoignition as follows:

- Deflagration – An ETC that develops into a propagating flame similar to the turbulent flame produced by the spark plug. This type of event produces weak pressure oscillations and occurs when temperature gradients are steep.

- Thermal explosion – The formation of a larger ETC that results in moderate pressure oscillations. The ETC often transitions into a deflagration shortly after development. Pressure oscillations due to this type of autoignition are moderate and the temperature gradients that cause it are somewhat flatter than those that result in deflagration.
- Developing detonation – An ETC that results in the pressure driven autoignition of nearby regions. This type results in the highest pressure oscillation levels and may cause rapid damage to the engine.

Of these three types, thermal explosion, which creates considerable acoustic noise but does not cause serious engine damage appears to be the most common in automotive engines under light to moderate knock. It is worth noting that all three may occur simultaneously during a single cycle.

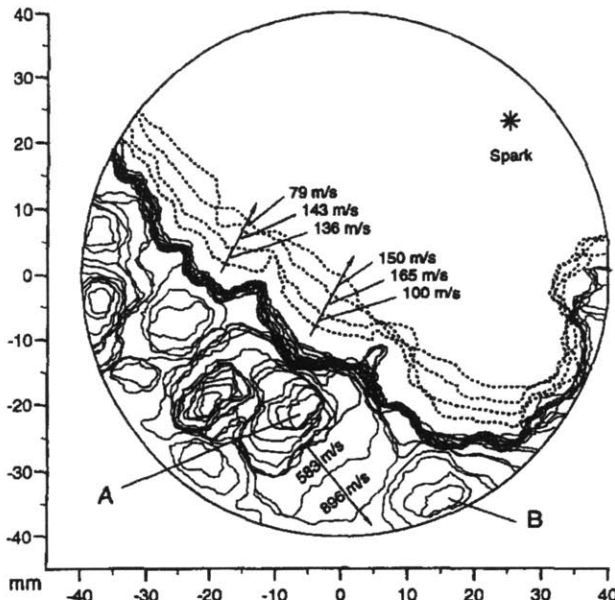


Figure 1-6: The spatial and temporal evolution of ETCs is shown in this image produced by Maly which shows the extent of burned regions during the autoignition event. ETCs such as B develop into deflagrations, this is the dominant mode by which the end gas is consumed. Alternatively the center which is marked A proceeds into a developing detonation. The combined effect of the rapid combustion of the end gas forces the main flame produced by the spark plug backward. Reproduced with permission from The Combustion Institute^[45]

The role of end gas inhomogeneity in the development of autoignition suggests that there is likely a sizeable stochastic component to the occurrence and severity of autoignition under a prevailing set of steady state conditions^[48]. This particular aspect of autoignition has largely eluded documentation within the literature, particularly in spark-ignited engines. Some authors have observed that during steady operation various autoignition intensity metrics indicate that only a fraction (generally less than 25%) of cycles exhibit the characteristic signs of autoignition^[43]. If the spark timing is advanced to promote the occurrence of autoignition cycles with severe knock, no sign of

knock and all possibilities in between are frequently observed. The potential for severe knock and the engine damage that may accompany it mean that the operational limits of the engine are based on the worst autoignition event likely to arise under a given set of conditions. For this reason the statistical factors that govern the occurrence and intensity of autoignition in engines are of particular interest. A reduction in the stochastic tendencies of autoignition can generally be transferred to an improvement in efficiency through more favorable combustion phasing or an increase in compression ratio.

1.3 Research Objectives

The goal of this research project is to deconstruct and quantify the physical and chemical effects of EGR on autoignition. The first task in this endeavor is to identify changes in engine behavior, such as burn duration, pumping work, emissions and stability, that are caused by altering the location of the EGR source from pre- to post-catalyst. This was approached by developing an EGR system that can be reconfigured to draw exhaust from either before or after the catalyst and testing this EGR system across a range of EGR flow rates and operating conditions. An analysis of the changes in engine behavior and autoignition characteristics was performed to develop a clear understanding of their origins. A key question that this research project seeks to answer is: do the chemical differences between pre-catalyst and post-catalyst sourced EGR result in significant changes in combustion or autoignition?

The second component of of this effort is the development of an extended knock integral correlation that incorporates changes in EGR rate and air-fuel ratio into a single expression, thereby allowing the onset of knock to be anticipated and its dependence on these controlled parameters to be assessed. In order to produce an accurate correlation with these three interrelated degrees of freedom a conventional approach to determining the ignition delay, which would require hundreds or thousands of time consuming experiments using a RCM or shock tube, was forgone and a method of determining the ignition delay using a real engine and a simplified engine model was developed. Following the identification of an empirical ignition delay model the physical and chemical factors that result in cycle-to-cycle variations in autoignition were examined and a model proposed that links engine operating conditions to the intensity of autoignition and the level of variation in intensity that can be expected.

In summary the research objectives consist of the following four items:

- Effects of EGR source
 - Identify and quantify the effects of the volatile components of recirculated exhaust gases extracted from a location upstream of the catalyst on autoignition and combustion

- Identify and quantify the physical effects of extracting exhaust gasses upstream or downstream of the catalyst on engine operation
- Knock onset and intensity correlation
 - Develop an ignition delay expression that includes EGR and air-fuel ratio and is suitable for use with engines: $\tau(p, T, \lambda, w_{egr})$
 - Develop a statistical model of knock intensity that relates operating conditions to cycle-to-cycle variation in knock intensity

Chapter 2

Experimental Apparatus and Procedures

In this chapter the configuration of the engine and experimental system will be outlined, with special care given to the description of the sensing hardware. First, the configuration of the subsystems that make up the engine will be detailed including the air flow path, fuel delivery system, exhaust, EGR system, valvetrain and turbocharger. Following this account the configuration of auxiliary systems such as the dynamometer, cooling system and data acquisition system will be explained. The procedures used during the collection of experimental data will also be described as knowledge of the structure of these procedures is essential to interpretation of the data that is generated by their use.

2.1 Engine

A General Motors Ecotec Generation II engine, identified by the designation LNF, was used to acquire the experimental data presented in this document. The four cylinder, turbocharged, direct injected engine was first sold in 2007 and has a displacement volume of just under 2 L. It develops a maximum output power of 190 kW (260 hp) at 5300 rpm and peak torque of 353 N m (260 lb ft) at 2000 rpm. The engine geometry and compression ratio (cf. Table 2.1) are representative of turbocharged and downsized engines and the engine control module (ECM) makes full use of the variable cam phasing and direct injection systems to maximize engine efficiency. In the years that have elapsed since the introduction of the LNF the compression ratio of new, Generation III, engines has risen slightly (the LTG has risen to 9.5) with relatively few changes to overall engine geometry or architecture. The changes have resulted in slightly higher maximum power and a modest improvement in fuel economy over the generation II design. Due to the architectural and geometric

similarities between the LNF and a number of competing engines the LNF is a test platform that is representative of an entire class of turbocharged, high output four cylinder engines.

Engine Specifications	
Configuration	straight-4
Displacement	1988 mL
Bore	86 mm
Stroke	86 mm
Connecting Rod	145.5 mm
Wrist Pin Offset	0.8 mm
Compression Ratio	9.2
Maximum Power	190 kW @ 5300 rpm
Maximum Torque	353 N m @ 2000 rpm
Fuel Delivery	direct injection
Turbocharger Type	twin-scroll
Valve Timing	dual cam phasers

Table 2.1: The geometry and characteristics of the General Motors LNF engine are typical of many turbo-downsized four cylinder engines produced between 2007 and 2015.

Intake Airflow

Fresh air enters the engine through a conical air filter, passes through a turbine air flow meter (IMAC Systems Quantometer SZ-250) and into a 41.6 L damping tank. The indoor air drawn through the filter is only loosely controlled, thus in order to allow correction of experimental data the pressure, temperature and humidity were measured twice daily near the intake air filter. Air leaves the damping tank through a 7.6 cm diameter tube, flowing past a hot-film mass air-flow meter and into the turbocharger compressor. Upon exiting the compressor the air is cooled by a water-to-air intercooler which is connected to the municipal water supply. To avoid condensing water vapor from the intake air the flow rate of water through the intercooler was adjusted to maintain minimum outlet air temperatures above 30 °C. The cool air is then reheated as necessary by a process air heater (Sylvania SureHeat 074728 10kW) which is controlled by a process controller to maintain a constant temperature at the inlet to the intake manifold. In the present research this temperature is maintained at 40 °C. The throttle is controlled electronically by the ECM which is in turn controlled by a computer console. The Intake manifold, and the entire intake air path are outfitted with pressure and temperature sensors of various types (cf. Figure 2-1). Temperatures are measured throughout by k-type (chromel-alumel) thermocouples and airflow pressures are measured by solid state diaphragm type absolute pressure transducers (Omega PX219) with the exception of the pressure measurement in the intake runner of cylinder number one which is a high speed miniature piezoresistive absolute pressure sensor (Kistler 4005B) connected to a piezoresistive amplifier (Kistler 4618A0). This sensor is used for adjusting relative cylinder pressure measurements to an absolute basis (a process frequently referred to as *pegging*). The entire complement of factory supplied sensors designed for use with this engine were maintained, such as the intake air temperature and manifold absolute pressure sensors. These sensors remained connected to the ECM and were not used for

data acquisition.

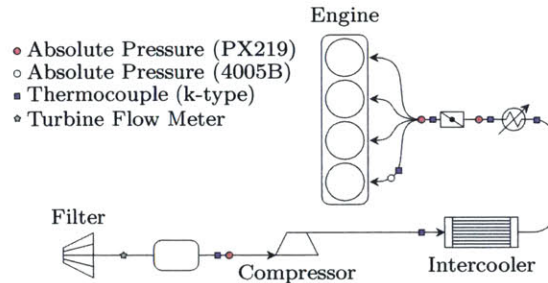


Figure 2-1: Positions of sensors in the intake air path. Only sensors connected to the data acquisition system are shown. The factory installed sensors connected to the ECM and used for engine control exist alongside these data acquisition sensors.

Fuel System

The LNF engine uses a high pressure direct injection system with a mechanically driven high pressure fuel pump delivering fuel at 31 bar to 155 bar to side-mounted injectors (cf. Figure 2-2). Under some operating conditions - generally at low engine speed and load - the spray interacts with a bowl in the piston to create a locally enriched mixture in the vicinity of the centrally located spark plug. The high pressure fuel pump, which is driven by the camshaft, is provided with fuel via a small (approximately 100 mL) damping reservoir located 15 cm from the pump inlet. The reservoir is fed by one of two parallel low pressure (4 bar) fuel systems which draw fuel from their respective fuel tanks (cf. Figure 2-3). Provisions for switching fuel systems and purging fuel lines are provided by a custom made fuel control panel installed immediately upstream of the high pressure fuel pump inlet reservoir. One tank and fuel system is reserved exclusively for use with Haltermann HF0437 EPA Tier III reference fuel, the primary fuel used in this research project. The HF0437 fuel is a high octane reference fuel with a RON of 96.6, a MON of 88.5 and a stoichiometric air fuel ratio of 14.6. The full specifications of the fuel are provided in the appendix. The secondary fuel tank is used for experiments requiring alternative fuels or blends such as PRF. Before the secondary tank was filled with a new fuel it was thoroughly washed and dried. The fuel lines were then purged and the engine was run for at least 20 min at 1500 rpm and 0.8 bar manifold pressure to remove any remaining fuel from the high pressure pump and fuel injector lines.

A calibration procedure was developed to estimate the mass of fuel injected into the cylinder based on the injection duration and fuel rail pressure reported by the ECM. Fuel was drawn from a flask with a small vent hole while the engine operated at constant injector pulse width and constant fuel rail pressure. The flask was positioned on an electronic scale and its weight was recorded every 150 s over a 15 min test. This procedure was repeated for a range of fuel pressures and injection durations to create a fuel delivery map. The fuel delivered is proportional to the injection pulse width for pulse widths greater than 500 μ s and scales with the root of fuel pressure. An injection



Figure 2-2: Diagram of the direct injection system on the LNF. Under some light-load conditions the side-mounted injector spray interacts with the piston bowl. During most high-load operation this interaction does not occur as the fuel is injected while the piston is lower in the stroke. Image © General Motors.

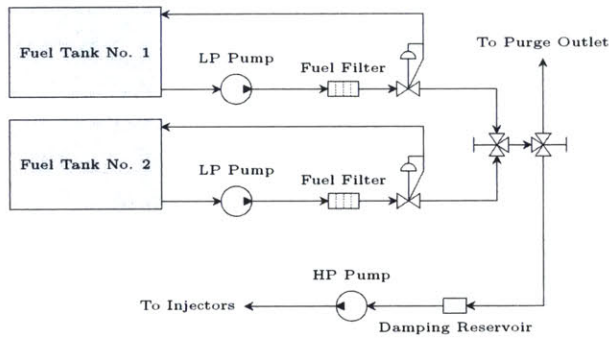


Figure 2-3: Diagram of fuel system. Fuel leaving either of the two tanks proceeds through a low pressure pump, secondary fuel filter and pressure regulator before reaching the fuel source selection valve. Fuel from the selected tank flows into a fuel delivery selection valve which directs the fuel to either a purge outlet or the engine. Fuel flowing to the engine enters a small damping tank before proceeding through the high pressure fuel pump. The high pressure fuel is then delivered to the direct injectors.

pulse width offset must be included to account for the valve opening and closing dynamics. The mass of delivered fuel is assumed to scale with fuel density provided the fuels are of similar viscosity. The amount of fuel delivered was computed using linear interpolation and the measured fuel delivery map. Alternatively, computing the quantity of fuel delivered using the measured flow rate of air and observed air fuel ratio generated fuel flow amounts that varied by less than 5% from the pulse width and pressure interpolation method.

In-Cylinder Measurements

Pressures within the cylinder were measured by piezoelectric cylinder pressure transducers (Kistler 6125A) which were equipped with flame arrestors. Sensors were installed in cylinders one and three at a location between the intake and exhaust valves in the cylinder head (cf. Figure 2-4). The charge output of the piezoelectric sensors was converted to a voltage output using a charge amplifier (Kistler 5010b). The natural frequency of the 6125 series pressure transducers exceeds 70 kHz and the charge amplifier was configured with a low-pass filtering cutoff frequency of 180 kHz. The cylinder pressure transducer and charge amplifier pair were calibrated for offset and linearity using a hydraulic dead-

weight tester with the sensor heated to 100 °C. Pegging of the cylinder pressure measurements was accomplished using the piezoresistive absolute pressure sensor in the runner of cylinder number one according to procedures designed to minimize experimental error^[56, 16, 11, 49].

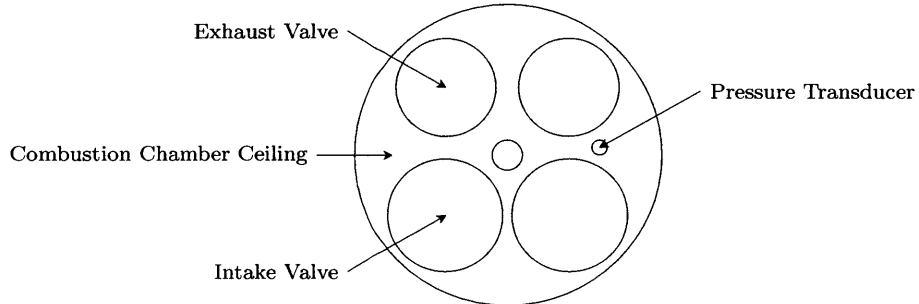


Figure 2-4: The cylinder pressure transducer is located within the cylinder head between the intake and exhaust valves. The transducer is approximately 20 mm from the cylinder wall.

Turbocharger and Exhaust System

The exhaust side of the cylinder head feeds a cast stainless steel exhaust manifold. The runners of cylinders one and four meet just upstream of the turbocharger flange and are separated from cylinders two and three. The twin-scroll turbocharger admits each stream separately and directs the exhaust flow through the appropriate scroll. The wastegate is integrated into the turbine housing and is actuated by an external solenoid. The pressure on the solenoid diaphragm is modulated by an electro-pneumatic solenoid valve controlled by the ECM. Base boost pressure, the pressure beyond which the wastegate will begin to open if the control solenoid is not energized, is approximately 1.2 bar. Beyond base boost the actuation duty cycle of the control solenoid must be increased to vent the pressure side of the diaphragm and thus hold the wastegate closed. A duty cycle of 100% on the boost control solenoid holds the wastegate closed regardless of boost pressure. During this research project the wastegate duty cycle was maintained at 100% throughout testing.

Temperature and pressure sensors are installed throughout the exhaust system. Temperatures are recorded in each exhaust runner and numerous downstream locations by k-type thermocouples (cf. Figure 2-5). Two wide band oxygen sensors are installed downstream of the turbocharger, one providing measurements to the ECM the other connected to the data acquisition system. The oxygen sensor connected to the data acquisition system is a Bosch LSU 4.2 type sensor connected to an ETAS UEGO controller, which provides a voltage that is proportional to the air-fuel equivalence ratio to the data acquisition system. Downstream of the oxygen sensors is the factory supplied close-coupled catalyst. Following the catalyst a fixed restriction, in the form of a gate valve, was adjusted to simulate the back pressure of an exhaust system and muffler. The pressure drop across the valve is approximately 35 mbar at 1500 rpm with an indicated power output of 35 kW. During experimentation the temperature at the inlet to the turbine was limited to 950 °C. This limit often

established the maximum amount of spark retard possible at a particular engine speed and load.

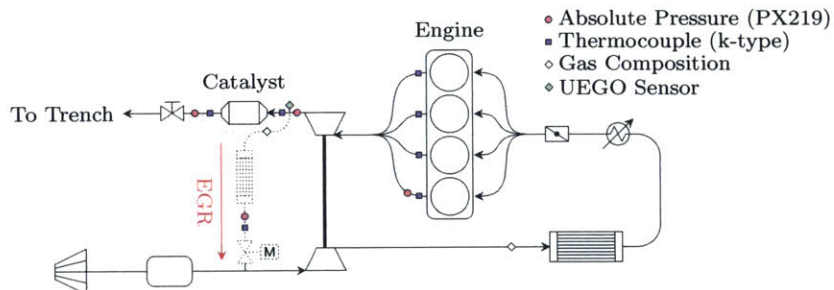


Figure 2-5: Positions and types of sensors in the exhaust and EGR system. The dotted line between the point just downstream of the catalyst and the EGR cooler represents an alternative configuration of the EGR loop that draws exhaust gasses from downstream of the catalyst.

Exhaust Gas Recirculation System

The LNF was not equipped with an EGR system from the factory, thus to meet the experimental demands of this research project a custom system was designed and constructed. The EGR system that was developed possesses several unique features. Foremost among these is a design that allows the location from which exhaust gasses are drawn to be modified within several minutes (cf. Figure 2-5). Two source locations were utilized, one immediately upstream of the close-coupled catalyst, and another immediately downstream. The change in source location was effected by placing a cap over the disused source location and installing a formed pipe between the desired source and the EGR cooler. After flowing from the selected source the exhaust gasses enter an EGR cooler. The cooler, originally from a Volkswagen Jetta TDI (engine code BRM), was adapted to the LNF engine. Engine coolant was circulated through the EGR cooler reducing the temperature of the exhaust gasses to approximately 100 °C. An electronic EGR valve originally from a Ford Fusion (Duratec 25 engine) was used to control EGR flow. Actuation electronics for the EGR valve were designed and built to allow the valve position to be adjusted from the data acquisition interface. The EGR valve delivers the recirculated exhaust just upstream of the turbocharger compressor inlet.

The composition of the exhaust gas was measured by a nondispersive infrared (NDIR) gas composition sensor (Horiba MEXA-554JU). Prior to analysis the exhaust was dried by passing it through a condenser chilled to 0 °C and a calcium sulfate based desiccant (Drierite 23005). The sensor therefore provides a measurement of volume fraction of carbon dioxide on a dry basis. The composition of the gasses entering the intake manifold were also measured by a NDIR gas composition sensor, however this sensor was custom made based on a standalone optical bench (PPSystems SBA-5). The custom sensor consisted of provisions for drying the sample, providing pure nitrogen for sensor calibration, and delivering a consistent volume flow rate of 400 mL min^{-1} at atmospheric pressure to the optical bench. Pressures at the pre-throttle sampling location ranged from 0.9 bar to 2.4 bar. The mass fraction of exhaust gasses in the fresh intake mixture was calculated from the two dry

measurements as

$$w_{egr,intake} = \frac{m_{egr}}{m_{air} + m_{egr}} \approx \frac{x_{co_2,intake,dry} - x_{co_2,atm,dry}}{x_{co_2,exhaust,dry}} \quad (2.1)$$

where m_i is the mass of component i and $x_{i,dry}$ is the mole fraction of component i after water vapor has been removed. The level of atmospheric CO₂ used was $x_{co_2,atm,dry} = 350$ ppm. This EGR rate approximation is based on the assumptions that the mole fraction of water vapor in the fresh air is small and the molecular weight of the recirculated exhaust is similar to the molecular weight of air. This approximation has been shown to be acceptable, particularly for EGR rates under 15 %. The dry mole fractions of CO₂ in the intake and exhaust are measured by the NDIR gas composition sensors. An *overall* EGR rate was then corrected to include the mass of fuel injected into the intake mixture and the residual mass fraction w_r according to

$$w_{egr} \approx \frac{w_{egr,intake}(1 - w_r)}{1 + \frac{1 - w_{egr,intake}}{\lambda(m_a/m_f)_s}}, \quad (2.2)$$

where λ is the air-fuel equivalence ratio and $(m_a/m_f)_s$ is the stoichiometric air-fuel ratio. Thus the EGR rate defined in Eq. 2.2 is the mass fraction of external EGR in the trapped charge and the total mass fraction of burned gasses in the trapped charge is $w_d = w_{egr} + w_r$.

Bottled Gas Addition System

The effects of specific gasses on combustion and autoignition was examined by supplementing the intake charge with various amounts of bottled gasses. In particular the effects of hydrogen, carbon monoxide and oxides of nitrogen were studied. These gasses were added individually to a point just upstream of the throttle plate (cf. Figure 2-6). A calibrated gas flow meter was used to introduce the bottled gas into the intake flow through a flame arrestor. For safety reasons the fuel gasses were added downstream of the air heater which was adjusted as necessary to maintain a constant temperature at the throttle plate.

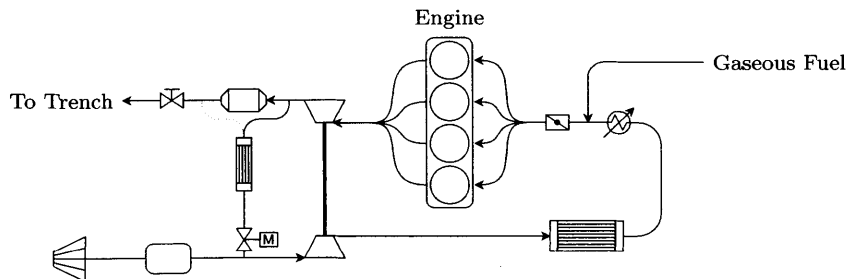


Figure 2-6: Gaseous fuels were added to a point in the intake path between the air heater and throttle plate. Fuel gasses were delivered through a flow proportioning valve and flame arrestor.

Cylinder Head and Valvetrain

The LNF is equipped with dual variable cam phasers. The cam phasers use oil pressure to adjust the phasing of valve opening and closing relative to crankshaft orientation (cf. Table 2.2). The phasers on the LNF are capable of adjusting both the intake and exhaust cam phasing by 50°. The majority of experimental data presented in this document was collected at fixed valve timing (cf. Table 2.3). This valve timing set point was based on the factory tuned valve timing at high loads and low engine speeds (approximately 1500 rpm, 1 bar manifold pressure). All opening and closing events quoted are evaluated using the 0.25 mm lift criterion. The crankcase ventilation system, which extracts gasses from the crankcase and cylinder head was vented to the atmosphere to prevent the contamination of intake air with oil vapor and crankcase gasses.

	Opening	Closing
Intake Parked	10° aTDC	60° aBDC
Intake Fully Phased	-40° aTDC	10° aBDC
Exhaust Parked	-50° aBDC	-10° aTDC
Exhaust Fully Phased	0° aBDC	40° aTDC

Table 2.2: The cam phasers can adjust the intake and exhaust cam phasing by 50°. The default or parked position of the intake and exhaust cams are given as well as the fully phased position. The intake cam timing is advanced and the exhaust cam timing is delayed with increased phaser activity.

	Opening	Closing
Intake	-32° aTDC	18° aBDC
Exhaust	-20° aBDC	20° aTDC

Table 2.3: Fixed valve timing values used to collect the experimental data presented in this document except where alternative valve timing is specifically stated. This cam phasing has moderate overlap at 52° using the 0.25 mm lift definition of opening and closing.

Cylinder Block and Crankshaft

All accessory loads were removed from the engine including the coolant pump, charging system and starter motor. The crankshaft was instrumented with an incremental optical quadrature encoder (BEI H25) which provided 360 pulses per revolution. Using a custom made processing circuit the quadrature signal is decoded into two digital output channels. The first channel provides one rising edge every 0.25° of crank rotation while the other provides a rising edge at bottom dead center (BDC) of the compression stroke. The encoder was aligned to match the dynamic location of top dead center (TDC) combustion for cylinder one with 180° using a capacitive TDC sensor (AVL TDC Sensor 428).

2.2 Dynamometer and Auxiliary Systems

The engine test bench is equipped with several pieces of equipment necessary for safe and reliable engine operation. The dynamometer, which is connected to the flywheel via an output shaft with

flexible couplings, absorbs and dissipates power produced by the engine. An electric drive motor is also connected to the engine output and is capable of rotating the engine in the absence of combustion. The electric motor is also used in the place of a starter motor. Heat rejected by the engine is carried away by the cooling system which is designed to stabilize coolant temperature and performs the functions of the water pump, radiator and thermostat.

Dynamometer

The dynamometer is of the eddy-current type and is rated up to 150 kW and 500 N m (SAJ SE150). Cooling is provided by a filtered municipal water supply. The dynamometer is connected to a dynoamometer controller (Dyne Systems Dyn-Loc IV) which is capable of maintaining either speed or load constant during engine operation. Torque sensing is provided by a strain gauge based load cell which was calibrated in accordance with manufacturer recommended procedures. Throughout the experimental testing carried out for this research project the dynamometer was operated in constant speed mode. The maximum engine output is higher than the rated load of the dynamometer (190 kW compared to 150 kW) which limited the range of speeds and loads that could be studied.

Electric Motor

A 40 hp electric motor (Baldor Electric Inverter Drive Motor) is used for starting the engine and sensor calibration procedures that call for rotation of the crankshaft in the absence of combustion, such as identifying TDC using a capacitive sensor. The motor is driven by a variable speed motor controller (Yaskawa Varispeed F7). When not in use the motor, while electrically neutralized, still imposes a friction load on the output of the engine which is not measured by the dynamometer. As such the brake torque measured by the dynamometer is expected to read lower than the actual torque output. Due to this unknown contribution of the electric drive motor to friction, brake torque measurements were not used outside of providing a qualitative measure of engine output.

Cooling System

The modified engine cooling system consists of an engine coolant loop, which is filled with a blend of ethylene glycol and distilled water in equal parts (cf. Figure 2-7). The thermostat was removed from the engine allowing coolant to be pumped through the engine by an external, electrically powered centrifugal pump. The coolant reservoir is equipped with electrical heaters for warming the coolant and provisions for draining the cooling system. Coolant entering the tank flows through a water to coolant heat exchanger which uses the municipal supply to reduce coolant temperature. A process controller is used to maintain the coolant temperature in the tank at 80 °C with a tolerance of ±1 °C. After coolant flows through the engine it is directed through the EGR cooler, heat exchanger and

returned to the tank.

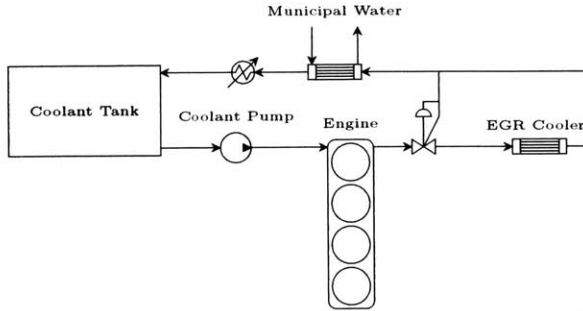


Figure 2-7: Diagram of the cooling system used with the LNF engine. Coolant is supplied from a tank and a portion of the flow through the engine is directed through the EGR cooler. The coolant temperature is reduced using a heat exchanger fed with municipal water or increased using an electric heater.

2.3 Data Acquisition and Processing

The data acquisition and processing system used during the course of this research consists of three distinct components, the engine control system, the data acquisition system and the data processing system. The first component, the engine control system, is centered around the ECM and is responsible for reading all sensors and driving all of the actuators required to operate the engine. The second component, the data acquisition system, is independent of engine control and consists of all of the sensors, hardware and software required to quantify the operational characteristics of the engine. The third component, the data processing system, is a set of code, written predominantly in MathWorks MATLAB that is used to extract and interpret data collected by the acquisition system. The engine control system and data acquisition system are run simultaneously and share information during operation of the engine. The data processing system is used when the engine is offline to view and manipulate the experimental data.

Engine Control System

The engine control system consists of the hardware and software necessary to operate the engine. The center of this system is a development ECM (Bosch ETKP 4.0) which is connected to a computer workstation using an ethernet data communication interface (ETAS ES591.1) that allows ECM parameters to be modified during operation of the engine using ECM tuning software (ETAS Inca 6.2). The ECM interfaces with the engine systems through all of the factory-supplied sensors and actuators. Power to the fuel injectors and ignition system are routed through a safety disconnect and to the control panel as a means of enabling or disabling the firing of the engine. Parameters of the ECM were adjusted to achieve the desired operating conditions such as air-fuel equivalence ratio, throttle position, spark timing and valve timing. During stoichiometric operation ECM modulation

of the air fuel ratio was enabled which results in variations in the air-fuel equivalence ratio (λ) of ± 0.02 with a frequency of 1.5 Hz.

Data Acquisition System

The data acquisition system collects measurements from a set of sensors that is largely independent of those used to operate the engine. Sensors are connected to a modular data acquisition system (National Instruments cDaq 9188) which relays sampled data via ethernet to a computer workstation. The eight slots of the modular data acquisition system (DAQ) were outfitted with several analog (5X NI 9215) and thermocouple (NI 9213) input modules as well as digital input-output ports (NI 9401 and NI 9402). The maximum sampling frequency of analog signals is 100 kHz, simultaneous sampling across all channels. Data acquisition code was developed using National Instruments LabView 2009. Under steady state conditions the code was configured to collect data for 100 cycles sampling every 0.25° of crank rotation. Immediately following the crank angle resolved sampling, data was collected for 100 cycles while sampling at 100 kHz. Sampling steady state data as both time and angle resolved measurements aids in the accurate evaluation of measures such as mean effective pressure (MEP) (which requires known positions) and knock intensity (which requires temporal filtering). The simultaneous sampling of both crank angle and time resolved data for the same cycle was not possible due to hardware limitations. End to end calibration was performed on all pressure and temperature sensors and these calibrations were periodically verified.

A data communication interface between ETAS Inca and NI LabView was developed using the ASAM-3MC protocol to allow data that is difficult to measure directly but known by the ECM to be saved during data collection. Fuel pressure, injection duration, spark timing and valve timing were passed from Inca to LabView during data collection. A phase delay inherent to the ASAM-3MC protocol makes it impossible to assign the transmitted data to a specific cycle, however these parameters are either constant at steady state or only required as mean values.

The data collection interface developed for this research project provides the operator with a wide array of information during engine operation. The most recent cylinder pressure measurements are shown for cylinders number one and three as well as the preceding nine cycles for each cylinder which are shown with progressively lower opacity. A pressure-volume diagram is also constructed for cylinder number one which is updated every cycle. The air-fuel equivalence ratio, EGR rate, fuel delivery rate, emissions and various temperatures are shown alongside load metrics such as the net and gross indicated MEP and manifold air pressure. The communication interface with Inca is used to allow basic commands such as increment spark timing to be sent from the LabView interface. When the operating conditions are deemed satisfactory for data collection a *save data* button is pressed which temporarily suspends the display of data and allocates computing resources to the transfer and transcription of information transmitted by the DAQ.

A new data output format was developed within LabView to increase the rate and precision at which data could be stored. The format links measurements to their units and creates a data structure that may be extended arbitrarily to meet changing experimental demands without damaging existing data processing code. The format stores data in binary, which being identical to the format used by LabView to store data in computer memory, may be very quickly copied to a hard disk as it requires no additional manipulation or computation. Storing data in this format allows memory to be written to a file and cleared at a rate exceeding the collection rate and thus avoids any potential for memory overruns or loss of data.

Data Processing System

A newly developed data processing library, written in MATLAB, simplifies the access and manipulation of the experimental data stored in binary form. Procedures were coded to perform common analyses such as computing the heat release during combustion using the Rassweiler-Withrow method^[51] and determining the gross and net indicated mean effective pressure (MEP). A description of the binary file format and selected data extraction and processing code is provided in the appendix. Although the majority of data processing is accomplished using MATLAB, specialty engine simulation software (Gamma Technologies GT-Suite) is used under some circumstances to estimate parameters that cannot be measured directly using the research apparatus.

2.4 Experimental Procedures

Procedures were developed to ensure uniformity of experimental data. The three most pertinent procedures are the start of day calibrations and measurements, the engine warmup procedure and the method of collecting data over a range of spark timing values.

Start of Day

At the beginning of the day, while the engine is cool, environmental parameters are measured and sensing systems are checked. First the temperature and humidity are measured using a sling psychrometer and recorded. The atmospheric pressure measured by an outdoor weather station approximately 250 m from the engine is also recorded. The data acquisition system is powered on and all of the sensed pressures and temperatures are plotted in real time using a LabView interface developed specifically for this purpose. The measured temperature and pressure are entered into the interface and any sensors that do not agree with these measurements within their margin of error are examined and calibrated. The Horiba NDIR is calibrated and zeroed using a bottled mixture of gasses of known proportions and atmospheric air. The custom built NDIR is zeroed using high-purity nitrogen at the start of the day and every 30 min from then on. The ice bath used to dry

exhaust gasses is filled and the desiccant for both NDIR devices is renewed if necessary.

Engine Warmup

The coolant temperature process controller and coolant pump are enabled which begins to warm the coolant and circulate it through the engine. Communication between the ECM and computer console is then established. The control valves for the municipal water supply are opened providing cooling water to the dynamometer, intercooler and cooling system. The engine coolant is warmed to operating temperature by starting the engine. First the electric motor is used to rotate the engine at 1200 rpm with the ignition and fuel system disabled. Once engine speed has stabilized the dynamometer is activated with a set speed of 1190 rpm. If the dynamometer engages and the ECM reports no faults the ignition and fuel systems are activated and the engine begins firing. At this point the electric motor is deactivated and the engine is operated at 1200 rpm and 0.5 bar manifold pressure until the coolant comes up to operating temperature (generally 80 °C).

Spark Timing Sweep

The majority of the experimental data presented in this document was collected as part of a spark timing sweep. Before beginning a sweep of spark timing the engine was allowed to stabilize for a minimum of 10 min. Temperature stability in the exhaust system generally exhibited the largest time constants and thus these temperatures were monitored during the stabilization process. Data was collected at the stabilized operating point and as spark timing was advanced control parameters were adjusted to maintain either constant fuel delivery rate or constant net indicated mean effective pressure (NIMEP). The engine was allowed to stabilize between increments of spark timing for a minimum of 2 min or as required for the exhaust temperatures to reach equilibrium. The spark timing was advanced by the minimum amount possible, which for this ECM is 0.75°. The spark timing was progressively advanced until a state of heavy knock was reached. Heavy knock was identified by observing fluctuations in cylinder pressure of ± 5 bar.

Chapter 3

Effects of EGR Source on Engine Operation

Until recently the choice of the location from which exhaust gasses are drawn by the exhaust gas recirculation (EGR) system has been made based largely on thermal, packaging and corrosion constraints. However, research published within the last several years has indicated that extracting the exhaust gasses from upstream of the catalytic converter may provide beneficial effects, particularly with respect to the autoignition tolerance of the engine^[52, 5]. Such an implementation presents practical difficulties due to the potential formation of nitric acid in exhaust condensate when oxides of nitrogen are present in moderate levels. If exhaust gasses are extracted from a post-catalyst location the weakly basic ammonia formed from oxides of nitrogen that have been reduced in the catalyst presents less severe durability concerns. In order to make an informed decision regarding the selection of EGR implementation the advantages and disadvantages of each topology must be studied quantitatively, which is the aim of this effort.

This chapter begins by identifying the compositional differences between pre-catalyst and post-catalyst sourced exhaust gasses and ties these differences to changes in combustion that have been observed in the literature. Experimental testing is then used to identify critical differences in the physical behavior of the engine under varying EGR source conditions. Following the identification of changes in engine behavior due to physics an examination of differences that can be attributed to charge chemistry is performed. The analysis presented in this chapter shows that under typical conditions the effects of chemical differences in the recirculated exhaust gas are small in comparison to the effects caused by alteration of the exhaust flow dynamics.

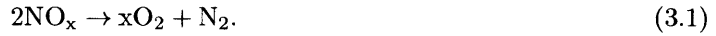
3.1 Recirculated Exhaust Composition

The contents of the exhaust have been modeled and measured by many methods^[29]. The treatment presented here is intended to summarize the key components of the exhaust flow and highlight differences that may occur depending on the regime of engine operation and the location in the exhaust system.

Stoichiometric Mixtures

Combustion of a stoichiometric mixture of air and fuel results in the formation of two ideal products, namely water vapor (H_2O) and carbon dioxide (CO_2). However, combustion of a stoichiometric mixture generally results in small amounts of carbon monoxide (CO), hydrogen (H_2) and oxides of nitrogen (NO_x) along with small quantities of oxygen and hydrocarbons that escape combustion due to mixture nonuniformity and quenching of the flame near crevices within the engine^[29]. The largest individual constituent of the exhaust gas is atmospheric nitrogen (N_2) which along with atmospheric carbon dioxide and water vapor pass through the engine largely unaffected.

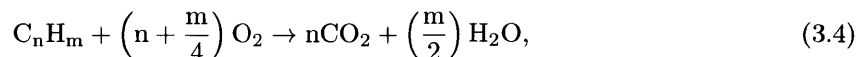
The three way catalyst performs a set of complementary reactions that are intended to eliminate components of the exhaust that are damaging to the environment or result in adverse health effects. Specifically the catalyst reduces oxides of nitrogen to oxygen and molecular nitrogen by the catalytic reaction



In the presence of hydrogen gas some of the oxides of nitrogen may react to form ammonia^[54] by



which from a practical perspective is a less favorable reaction due to the basic nature of ammonia. Both of these reactions are only favored if the partial pressure of oxygen is sufficiently low. Using the oxygen liberated by these reactions along with any oxygen that may have escaped combustion carbon monoxide, hydrogen and hydrocarbons are fully oxidized in the reactions



Because this set of reactions consists of both reduction and oxidation reactions it is only favorable in a narrow range of air-fuel ratios near stoichiometry. If the catalyst is functioning properly levels

of NO_x, CO, H₂ and hydrocarbons in the exhaust will be reduced by several orders of magnitude, from their already low molar concentrations below 1%. In their place are the considerably more inert N₂, CO₂, H₂O and NH₃.

Comparing the pre-catalyst and post-catalyst exhaust content for stoichiometric operation identifies three constituents that are largely eliminated in the post-catalyst stream. From highest to lowest molar concentration these are carbon monoxide which may be in the range of 0.75%, molecular hydrogen is generally present at one half to one third of the carbon monoxide concentration in automotive engines or roughly 0.25% and oxides of nitrogen – the presence of which is strongly temperature dependent^[13] – are generally measured at concentrations near 0.1% at moderate loads and stoichiometric conditions in the experimental engine. Together these components make up roughly 1% of the exhaust by volume. Using these concentrations and the assumption that no hydrocarbons are present in the exhaust the fraction of energy leaving the engine as combustible species may be compared to the energy of the fuel consumed. Such an analysis indicates that 2.6% of the fuel energy is leaving the engine in the form of CO and 0.75% leaves in the form of H₂. The combined chemical energy in the exhaust of 3.4% is referred to as the combustion inefficiency, which is defined by Heywood^[29] as,

$$1 - \eta_c = \frac{\sum_i x_i Q_{LHV,i}}{[\dot{m}_f / (\dot{m}_a + \dot{m}_f)] Q_{LHV,f}}, \quad (3.6)$$

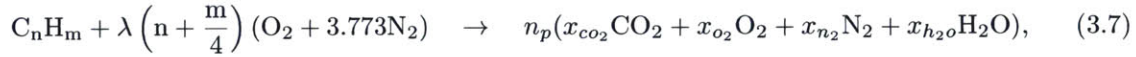
where η_c is the combustion efficiency, x_i is the mass fraction of combustible species i in the exhaust, $Q_{LHV,i}$ is the lower heating value of species i , $Q_{LHV,f}$ is the lower heating value of the fuel and \dot{m}_f and \dot{m}_a are the mass flow rates of fuel and air into the engine. Combustion inefficiencies of two to four percent are common for lean or stoichiometric mixtures with the inefficiency increasing rapidly to approximately 30% at an air-fuel equivalence ratio of 0.8 ($\lambda = 0.8$). Although the energy content of hydrogen is much higher than carbon monoxide per unit mass converting the heating values to kJ mol⁻¹ reveals that the carbon monoxide value of 283 kJ mol⁻¹ is not substantially different from the hydrogen value of 240 kJ mol⁻¹. This implies that the ratio of carbon monoxide to hydrogen energy is similar to the ratio of carbon monoxide to hydrogen volume. Using the experimentally observed volume ratios of 2 to 3 yields energy ratios between 2.3 and 3.5.

Due to combustion stability issues it is difficult to operate spark ignited automotive engines when burned gasses make up much more than 25% of the cylinder contents. Thus if the preceding analysis is continued with 25% exhaust gas recirculation one would expect that of the 3.4% fuel energy leaving in the exhaust approximately 0.85% of the fuel energy makes it back into the charge in the form of carbon monoxide and hydrogen. Under moderate to high load conditions the fuel delivered per cylinder per cycle in the LNF is approximately 48 mg, thus the additional fuel energy provided by the recirculated exhaust is expected to equate to approximately 0.4 mg of fuel, which is on the order of cycle-to-cycle variations in fuel delivery. Generally such a small fraction of additional fuel would not be considered capable of altering overall combustion stability and engine behavior

however two considerations raise the possibility that such a small change may have an observable effect. First, hydrogen and carbon monoxide differ considerably from the raw hydrocarbon fuel. In particular flames in hydrogen-air mixtures burn considerably more quickly than hydrocarbon-air mixtures^[4, 7]. This fact has led some to propose that small amounts of supplemental hydrogen may improve combustion stability and speed. The second consideration is that when the engine is operated with high rates of exhaust recirculation the combustible charge is diluted significantly. This dilution alters the speed and behavior of the flame, reducing the overall rate of combustion.

Fuel Lean Mixtures

For mixtures that have excess oxygen the overall combustion reaction can be expressed as



where λ is the air-fuel equivalence ratio, x_i is the mole fraction of component i and n_p is the total number of exhaust products in mol. Here the amounts of hydrogen, carbon monoxide, unburned hydrocarbons and oxides of nitrogen have all been assumed to make up a negligibly small part of the exhaust mixture. If the fuel characteristics (n and m) and the equivalence ratio (λ) are known this equation possesses five unknowns. Five equations can be generated by balancing the reaction for carbon, hydrogen, oxygen and nitrogen then recognizing that the mole fractions of the products sum to unity.

The principle feature of interest in the composition of lean exhaust is the unburned oxygen content (cf. Figure 3-1). As the air-fuel equivalence ratio is increased (and the mixture is made leaner) the burned portion of the exhaust gas composition does not change appreciably. Instead this burned portion is merely diluted by an unburned quantity of air (oxygen and nitrogen). When the engine is operated lean with EGR a portion of the excess air in the charge comes from the EGR mass flow and the remainder from the environment.

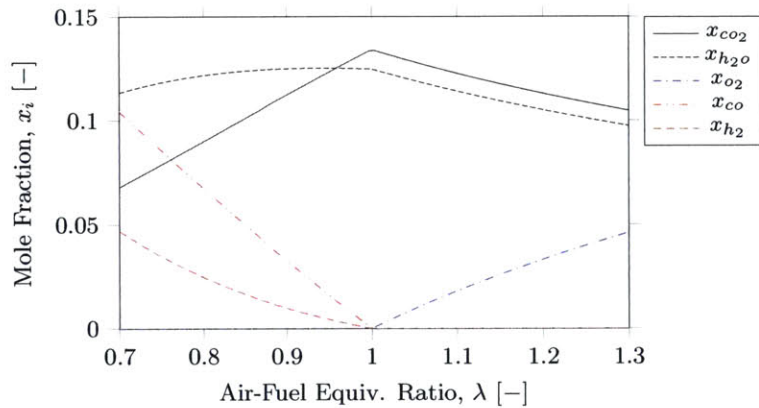
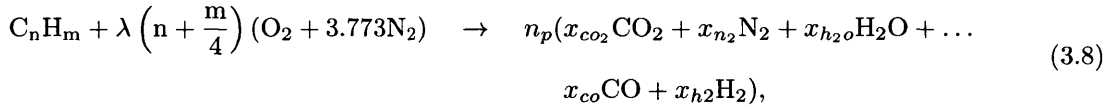


Figure 3-1: The mole fractions of carbon dioxide, water vapor, oxygen, carbon monoxide and hydrogen as a function of air-fuel equivalence ratio.

Fuel Rich Mixtures

When there is fuel in excess of the amount that can be fully oxidized with the available air a considerable portion of the fuel energy may leave the cylinder in the form of combustible species. During rich operation the idealized combustion reaction is



where the concentrations of oxygen, unburned hydrocarbons and oxides of nitrogen in the exhaust have been neglected. Here there are six unknowns, five of which can be eliminated as with the lean case by balancing the reaction for carbon, hydrogen, oxygen and nitrogen and recognizing that the mole fractions of products add to unity. The final unknown may be eliminated by employing an empirical relationship based on the water-gas shift relationship,

$$\frac{x_{CO}x_{H_2O}}{x_{H_2}x_{CO_2}} \approx 3.8. \quad (3.9)$$

The composition of the exhaust during rich operation has several features that are of interest. First, as the mixture is enriched the amount of fully oxidized products – namely CO₂ and H₂O – decreases considerably, being replaced by partially oxidized products such as CO and H₂. The majority of the chemical energy remaining in the exhaust is in the form of carbon monoxide, which makes up approximately three quarters of the energy content while the remaining one quarter is in the form of hydrogen. Under very rich conditions nearly 30% of the fuel energy may leave in the form of combustible species. When an EGR system is used during rich operation it is conceivable that up to 7.5% of the fuel energy could be introduced in the form of carbon monoxide and hydrogen however it is essential to recognize that under these operating conditions the energy content of the fuel in excess of the amount required to fully oxidize the available air will be several times larger than this figure.

3.2 Thermo-physical Effects of EGR Source

The installation of an EGR system on an engine has widespread effects on its operational characteristics. The *thermo-physical effects* are those related to changes in flow dynamics, system pressures, turbocharger behavior and other processes that are governed by thermodynamic or physical principles exclusive of combustion. A key characteristic these effects, which will be discussed shortly, is that their occurrence is not limited to situations in which the EGR system is in use.

Installation Effects

Changes in engine behavior caused by the installation of an EGR system were studied by performing a series of experiments in which the EGR cooler and connective tubing were installed in either the pre-catalyst or post-catalyst position with the EGR valve sealed and disconnected from the intake. Additional tests were also performed in which the entire EGR system was removed. In each configuration the engine was operated under stoichiometric conditions at 1500 rpm with a fuel flow rate of 140 g min^{-1} , nominal valve timing (cf. Table 2.3) and a range of spark timings. The results of this spark sweep indicate that the net indicated fuel conversion efficiency is reliably higher when the EGR system is installed in the pre-catalyst location than when it is installed in the post-catalyst location or removed entirely (cf. Figure 3-2).

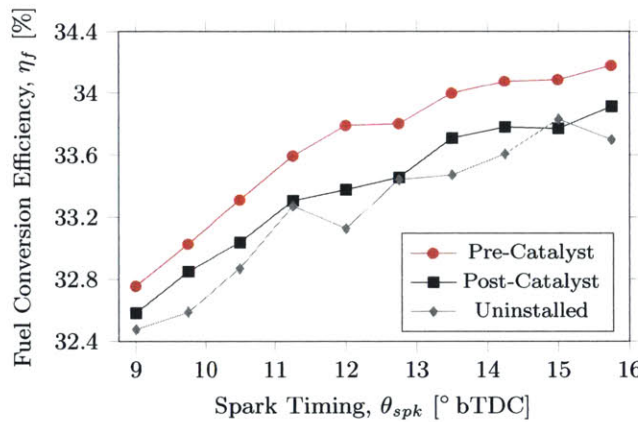


Figure 3-2: A spark sweep performed with the EGR system installed in the pre-catalyst location results in a higher net indicated fuel conversion efficiency than when the EGR system is installed in the post-catalyst configuration or removed entirely. This installation effect occurs in the absence of recirculation flow (with the EGR valve fully closed).

A close comparison of representative cylinder pressure measurements obtained at a spark timing of 13.5° bTDC indicates that the majority of the efficiency improvement in the pre-catalyst configuration is due to overall higher cylinder pressures (cf. Figure 3-3). A lesser improvement may be attributed to a reduction in the pumping work caused by an increase in manifold pressure. Although these changes may appear slight the result is a change in fuel conversion efficiency on the order of 0.5% which is comparable to the efficiency improvements that one might expect from the use of an EGR system – yet the observed change in efficiency was developed in the absence of any EGR flow. It is therefore essential that the cause of these changes be clearly identified as a failure to do so may result in the attribution of efficiency improvements to EGR that are truly due to the alteration of the exhaust system.

Pressure measurements from within the cylinder and the intake and exhaust runners provide the first indications that the difference in engine behavior when the EGR hardware is installed may be due to a change in charge composition. During blowdown and the exhaust stroke cylinder and

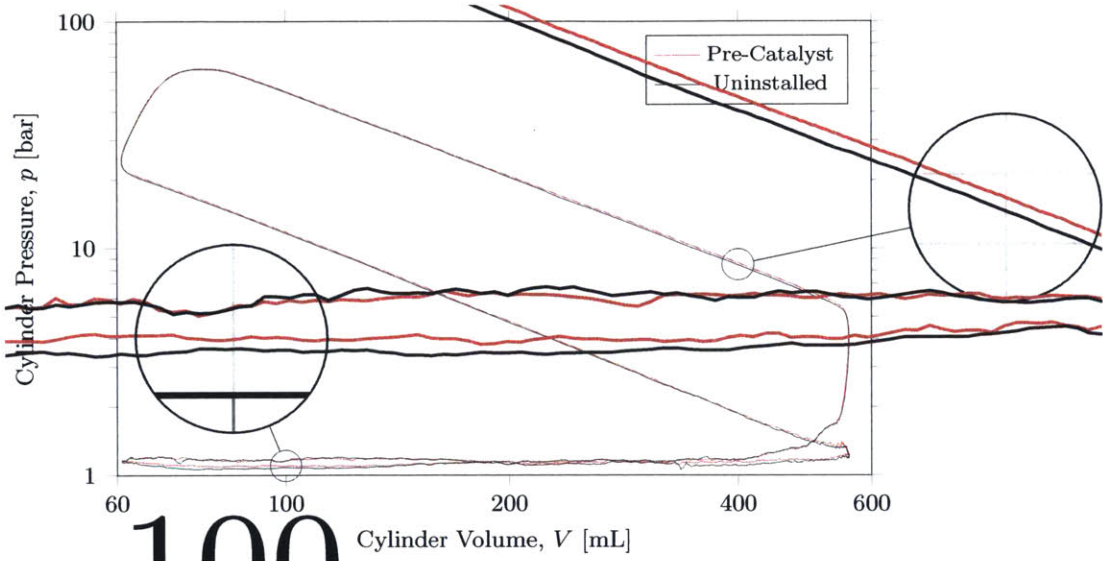


Figure 3-3: The majority of the efficiency improvement realized by installing the EGR system in the pre-catalyst location is attributable to an overall increase in pressures in the pre-catalyst configuration. This potentially indicates a change in charge composition.

exhaust runner pressures follow similar trajectories for both the pre-catalyst installation and the uninstalled case. However, during the later half of the exhaust stroke cylinder and exhaust runner pressures for the pre-catalyst installation take on slightly higher values than the uninstalled case. At 32° bTDC the intake valve opens to a pressure that is higher than the exhaust pressure (cf. Figure 3-4). The pressure differential without the EGR system installed is more favorable for scavenging than the pre-catalyst installation, presenting the possibility that the residual fraction may be higher when the pre-catalyst EGR system is installed. In both cases before the exhaust valve closes at 20° aTDC the pressure differential across the valve changes sign, indicating that some reverse flow of burned gasses may occur with this cam timing.

A change consistent with an increase in residual fraction that is observed when the EGR system is installed in the pre-catalyst location is the increase in manifold pressure required to consume the same quantity of fuel. The increase in manifold pressure is achieved by increasing the boost pressure generated by the compressor. In order to accomplish this the pressure ratio across turbine must be increased (the corrected mass flow does not change appreciably). Increasing the pressure ratio results in higher pre-turbine pressures which drives further increases in the residual fraction. This feedback mechanism is a complex function of valve timing, turbocharger characteristics, and exhaust system aerodynamics. The slight reduction in the polytropic exponent during the expansion process is also consistent with an increase in the residual fraction which for the same mass of fuel and air tends to reduce heat transfer transfer.

An examination of pressure measurements across the turbocharger reveals that when there is no EGR system installed high frequency pressure oscillations occur in the exhaust runner (cf. Figure 3-5). The level of pressure oscillations is significantly reduced when the EGR system is installed

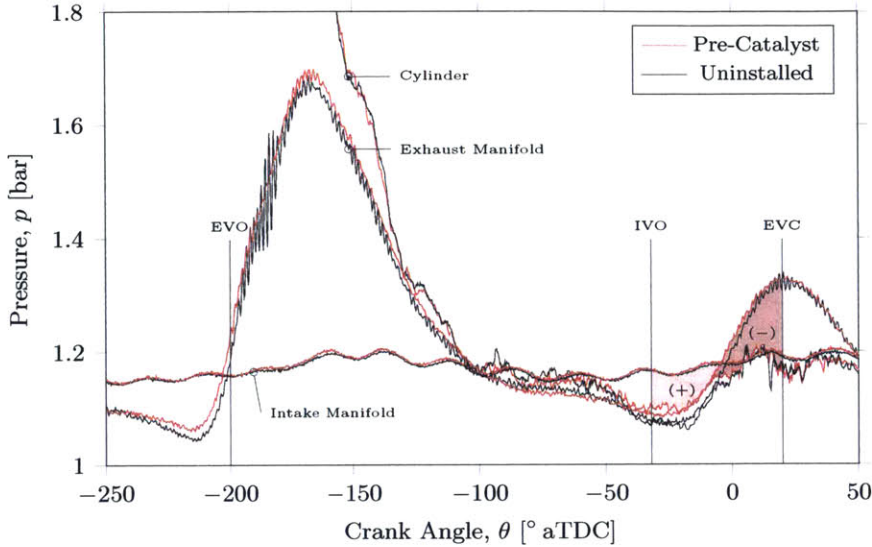


Figure 3-4: The blowdown and scavenging characteristics of engine change when the EGR system is installed in the pre-catalyst location. During valve overlap the positive pressure differential across the intake valve is reduced (area indicated by a +) while the area of a negative pressure differential across the exhaust valve is increased (area indicated by a -). These two changes tend to cause a higher fraction of residuals to be trapped due to less effective scavenging during the + region and increased reverse flow across the exhaust valve during the - region.

in the pre-catalyst location. The precise cause of these oscillations is not known however several observations may be made. The oscillation frequency appears to be identical to the rotational frequency of the turbine, which in this case is rotating at approximately 86.4 krpm and the measured magnitude of the pressure oscillations is largest during the blow down of cylinder number four. These characteristics suggest that the cause of the pressure oscillations may be related to cylinder to cylinder interaction within the scroll of the turbocharger. Under the test conditions it is worth noting that the turbine is operating at a low pressure ratio and low mass flow compared to its design specifications which is likely to result in low turbocharger efficiency. When the EGR system is installed the pressure ratio across the turbine is increased due to an increase in pre-turbine pressure and reduction in post-turbine pressure. This moves the turbine operating point to a slightly higher pressure ratio which is likely to improve turbine efficiency.

Altogether the changes that occur when the EGR system is installed are predominantly related to the flow dynamics within the exhaust. However, due to several features of modern engine designs – specifically the presence of the turbocharger and operation of the engine with substantial valve overlap – changes in the exhaust have the potential to alter charge composition and engine efficiency. The testing performed here provides a snapshot of the EGR system installation effects under a particular set of conditions, revealing that changes in engine behavior induced by the additional volume added to the exhaust system has effects that cannot reasonably be neglected. As engine speed and load are altered the effects of the additional exhaust volume are expected to change. This sensitivity to exhaust system configuration makes the comparison of alternative EGR installations

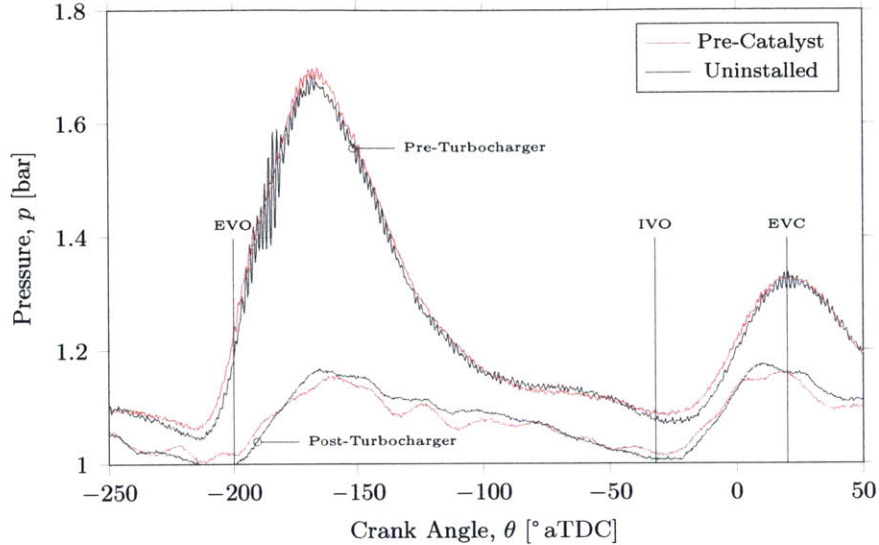


Figure 3-5: The pressure drop across the turbocharger is larger over the majority of the blowdown event when the EGR system is installed in a pre-catalyst location. The post-turbine pressure does not rise as high as when the EGR system is not installed. During the energetic blowdown phase pressure oscillations occur when no EGR system is installed that are largely eliminated when the EGR system is installed in a pre-catalyst location. The pressure oscillations may be caused by cylinder interactions within the scroll of the turbocharger, which is operating near the surge limit.

difficult because the engine must be tuned to provide an identical charge when the configuration is changed, a requirement which may entail modification of valve timing, throttle position or turbocharger wastegate settings.

Intake and Exhaust Pressure Modification

A feature of EGR systems touched upon in the previous discussion is that the inclusion of an EGR loop has the potential to reduce pressures in the exhaust system. The mechanism that drives this reduction is related to pulsating exhaust flow. Under the conditions of the previous section if an EGR system is installed in the pre-catalyst location the pressures observed within the EGR loop assume a characteristic sinusoidal shape (cf. Figure 3-6). These oscillations are caused by exhaust flow entering the EGR loop volume during periods of elevated pressure and leaving when the pressure falls. This tends to smooth fluctuations in both the velocity of exhaust flow and the pressure at the point to which the EGR system is connected. If smoothing of this type is introduced upstream of the catalyst the pressure drop across the catalyst, which is proportional to the square of flow velocity, is reduced. Such reductions may also be realized across a muffler or exhaust system, however the magnitude of the improvement will be reduced as the magnitude of flow oscillations is damped further down the exhaust system.

The reduction of pre-catalyst pressure, which increases the pressure ratio across the turbine, also depends on the position of the EGR valve. If the EGR valve is fully open the effective volume of the

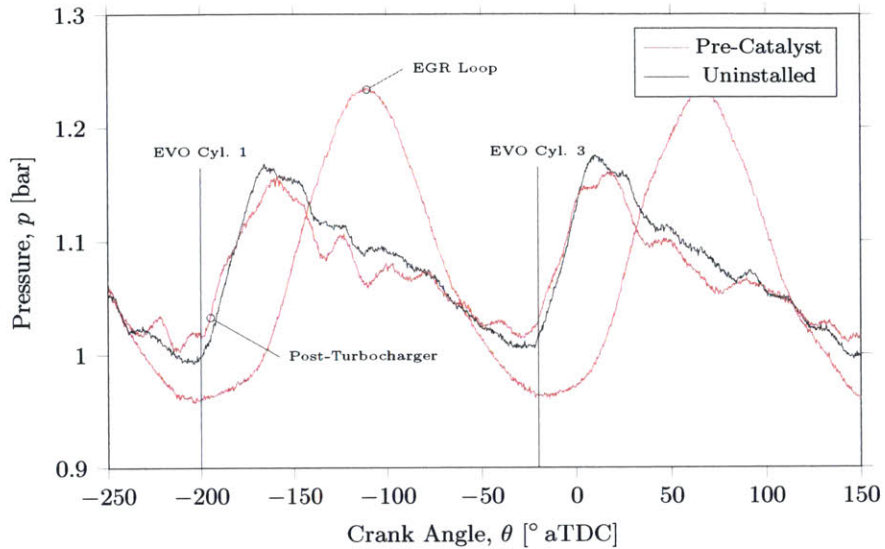


Figure 3-6: The pressures measured when the EGR system is installed in the pre-catalyst location indicate that during the early phase of the blowdown there is flow into the EGR loop volume. During the later part of the blowdown and the exhaust displacement stroke the pressure in the EGR loop exceeds the post-turbine pressure and mass flows out of the EGR loop through the catalyst. Compared to the pressures observed when no EGR system is installed the amplitude of pressure fluctuations due to pulsating flow observed just upstream of the catalyst is reduced.

EGR loop is increased and the pressure and flow fluctuations that occur at the entry to the EGR loop are reduced to lower levels. This effect, when combined with the increases in turbine mass flow that occur at high external EGR rates indicate that the operating point of the turbocharger may be altered considerably by the installation and use of an EGR system. Use of EGR necessitates operation at higher intake manifold pressures to achieve the same mass flow rate of either air or fuel through the engine. These higher intake manifold pressures result in a reduction in the amount of pumping work which may make up a considerable fraction of the efficiency improvements afforded by the installation of an EGR system^[18].

3.3 Combustion Effects of EGR Source

The identification of the sizable role of installation effects – those changes in engine behavior caused by the mere installation of EGR hardware – complicates the comparison of alternative EGR systems considerably. Changes made in the exhaust system, due to the feedback action of the turbocharger, cause further changes in the intake and charge, driving the engine to a distinct set of steady-state conditions. Since the steady state condition reached is governed by a complex feedback system composed of the engine, turbocharger, exhaust and intake it is difficult to recover identical operating conditions when changes are made to the exhaust. Thus comparisons based on experimentation using a turbocharged engine – such as the comparison presented here – must be considered as lower fidelity than a comparison made in an apparatus that is capable of isolating the charge preparation and

inlet conditions from changes that may occur in the exhaust. However, a compensatory feature of studying the behavior of EGR systems as they are frequently installed is that the system-level response of the engine may be observed and quantified.

This section will begin by examining the characteristics of pre-catalyst sourced EGR with regard to changes in charge properties that affect combustion or efficiency. This will be addressed by first identifying changes that occur at fixed combustion phasing – as measured by the crank angle of fifty percent heat release (CA50) – when the EGR rate is increased. Next an examination of changes in the autoignition behavior will be performed and the improvements in efficiency afforded by the possibility of more favorable combustion phasing will be quantified. Following the completion of this analysis an identical procedure will be performed for post-catalyst sourced EGR and the results will be compared.

Pre-Catalyst EGR

The experimental data presented in the analysis that follows was collected at 1500 rpm with a fixed fuel flow of 140 g min^{-1} , nominal valve timing (cf. Table 2.3) and a range of spark timing settings, air-fuel ratios and EGR rates. The EGR system was configured to extract exhaust gasses from a location upstream of the catalyst – just downstream of the turbocharger (cf. Figure 3-7). At each EGR set point a spark sweep was performed, advancing the spark until moderate knock was encountered. The range of possible EGR rates is limited by either the pressure differential across the EGR loop or the intake manifold pressure required to achieve the desired fuel flow rate.

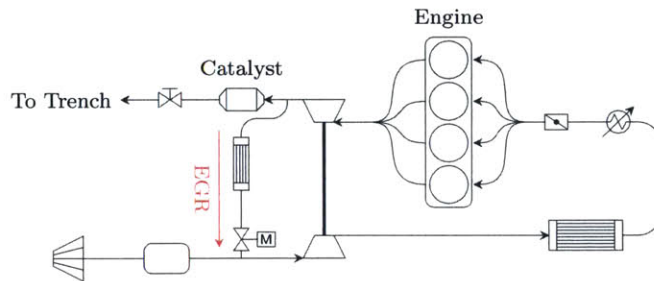


Figure 3-7: Configuration of EGR loop for *pre-catalyst* EGR.

Based on the previous description the data collected can be considered to exist in a three dimensional test matrix where the dimensions are:

1. Air-fuel ratio
2. EGR rate
3. Spark timing

The majority of data processing tasks were performed by compressing the third dimension (spark timing) by aggregating all of the experimental cycles at a given air-fuel ratio and EGR rate. A

heat release analysis was then performed on the aggregated cycles based on the method developed by Rassweiler and Withrow^[51]. This allowed the crank angles of ten, fifty and ninety percent heat release ($\theta_{10\%}$, $\theta_{50\%}$ and $\theta_{90\%}$ respectively) to be identified for each cycle. Much of the data presented will be expressed as a function of $\theta_{50\%}$ without specific regard for the spark timing that happened to induce this combustion phasing. This approach was adopted in order to reduce the influence of cycle-to-cycle variation in combustion phasing on the parameters being studied. Metrics such as the gross indicated mean effective pressure (GIMEP) were also computed on a cycle-resolved basis and the data was reduced by computing the mean value of the GIMEP within a CA50 window with a width of 1° (cf. Figure 3-8).

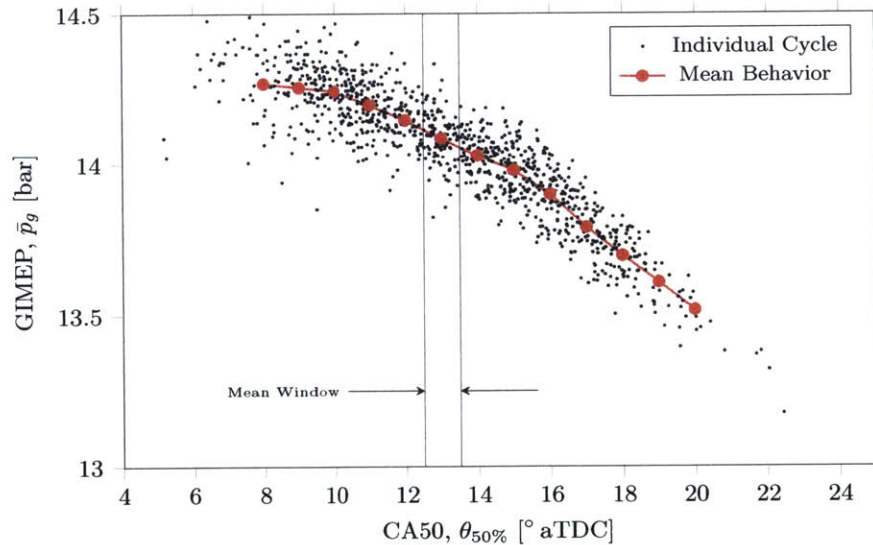


Figure 3-8: Data is reduced by computing the mean value within a CA50 window. The window width used is 1° and windows that do not contain at least 15 cycles are neglected. The data shown here represents a range of spark timing values between 9.75 °bTDC and 16.5 °bTDC under stoichiometric conditions with no EGR.

Stoichiometric Behavior

The performance of the EGR system under stoichiometric conditions represents the operating state of the highest practical importance, thus it is sensible to start with a detailed analysis of the stoichiometric behavior before moving on to other air-fuel ratios. A characteristic that is often associated with dilution of a charge by burned gasses is a reduction in the rate of heat release, or stated differently an increase in the burn duration. The burn duration, which is quantified as

$$\Delta\theta_{10\%-90\%} = \theta_{90\%} - \theta_{10\%}, \quad (3.10)$$

or the difference between the crank angles of 90% and 10% heat release, is a function of both CA50 and EGR rate (cf. Figure 3-9). The experimental data shows that the burn duration is considerably

more sensitive to CA50 than it is to the EGR rate. For a particular spark timing $\theta_{50\%}$ may vary by $\pm 4^\circ$ or more corresponding to burn duration variations on the order of $\pm 2^\circ$. In comparison the increase in mean burn duration from 0% to 10% EGR is on the order of 2° under these experimental conditions. At fixed CA50 the burn duration appears to increase uniformly with increasing EGR rates beyond 1.25% (cf. Figure 3-11).

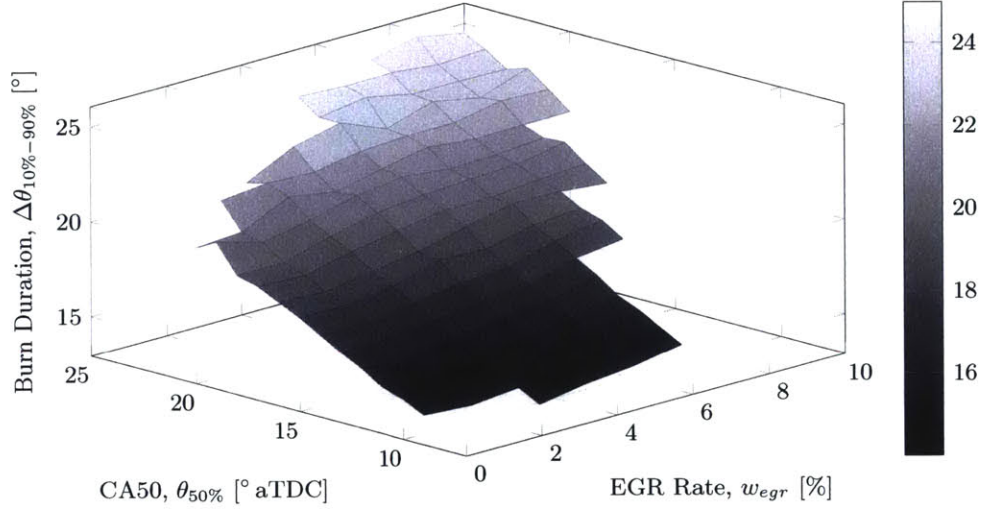


Figure 3-9: As indicated by this surface plot the burn duration is more heavily dependent on CA50 than EGR rate. Nevertheless increasing the EGR rate does result in an increase in the burn duration as expected.

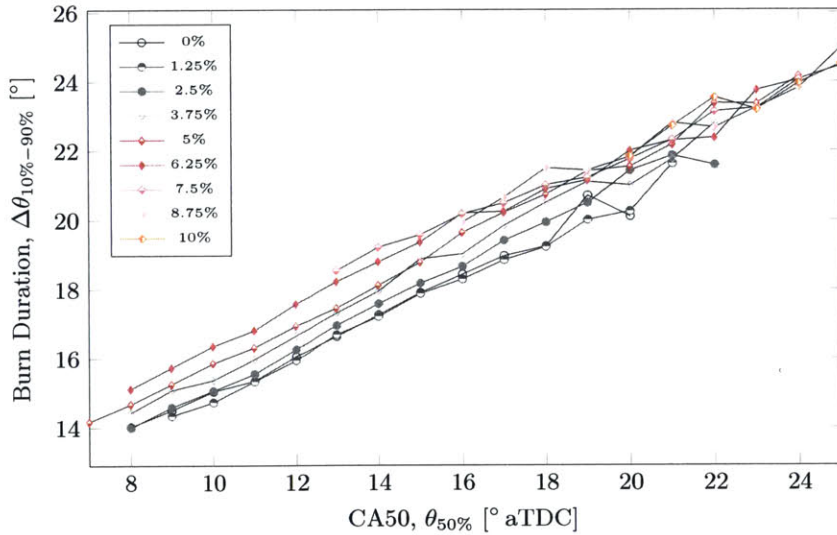


Figure 3-10: Under the conditions studied the burn duration increases by 2° when the EGR rate is increased from 0% to 8.75% at fixed CA50. The increase in burn duration does not appear to be a strong function of combustion phasing. The increased scatter on the upper right side of the plot is due to increases in cycle to cycle variation at late combustion phasing.

To interpret these findings it is helpful to characterize the relationship between the commanded spark timing and the realized CA50 (cf. Figure 3-12). The relationship between these two parameters is subject to considerable cycle to cycle variation as illustrated in the figure, however the trends

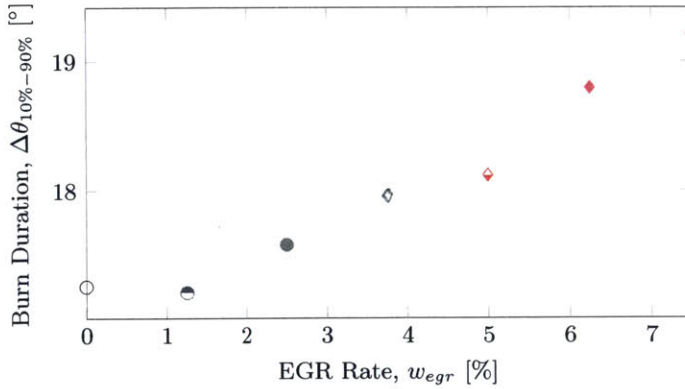


Figure 3-11: The burn duration at fixed CA50 of 14° aTDC increases uniformly for EGR rates higher than 1.25%. The magnitude of the observed changes in burn duration is on the order of 2° for a change in EGR rate of 8.75%.

produced are clear. Increasing the EGR rate at fixed spark timing increases the CA50 by 3° to 4° for a change in the EGR rate of 10%. At late combustion phasing the increase in CA50 at fixed spark timing when EGR is introduced is larger than near maximum brake torque (MBT) timing. This is due to increased cycle-to-cycle variation at late CA50, particularly with high EGR rates. As with the burn duration the rate at which spark timing must be advanced to maintain fixed CA50 when EGR is introduced is relatively stable between 0% and 10% EGR. The spark advance required to maintain constant CA50 over this EGR range is just over 2° under most conditions. Because the burn duration also increases on the order of 2° over this EGR range at constant CA50 it is apparent that the addition of EGR affects the early stages of flame development. If the heat release rate profile is approximately symmetric about CA50 then 1° of spark advance accounts for the change in the 10% to 50% burn duration while the remaining 1° must arise from an increase in the crank angle duration between the spark timing (θ_{spk}) and the crank angle of 10% heat release ($\theta_{10\%}$). Based on the experimental data the split between $\Delta\theta_{spk-10\%}$ and $\Delta\theta_{10\%-50\%}$ is uniform until very late combustion phasing – more than 20° aTDC – at which point a slightly larger increase in $\Delta\theta_{spk-10\%}$ is observed.

The ultimate purpose of introducing EGR at high engine loads is to increase the efficiency of the engine. This may be accomplished either by improving the thermodynamic characteristics of the charge, such as the specific heat ratio, or by decreasing the likelihood of autoignition at a particular combustion phasing by reducing charge temperatures. The latter mechanism only provides a method of improving efficiency if the CA50 is restricted to values later than the CA50 of MBT due to autoignition. Plotting the GIMEP as a function of CA50 over all of the EGR rates reveals that under these conditions the GIMEP is not particularly sensitive to changes in the EGR rate (cf. Figure 3-13). In fact the data indicates that contrary to the expected behavior the GIMEP is reduced by approximately 0.7% as the EGR rate is increased from 0% to 2.5%.

The apparent reduction in efficiency from the zero EGR case appears to be the result of more

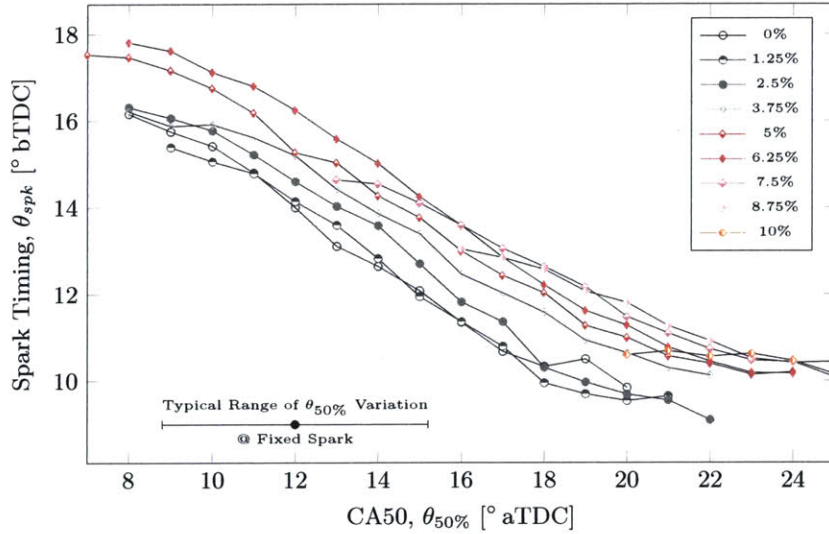


Figure 3-12: The relationship between spark timing and CA50 appears to be uniform over the range of EGR rates and combustion phasing values studied. The spark timing must be advanced just over 2° to maintain constant CA50 when the EGR rate is increased from 0% to 10%. The range of variation in CA50 that is observed at constant spark timing is considerable which complicates the interpretation of data that is presented with spark timing as the abscissa.

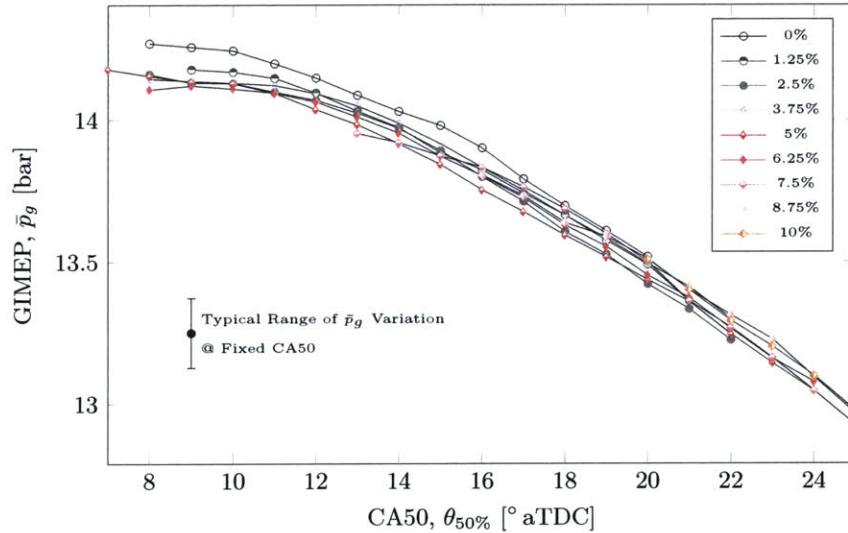


Figure 3-13: The GIMEP plotted as a function of CA50 shows only a slight dependence on EGR rate. The reduction in peak GIMEP from the 0% EGR case is accounted for by a reduction in the combustion efficiency.

complete combustion of the air-fuel mixture under the heavily knocking conditions present near MBT timing with no EGR. An analysis of the pre-catalyst emissions indicates that under these heavily knocking conditions levels of CO and unburned hydrocarbons are lower while levels of CO₂ are higher in spite of an increased coefficient of variation (COV) of GIMEP. The change in combustion efficiency that can be attributed to the change in CO emissions is given by

$$\Delta\eta_c = -\frac{\Delta x_{co} Q_{LHV,co}}{[\dot{m}_f / (\dot{m}_a + \dot{m}_f)] Q_{LHV,f}}. \quad (3.11)$$

Between 0% and 1.25% EGR at $\theta_{50\%} = 12^\circ$ aTDC the change in engine out CO mole fraction is approximately $\Delta x_{co} = 10^{-3}$ which yields $\Delta \eta_c = -0.004$ or equivalently -0.4% . If similar changes were to occur in the hydrogen and hydrocarbon emissions it is likely that the efficiency reduction of 0.7% observed in the data could be attributed to a reduction in combustion efficiency alone.

As for the lack of efficiency improvement with increasing EGR rate the data indicates that peak pressures do not increase until beyond 6.25% EGR as they would be expected to do with increasing charge mass. This is believed to be caused by a combination of two factors:

1. Increasing the manifold pressure in order to increase the EGR rate tends to reduce the trapped residual fraction by improving the effectiveness of scavenging. Because the residuals are at high temperature reducing the residual fraction has the effect of decreasing trapped charge mass and temperature and increasing charge density. This is accompanied by a reduction in pre-compression pressures within the cylinder.
2. If residuals – sometimes referred to as internal EGR – are reduced at the same time that the rate of external EGR is increased changes in the total burned gas mass fraction will be smaller than the changes in the external EGR rate. This reduces the changes in specific heat ratio which according to simulations are responsible for approximately 40% of the improvement in gross efficiency^[30].

These two changes both tend to reduce the magnitude of differences in the cylinder pressure when the external EGR rate is increased. Cycle simulations performed in GT-Power on a calibrated engine model indicate that between 2.5% and 6.25% external EGR the residual fraction decreases by 0.5% while the charge temperature at intake valve closing is reduced by 8K. Combining these effects with an ideal gas model of the charge indicates that the increase in cylinder pressure at IVC with the additional 3.75% external EGR is reduced from approximately 3.7% to 0.8%. Depending on the residual temperatures and the amount of residuals displaced per unit of additional external EGR. It is conceivable that cylinder pressures may be reduced as the external EGR rate is increased. This effect, which appears to be important where engine speeds are low and residual fraction is high, may be reduced by optimizing the valve timing to control residual fraction independently of EGR rate.

In order to properly examine the potential efficiency improvements afforded by the use of EGR for autoignition mitigation the tolerable maximum levels of autoignition must be well defined. Many measures of autoignition have been proposed, the majority of which rely on either accelerometer or cylinder pressure data^[46, 42]. For the purpose of the present analysis a metric based on cylinder pressure proves most practical, and a simple metric often referred to as the *knock intensity* was used. The knock intensity (KI) is calculated by high-pass filtering cylinder pressure data and determining the peak amplitude of the pressure oscillations induced by autoignition. The filter used was a digital phase-preserving high-pass filter with a cutoff frequency of 2.5 kHz. The knock intensity was

defined for every cycle and cycles that exhibited a $KI \geq 1$ bar were considered knocking cycles. At steady state (with fixed spark timing) the cycle-to-cycle variations in knock intensity exhibit a strong (although not definitive) correlation with CA50 – a topic which will be discussed in the following chapter – thus when analyzing autoignition results the use of CA50 over spark timing as the abscissa provides a more distinct transition between non-knocking and knocking behavior.

The knock limit may be expressed in terms of either the CA50 or the spark timing at which it occurs. For the present work the knock limited CA50 is taken as the more fundamental parameter and it is defined as the CA50 at which 10% of the observed cycles exhibit $KI \geq 1$ bar and is given the symbolic name $\theta_{50\%}^k$. The spark timing that is associated with this CA50 is determined by interpolation of the mean relationship between spark timing and CA50 under a given set of conditions (cf. Figure 3-12). This definition of the knock limited spark advance (θ_{spk}^k) is more aggressive than some adopted in the literature because use of this spark timing implies that half of the cycles will have a probability of knock greater than 10% while the other half will have a probability less than 10%. In practice this means that the probability of knock at the knock limited spark advance will most likely be in the range of 10-50%. If a less aggressive knock limit is desired the knock limited spark advance may be altered to reflect the expected range of variation in CA50 at fixed spark timing. To achieve a low probability of knock it is necessary to retard the spark timing such that $\theta_{50\%}^k$ falls just outside the 95% confidence interval of CA50 variation. Mathematically this may be expressed as

$$\theta_{spk}^{kc} = \theta_{spk}^k - \frac{\partial \theta_{spk}}{\partial \theta_{50\%}} 2\sigma_{CA50}, \quad (3.12)$$

where θ_{spk}^{kc} is a conservative knock limited spark timing and σ_{CA50} is the standard deviation of CA50 at fixed spark timing. The partial derivative of spark timing with respect to CA50 is frequently near unity thus it suffices to retard the spark by approximately two times the standard deviation of CA50 which depends on the operating conditions of the engine but is generally around 3° . Equivalently one may also consider a conservative knock limited CA50 as one approximately 3° later than $\theta_{50\%}^k$.

For the data set presently being analyzed the changes in efficiency – and therefore GIMEP – due to changes in thermodynamic properties of the charge has been observed to be small. The present analysis seeks to quantify the magnitude of efficiency improvements afforded by knock mitigation. The efficiency improvements promised by EGR may be decomposed into two effects, efficiency improvement at fixed CA50 due to changes in thermodynamic properties or efficiency improvements afforded by the ability to operate at more favorable combustion phasing (cf. Figure 3-14). An examination of the experimental GIMEP data (cf. Figure 3-13) reveals that the MBT combustion phasing is not sensitive to changes in EGR rate thus to present improvements due to autoignition mitigation it is acceptable to normalize the curves by MBT output, thereby collapsing all EGR rates to a single

curve. The collapsed normalized GIMEP curve was created based on functional form

$$\frac{\bar{p}_g}{\bar{p}_{g,MBT}} = 1 - 0.168 \left(\sqrt{1 + 4.44 \times 10^{-3}(\theta_{50\%} - \theta_{50\%,MBT})^2} - 1 \right) \quad (3.13)$$

which has been observed to accurately model the reductions in load caused by non-optimal combustion phasing^[8]. The optimal combustion phasing was identified as $\theta_{50\%,MBT} = 7.6^\circ$ aTDC. The translation of the knock limited CA50 along this collapsed curve as EGR rate is increased quantifies the fractional improvement in GIMEP due to autoignition mitigation (cf. Figure 3-15). This plot highlights the effect of knock avoidance strategy. Using the more realistic conservative CA50 limits the improvement in GIMEP is 1.4% compared to a 0.8% improvement using the more aggressive limit of the knock limited CA50. Comparing the change in GIMEP achieved by the knock abatement qualities of EGR to those generated by the changes in thermodynamic characteristics indicates that under these conditions knock avoidance is the dominant method by which GIMEP may be improved.

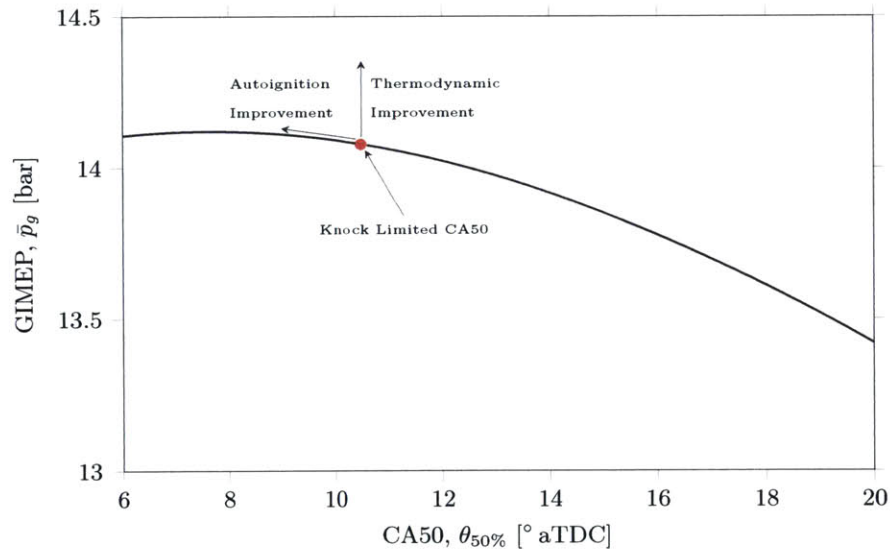


Figure 3-14: The efficiency improvements that are offered by EGR take the form of improvements that alter the thermodynamic characteristics of the charge and improvements that alter the autoignition behavior, which allow more favorable combustion phasing.

The change in the knock limited CA50 may be translated to a change in spark timing using the relationship between CA50 and spark timing previously developed (cf. Figure 3-12). If the change in the knock limited CA50 is defined as the difference between the knock limited CA50 for the zero EGR case and the knock limited CA50 then,

$$\Delta\theta_{50\%}^k = \theta_{50\%}^k|_{\text{NO EGR}} - \theta_{50\%}^k, \quad (3.14)$$

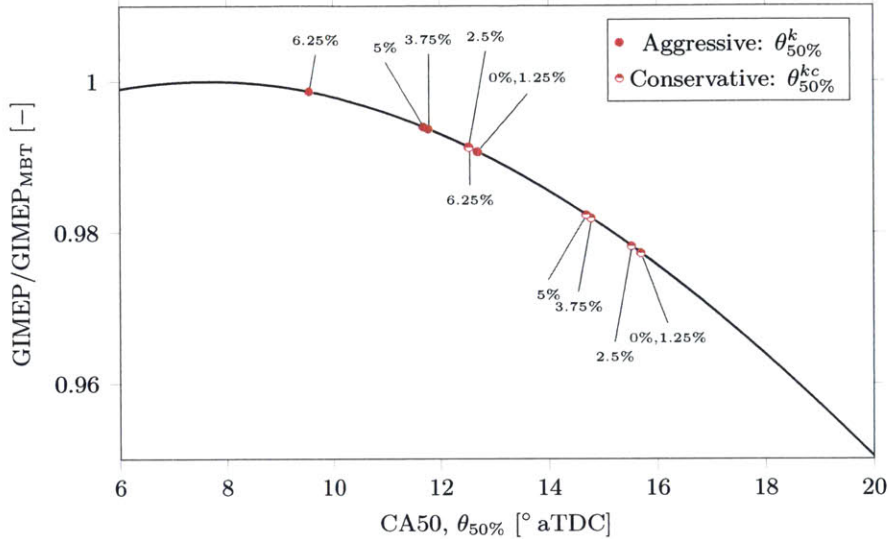


Figure 3-15: The knock limited CA50 is indicated on a normalized plot of GIMEP. Increasing the EGR rate from 0% to 6.25% decreases the knock limited CA50 by just over 3°. If a conservative strategy is adopted as would be required in a production engine due to cycle-to-cycle variation in CA50 the improvement in GIMEP is approximately 1.4%. The *aggressive* CA50 limit indicates the CA50 at which the engine could operate with only 10% knocking cycles if there was no cycle-to-cycle variation in CA50.

and if the change in knock limited spark advance is similarly defined as,

$$\Delta\theta_{spk}^k = \theta_{spk}^k \Big|_{\text{NO EGR}} - \theta_{spk}^k, \quad (3.15)$$

these two values may be compared to determine whether changes in the spark timing are used to compensate for changes in combustion phasing due to slower burn or to advance the CA50 due to higher knock tolerance. The Δ values defined above are defined such that advancing the spark or the CA50 results in a positive Δ value. Plotting the experimental data over all of the EGR rates for which the knock limit could be reached indicates that initial changes to the spark timing are used purely to recover the same combustion phasing with no material improvement in the autoignition limits (cf. Figure 3-16). However, beyond 2.5% EGR the spark advance is used almost exclusively to advance the CA50 to take advantage of improved knock resistance. This is possible because as the CA50 is advanced to take advantage of the autoignition margin burn duration tends to be reduced, however increasing the EGR rate tends to increase the burn duration these two effects nearly cancel resulting in relatively small changes in the burn duration at knock.

Rich Operation

When the charge is enriched slightly ($\lambda = 0.95$) similar trends of engine behavior are observed. In particular efficiencies are slightly reduced during the initial stages of EGR introduction, after which time MBT efficiencies stabilize (cf. Figure 3-17). An examination of the burn durations indicate that overall changes between the stoichiometric and rich cases are quite small (cf. Figure 3-18). At

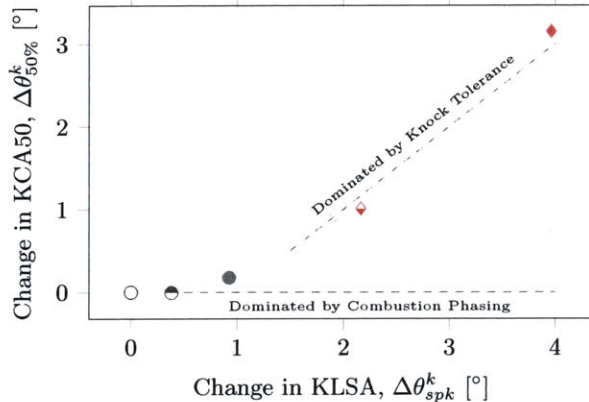


Figure 3-16: As EGR is first introduced the initial effect is to slow the early phases of flame development without changing the knock limited CA50. However, beyond EGR rates of 2.5% the majority of the spark advance is used to advance the CA50 to take advantage of the improved knock tolerance of the charge.

higher EGR rates (beyond 7.5%) the burn duration appears to stabilize (cf. Figure 3-19) however because such EGR rates could not be reached at the same combustion phasing for stoichiometric conditions it is not known whether this is a characteristic unique to rich EGR. Higher EGR rates were possible during rich operation because the mass flow rate of fuel was fixed, thus less air is required to achieve $\lambda = 0.95$ than $\lambda = 1$, allowing more of the available boost pressure to be used to accommodate EGR.

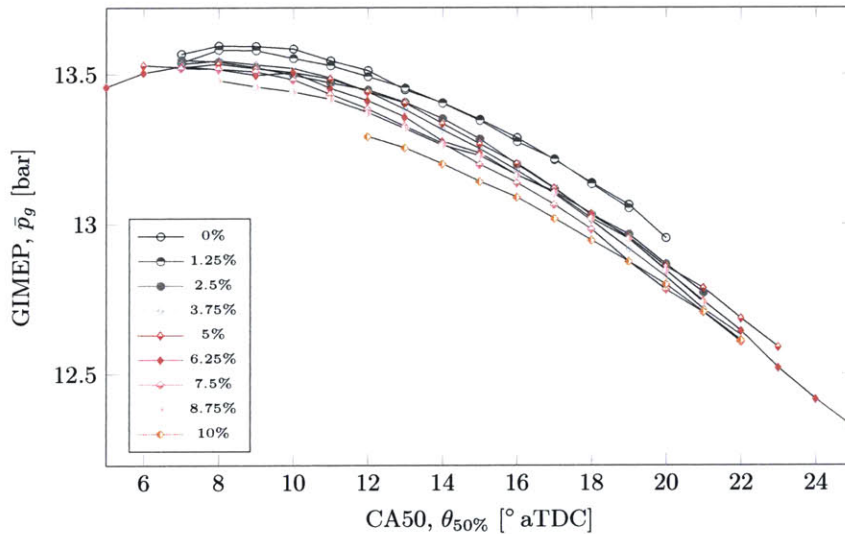


Figure 3-17: During rich operation ($\lambda = 0.95$) the response of GIMEP to increasing EGR rates is similar to the stoichiometric case. MBT output appears to decrease with increasing EGR rate.

As for the autoignition characteristics of rich EGR a distinction must be made between changes induced by overall modification of the air-fuel ratio and differences in the composition of the EGR. When the engine is operated under rich conditions the excess fuel acts as a diluent and post-compression temperatures are reduced due to a reduction of the specific heat ratio. Both of these changes reduce the likelihood of autoignition at a particular CA50. These changes result in the

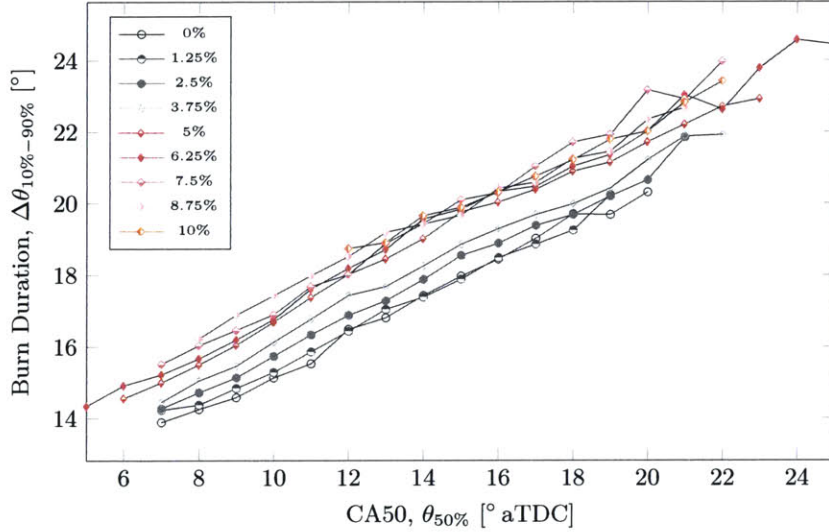


Figure 3-18: Burn duration are very similar between rich and stoichiometric operation (cf. Figure 3-10), although a larger range of EGR rates was possible.

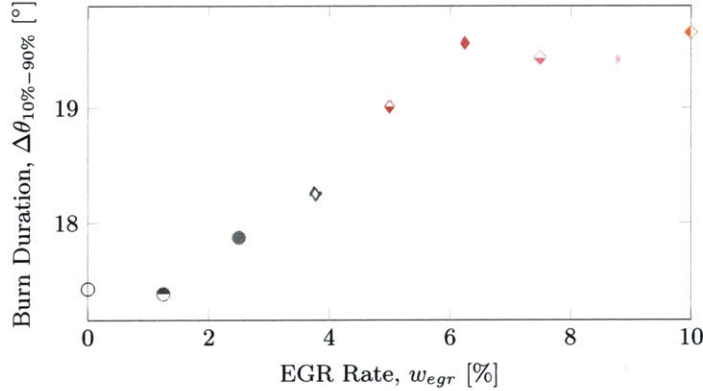


Figure 3-19: The burn duration at a fixed combustion phasing of 14° aTDC increases along similar lines as the stoichiometric case, however beyond 7.5% EGR the burn duration appears to stabilize. Because such EGR rates could not be obtained at this combustion phasing it is not known whether this is a feature unique to rich EGR.

knock limited CA50 being advanced from 12.7° aTDC to 11.1° aTDC when λ is reduced from 1 to 0.95 for the zero EGR case. Since MBT timing is not sensitive to this change in air-fuel ratio one may suspect that all other factors being equal the improvements in GIMEP will be smaller for the rich case as the partial derivative of GIMEP with respect to CA50 ($\partial \bar{p}_g / \partial \theta_{50\%}$) approaches zero as CA50 moves towards MBT.

The autoignition data indicates that over the same range of EGR rates (0-6.25%) the knock limited CA50 advances only 2° compared to the 3° observed for stoichiometric operation, however the change in the knock limited spark advance remained the same at 4° (cf. Figure 3-20). This means that more of the spark advance has been used to counter changes in combustion phasing than the stoichiometric case, with relatively less improvement in the knock limited CA50. The reduced ability to advance CA50 at the same dilution rate may indicate that rich EGR is less beneficial for knock

abatement than stoichiometric EGR. However, the knock limited CA50 has already been advanced 1.6° due to the change in air-fuel ratio which has resulted in an increase in peak cylinder pressures at the knock limit. The change in efficiency observed for rich EGR is reduced in comparison to the stoichiometric case due to the reduced change in the knock limited CA50 and the more advanced CA50 at zero EGR (cf. Figure 3-21).

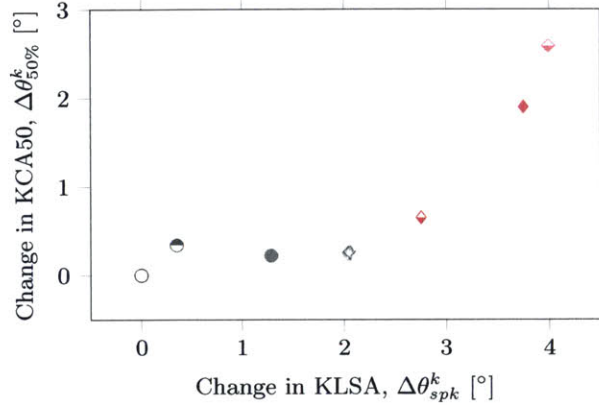


Figure 3-20: The change in knock limited spark advance up to 6.25% EGR is very close to the change observed under stoichiometric conditions, however the change in the knock limited CA50 is reduced from 3° in the stoichiometric case to 2°. This may indicate that at the same dilution rate rich EGR provides less knock abatement however the fact that the knock limited CA50 has already been advanced 1.6° due to the change in air-fuel ratio may contribute to this difference in behavior.

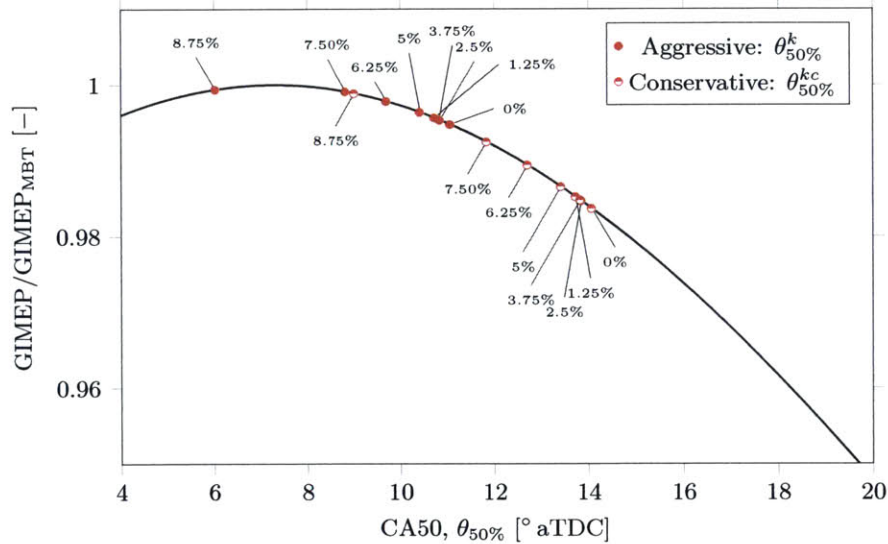


Figure 3-21: The smaller change in knock limited CA50 and more optimal initial combustion phasing under rich operation mean that improvements in GIMEP are smaller than the stoichiometric case.

Post-Catalyst EGR

As discussed in the section on the installation effects of EGR systems, attempting to draw a direct comparison between alternative EGR installations that are operated with the same engine parameters

ters – particularly valve timing – is an endeavour that may prove nearly intractable due to feedback effects of the turbocharger. Instead the best that can be done, short of developing a specially designed test apparatus, is to compare changes in behavior relative to the zero EGR case. The GIMEP data indicates that MBT combustion phasing is not altered appreciably from the pre-catalyst conditions (cf. Figure 3-22). However, the knock limited CA50 at the zero EGR is also advanced considerably – 8.2° aTDC for the post-catalyst case compared to 12.7° aTDC in the pre-catalyst configuration. The peak cylinder pressures drop by approximately 3 bar which may indicate that either the residual fraction has been reduced or a portion of the fresh charge is being lost through scavenging during the valve overlap period. The exhaust temperature is reduced at similar combustion phasing and temperature measurements throughout the exhaust indicate that post-cylinder oxidation – as indicated by the temperature rise across the catalyst – is increased from the pre-catalyst EGR conditions.

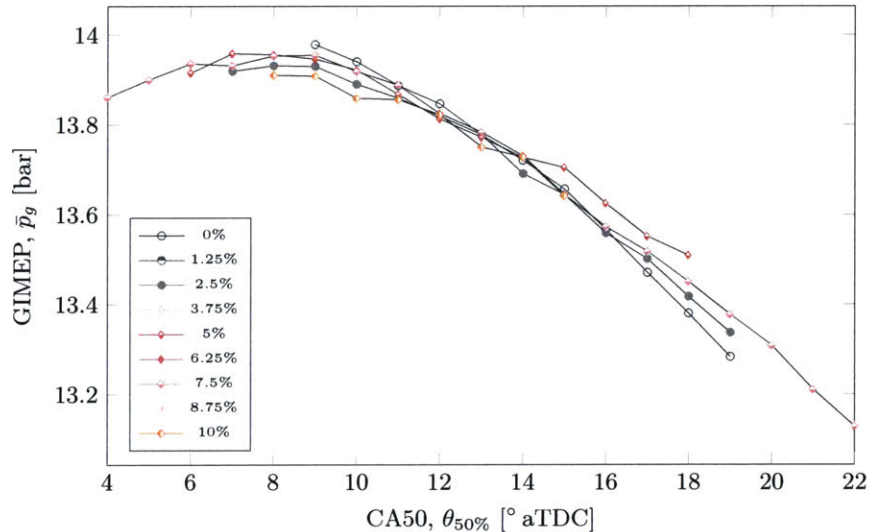


Figure 3-22: The MBT CA50 and overall characteristics of the GIMEP profiles are unchanged from the conditions observed with pre-catalyst EGR.

The burn durations and change in burn duration with increasing EGR mirror the values observed with the pre-catalyst EGR installation, increasing by approximately 2° for every 5% EGR (cf. Figure 3-23). However the spark to 10% burn durations appear to have been reduced across all conditions (cf. Figure 3-24). The reduction in spark to 10% burn durations is 3° to 4° , resulting in a similar knock limited spark timing but substantially advanced knock limited CA50. This behavior is consistent with a charge that is enriched due to scavenging. Cycle simulations performed in GT-Power indicate that altering the exhaust system in this way is likely to increase the amount of unburned airflow through the engine during valve overlap which results in a richer than stoichiometric trapped charge.

With the number of apparent changes in charge conditions due merely to a different installation of the EGR system it is not surprising that the autoignition limits also change. The change is believed

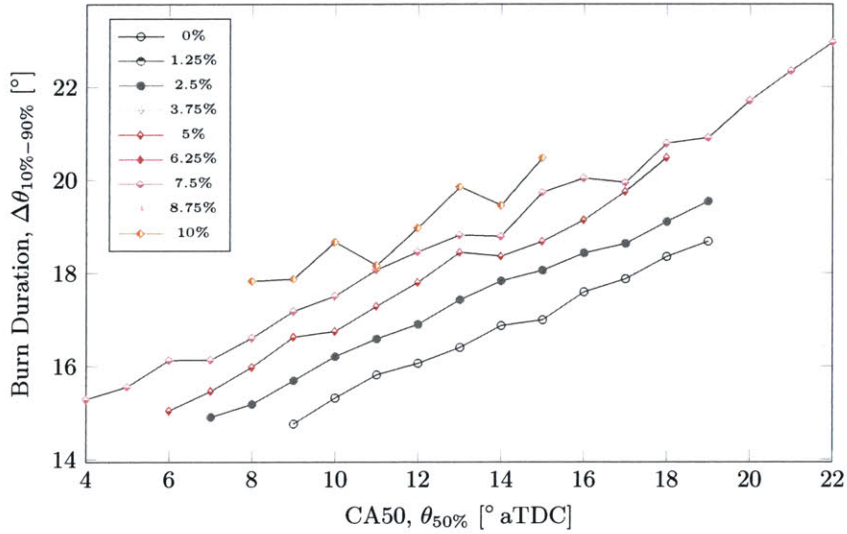


Figure 3-23: Burn durations and their dependence on EGR rate is also very similar to the pre-catalyst EGR conditions, however the data indicates that spark to 10% burn durations are reduced by 3° across all conditions.

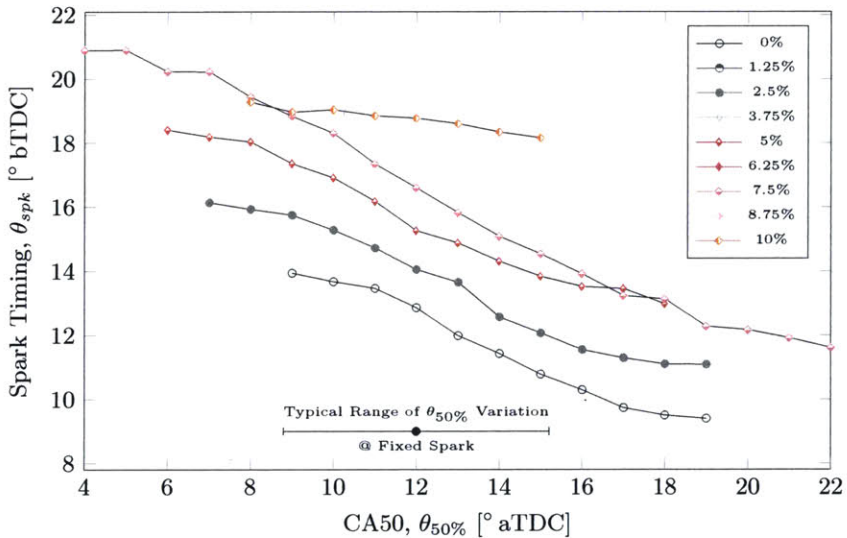


Figure 3-24: The relationship between spark timing and CA50 demonstrates the change that has occurred in the early stages of flame development when the EGR system was changed. The post-catalyst configuration results in shorter flame development periods. This is believed to be caused by an increase in scavenging during valve overlap which tends to enrich the charge.

to be caused by two factors. First, cylinder pressures are reduced due to scavenge flow through the engine resulting in a lower trapped mass of air. And second, because of the lower trapped mass of air and identical fueling the charge is enriched which improves knock tolerance by a mechanism similar to dilution. The net result of both of these changes is to advance the knock limited CA50 for the zero EGR case from 12.7 °aTDC for the pre-catalyst installation to 8.2 °aTDC for the post-catalyst installation. Clearly these changes make it difficult to compare the effects of EGR on knock tolerance however, if the change in the knock limited spark advance and knock limited CA50 are compared one arrives at values that are similar to those observed for the pre-catalyst installation (cf. Figure 3-25).

The change in knock limited CA50 is 2° and the change in knock limited spark advance is 4° at 5% EGR. For the pre-catalyst configuration These changes were on the order of 1° and 3° degrees at 5% EGR but increased to 2° and 4° by 6.25%. This difference may be attributed to smaller changes in the total mass fraction of burned gasses in the charge – consisting of residuals and external EGR – under pre-catalyst conditions due to displacement of residual gas with EGR, which does not appear to occur in the post-catalyst configuration which, under zero EGR conditions, already have a very low residual fraction (under 1% according to cycle simulation). Because the knock limited CA50 of the zero EGR case is closer to the CA50 of MBT gains realized by the improved knock tolerance with the introduction of EGR are modest (cf. Figure 3-26). There is virtually no improvement based on the aggressive CA50 knock limit and an improvement of less than 1% for the conservative CA50 limit.

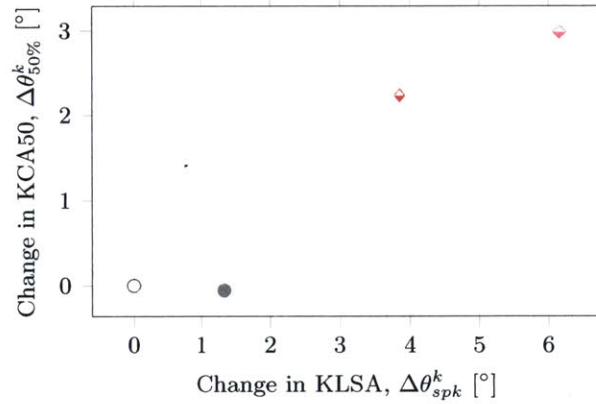


Figure 3-25: Changes in the knock limited spark advance and knock limited CA50 are similar to those observed with pre-catalyst EGR at a slightly higher external EGR rate. This may be due to displacement of residual gasses in the pre-catalyst configuration that does not occur using the post-catalyst installation.

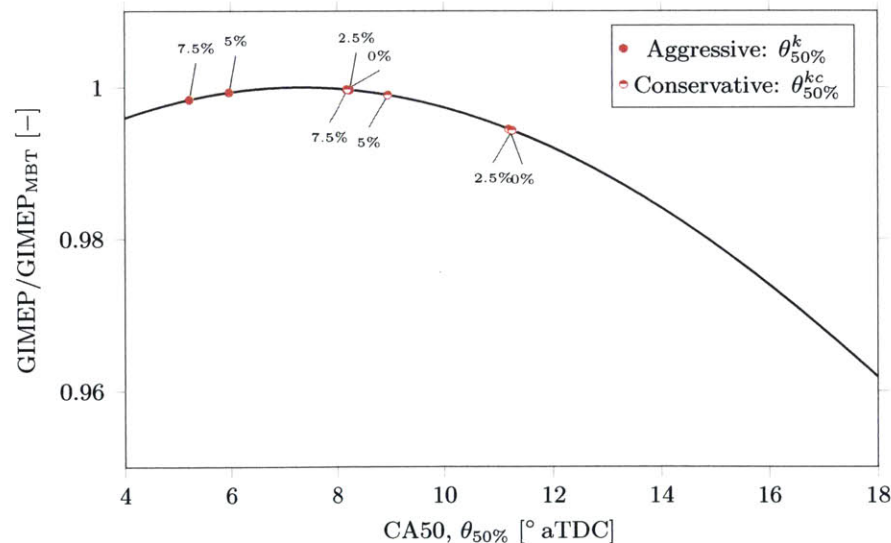


Figure 3-26: The knock limited CA50 with no EGR is close to MBT timing, thus improvements in efficiency due to improvements in autoignition tolerance result in a considerably lower efficiency gain.

Gas Addition Experiments

A series of experiments were performed in which gasses that exist in pre-catalyst EGR were added to an air-fuel mixture independently of any EGR system (cf. Figure 2-6). Bottled H₂, CO and NO were added with the intention of identifying the source of any potential differences in autoignition or combustion behavior. Based on the analysis of pre-catalyst and post-catalyst installations, no concrete differences in autoignition behavior or combustion could be observed thus the focus of this effort was to determine the quantity of these substances that must be introduced in order for measurable changes to occur in engine behavior.

The experiments presented here were performed at 1500 rpm, nominal valve timing and with the EGR system removed. The total fuel energy provided in the form of gasoline and fuel gasses was fixed at an amount equivalent to 120 g min⁻¹ of the Haltermann reference fuel. This implies that as gaseous fuels are used to replace liquid fuel the manifold pressure increases. The NO was given no fuel value and was provided to the engine in the form of 4% NO with a balance of N₂.

The addition of hydrogen is initially met with reductions in burn duration without a substantial change in knock resistance, this causes the knock limited spark timing to be retarded slightly with increasing rates of hydrogen in order to maintain the same combustion phasing (cf. Figure 3-27). When hydrogen makes up 3% of the fuel energy the reduction in spark to 50% burn duration is approximately 1.25°. Beyond 3% hydrogen energy the knock limited CA50 begins to improve, ultimately reaching 5° of advance when 10% of the fuel energy is hydrogen. This improvement in the knock limited CA50 is believed to be due to the reduction in peak unburned gas temperatures caused by increasing the pre-combustion pressures as the fraction of gaseous fuel is increased. This effect is identical to the dilution effect described by Hoepke^[30].

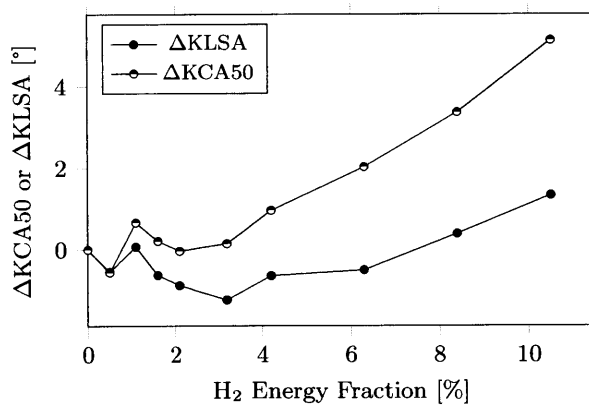


Figure 3-27: The replacement of gasoline with hydrogen fuel in the percentages indicated above each point indicate that the initial effect of hydrogen addition is to decrease the spark to 50% burn duration without substantial changes in the knock limited CA50. Beyond 3% hydrogen by energy the additional hydrogen reduces changes in the unburned gas temperature resulting in improved knock resistance and earlier knock limited CA50 values.

The changes observed with hydrogen addition can be put in perspective with relation to EGR by

observing that combustion inefficiencies are generally below 10% – even under mildly rich conditions – thus if a maximum EGR rate of 30% is possible the recirculated fuel energy will be on the order of 3%, only one quarter of which would generally be hydrogen. This restricts the energy fraction of hydrogen to values under approximately 0.75%. Based on the experimental data the three points obtained with 0%, 0.5% and 1.1% hydrogen energy lie within $\pm 0.25^\circ$ degree of each other with regard to changes in the knock limited spark advance. No claim can be made that such small variations in the knock limit are statistically significant. The change in knock limited CA50 is on the same order and also considered statistically insignificant.

Carbon monoxide generally makes up the remaining three quarters of the chemical energy of the exhaust which means that a maximum of 2.25% of the fuel energy could be recirculated in the form of CO. A similar set of experiments was performed by introducing CO while maintaining the total fuel energy constant. The results indicate that the knock limited CA50 is advanced by approximately 1° up to fuel energy fractions of 4.5% while the knock limited spark advance remains constant. This implies that the spark to 50% burn duration is also shortened by 1° . Further increases in CO do not appreciably alter the knock characteristics, however they continue to reduce spark to 50% burn durations. Based on the maximum expected CO energy of 2.25% it is unlikely that CO plays a dominant role in EGR chemistry. Compared to hydrogen, carbon monoxide produces a more substantial effect in the quantities that are to be expected in EGR.

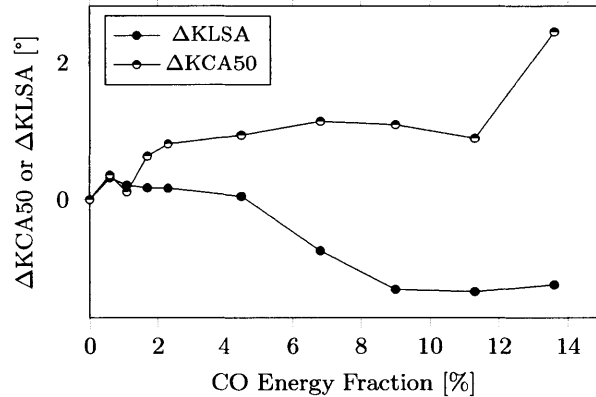


Figure 3-28: The addition of CO initially results in shortened spark to 50% burn durations and a modest improvement in the knock limited combustion phasing (1°). Beyond 4.5% of the fuel energy no additional improvement in the knock limit is realized however the burn durations continue to be reduced. It is unlikely that CO in the fractions present in EGR is capable of altering the gross combustion characteristics.

The final gas examined was nitric oxide. Sources within the literature report that NO is damaging to knock resistance and the experimental data appears to confirm this finding. Even at modest levels in the hundreds of ppm the knock limited CA50 must be retarded by 1° despite the introduction of a diluent (N_2) in conjunction with NO. The formation rate of NO is highly temperature sensitive however 1000 ppm is not uncommon. Using a maximum of 30% EGR one would expect the concentration of NO in the intake charge to be on the order of 250 ppm which may result in

a measurable degradation in the autoignition characteristics of the charge. Luckily with increased amounts of EGR NO formation reactions fall from favor and it is unlikely that high enough levels of NO exist within the exhaust of engines running at modest EGR rates to produce detrimental effects.

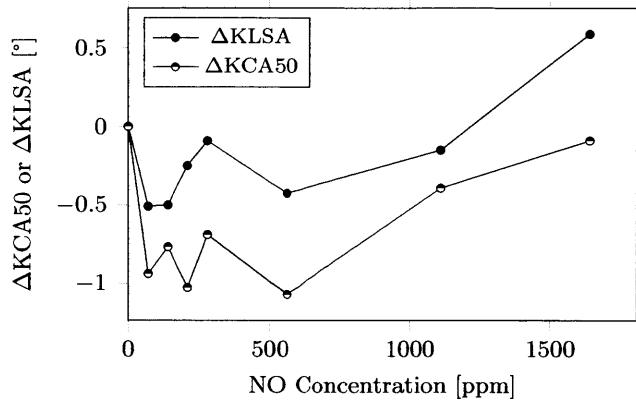


Figure 3-29: Nitric oxide appears to degrade the knock resistance of the air-fuel mixture despite relatively minute concentrations. This effect, although possible, is not likely to occur in practice because the formation rate of NO in engines operating with EGR is low.

Chapter 4

Knock Onset and Intensity Correlation

The autoignition of air-fuel mixtures has been the subject of research for nearly a century, and although much progress has been made in the development of anti-knock fuel additives, a detailed understanding of the chemical reactions that precipitate the autoignition of gasoline has not yet been developed. This difficulty has directed the study of autoignition in engines towards the development of empirical models. The chapter that follows describes a new approach to generating the data required to create a robust Livengood-Wu knock integral correlation that includes the effects of recirculated exhaust gasses and changes to the air-fuel ratio. The results of this correlation are then used to develop a statistical model of the cycle-to-cycle variation in knock intensity.

4.1 Chemical and Empirical Autoignition Models

The primary impediment to the chemical modeling of autoignition is the overwhelming compositional complexity of gasoline, which typically contains hundreds of chemical compounds each capable of numerous reactions. For less complex fuels, such as the two component blend of iso-octane and n-heptane known as PRF, a sequence of reactions has been identified by Semenov that leads to delayed autoignition^[21]. To understand this chain of events it is helpful to refer to experimental data. The two devices most frequently used to study autoignition are the combustion bomb and the RCM (cf. Figure 4-1).

The combustion bomb is the simpler of the two devices and consists of a spherical chamber with a spark electrode gap at its center. A mixture of air and fuel vapor is admitted at an initial pressure and temperature and the spark electrode is energized, causing a flame to propagate radially from the center. The flame compresses the unburned air-fuel mixture (end gas) near the walls and if the

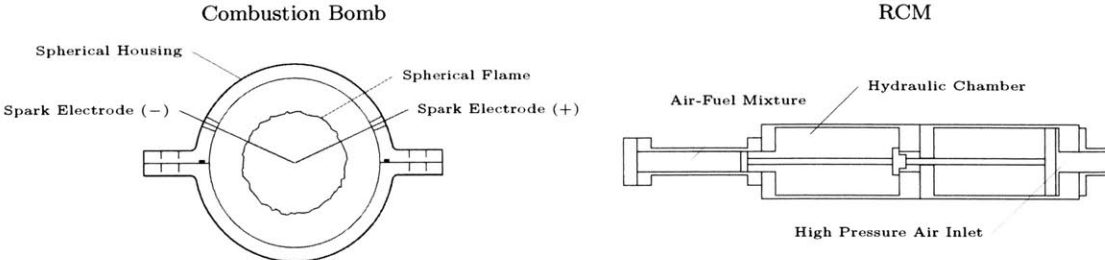


Figure 4-1: Schematic diagram of a combustion bomb (adapted from Keck^[31]) and a rapid compression machine showing their construction and key parts. The combustion bomb is filled with an air-fuel mixture which is ignited by the extended spark plug electrodes. The spherical flame that develops compresses the end gas near the chamber walls which may cause it to autoignite. The RCM is filled with an air-fuel mixture and the hydraulic section is pressurized to hold the piston at the bottom of its stroke. A pneumatic pressure is then applied to a driving piston pre-loading the piston shaft. Once the hydraulic pressure is removed the piston is driven forward at high speed, compressing the air fuel mixture.

temperature and pressure rise to high enough levels the end gas will autoignite before it is consumed by the flame. The RCM functions somewhat differently. Within the cylinder a mixture of air and fuel is isentropically and adiabatically compressed to a fraction of its initial volume. If the pressure and temperature of the charge are high enough the mixture will autoignite. Experiments have shown that under some conditions mixtures of PRF and air that are compressed in an RCM release heat in two distinct stages (cf. Figure 4-2). During the first “cool” stage, which occurs shortly after compression, a small fraction of the thermal energy of the air-fuel mixture is released, causing the temperature to rise approximately 75 K. After a delay of several milliseconds the mixture progresses into “hot” combustion and the remainder of the thermal energy is liberated. The set of reactions that exhibit this characteristic two-stage combustion and long induction times was initially proposed by Semenov^[21] and later refined by researchers at Shell^[53] and Hartwell Research Laboratory^[15]. A brief outline of the proposed mechanism is presented here that summarizes the more detailed work of Cox^[15].

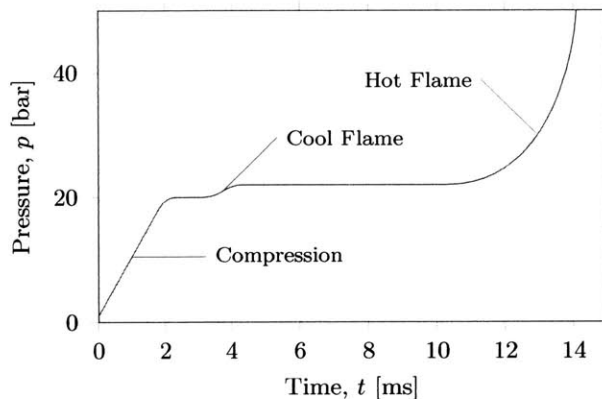


Figure 4-2: Schematic representation of two-stage ignition in a rapid compression machine. The temperature of the mixture may rise by 75 K during the cool flame stage which represents the release of well under 5 % of the total fuel energy.

Model of the Chemical Reactions Leading to Autoignition

1. A reaction is initiated by the interaction of fuel and oxygen. Following initiation, radical species participate in chain propagation and termination reactions which result in the formation of meta-stable intermediate such as an aldehyde (R-CHO) among other compounds.
2. After quenching of the cool flame the mixture enters a state in which the rate of chain termination reactions is greater than the rate of chain branching reactions, this causes the radical concentration to decrease, relaxing to a lower value.
3. The degenerated branching reactions of the intermediate compounds such as (R-CHO) increase the radical concentration which leads to the formation of additional branching agents.
4. When the net radical production factor (β) which is defined as:
$$\beta \equiv \text{rate of radical production} - \text{rate radical destruction},$$
exceeds zero there is a rapid increase in the number of radicals and autoignition occurs.

Cox suggests that fuel and oxygen concentration, pressure, temperature and the composition of the air-fuel mixture all affect the induction period. The fuel and oxygen concentrations enter directly into the computation of the reaction rates of the various steps that precede autoignition. The pressure affects autoignition because it changes these concentrations. Temperature on the other hand alters the reaction rates of each reaction differently, thus the effect of temperature on the aggregate reaction may defy intuition, particularly for fuels in which the cool flame and hot flame reactions are favored in disparate temperature ranges (such as PRF). The composition of the fuel influences the formation of meta-stable intermediates which play a critical role in autoignition chemistry. Due to the complexity and uncertainty involved in the development of a chemical autoignition model, automotive research has focused on the development of empirical models that capture and approximate the behavior of air-fuel mixtures in either rapid compression machines or firing engines.

The Autoignition Integral

The empirical method of correlating in-cylinder conditions with the onset of autoignition proposed by Livengood and Wu^[44] has seen widespread use since its proposal in 1955^[20]. Their method assumes that autoignition occurs rapidly after the concentration of a hypothetical knock precursor – which may be considered a progress variable for autoignition – exceeds a critical value. The knock precursor reaction – which is most likely a complex aggregate reaction – is assumed to be of zero order and thus independent of precursor concentration. This assumption implies that the concentration of knock precursors at time t is given by,

$$\frac{[x]}{[x]_c} = \int_{t_0}^t \frac{1}{\tau(t)} dt, \quad (4.1)$$

where $[x]$ is the precursor concentration, $[x]_c$ is the critical precursor concentration, t_0 is an initial time with a negligibly small precursor concentration and τ is an ignition delay function, which in general depends on the pressure, temperature and composition of the air-fuel mixture. If the critical precursor concentration is assumed to be constant, autoignition will occur at time t_c where

$$1 = \int_{t_0}^{t_c} \frac{1}{\tau(t)} dt. \quad (4.2)$$

When experiments are performed in a rapid compression machine the relevant properties of the charge (pressure, temperature, composition) are constant during the ignition delay. This implies that the value of τ is also constant. Thus by measuring the time between compression and autoignition ($t_c - t_0$) in a RCM the value of τ for a specific constant pressure (\bar{p}), constant temperature (\bar{T}) and composition may be identified as,

$$\tau(\bar{p}, \bar{T}) = t_c - t_0 \quad (\text{RCM}). \quad (4.3)$$

Experiments of this type over a range of pressures and temperatures suggest that the ignition delay function can be approximated by an equation of the form^[44]

$$\tau(p, T) = ap^{-b}e^{c/T}, \quad (4.4)$$

where p is the cylinder pressure, T is the end gas temperature, and a , b and c are empirical constants that depend on the composition of the mixture^[59, 58]. Realistically, expressions of this type only match experimental data well over a limited range of temperatures. If the logarithm of the ignition delay predicted by Eq. 4.4 is plotted against $1/T$ the isobars are linear (cf. Figure 4-3) with a slope that depends only on c as described by

$$\log(\tau) = c \log(e) \frac{1}{T} + \log(a) - b \log(p). \quad (4.5)$$

However, when some fuels (such as PRF) are tested in a RCM at a constant post-compression pressure the temperature dependence appears to be considerably different than this simplified model (cf. Figure 4-4). The distinctive dip in plots of $\log(\tau)$ against $1/T$ is attributed to a *negative temperature coefficient* at these intermediate temperatures. This behavior is present at temperatures where activity due to a low temperature reaction mechanism decreases more rapidly than activity from a high temperature reaction mechanism increases. Although not all fuels exhibit a clear negative temperature coefficient region it is sensible to recognize that the proposed ignition delay expression represents an oversimplification of the behavior of real fuels and is thus predisposed to errors when applied over a wide temperature range.

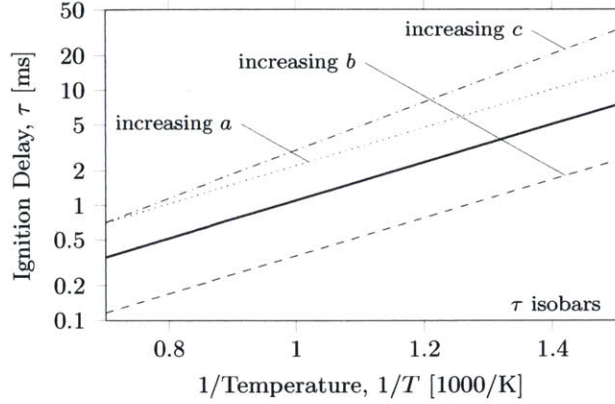


Figure 4-3: The ignition delay isobars that are described by Eq. 4.4 are shifted upward by increasing a , downward by increasing b and increasing c increases the slope of the line while maintaining the same y -intercept.

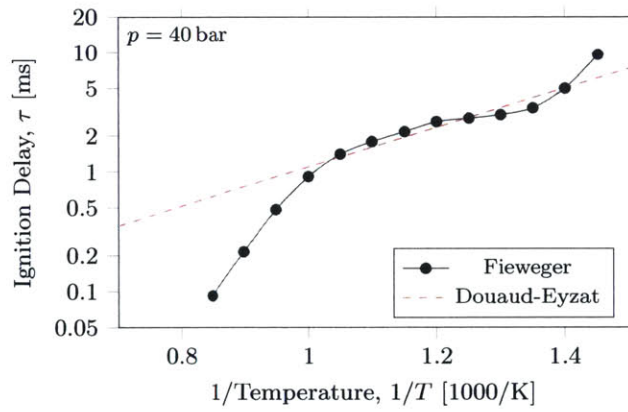


Figure 4-4: Ignition delay data from Fieweger^[22] for PRF 90. The exponential temperature dependence in τ can only accurately model a portion of the ignition delay characteristics of a real fuel.

The Role of Uncertainty in the Prediction of Autoignition

At this point, having accepted the inherent inaccuracy of a simplified ignition delay formulation, it is instructive to consider what effects differences between the simplified ignition delay function and the true behavior of fuels may have on the accuracy of autoignition prediction in engines. In a rapid compression machine the temperature, pressure and composition of the charge are close to constant during the induction period. This implies that the ignition delay also assumes a near constant value. Factoring a constant ignition delay ($\tau(t) = \bar{\tau}$) out of the integral in Eq. 4.2 and evaluating the integral yields

$$1 = \frac{t_c - t_0}{\bar{\tau}}. \quad (4.6)$$

Which can be rearranged to recover the definition of the ignition delay

$$\bar{\tau} = t_c - t_0. \quad (4.7)$$

A sensitivity analysis on this expression is straightforward and indicates that uncertainty in the measurement (or identification) of t_c and t_0 are reflected directly in the ignition delay. Mathematically the sensitivity of $\bar{\tau}$ is given by,

$$\Delta\bar{\tau} \approx \Delta t_c - \Delta t_0. \quad (4.8)$$

Or if the intent is to predict the time at knock based on past observations,

$$\Delta t_c \approx \Delta\bar{\tau} + \Delta t_0. \quad (4.9)$$

This situation is tractable and the implications of inaccuracy are apparent even in the absence of any formal analysis. However, the situation that occurs in a firing engine or a combustion bomb is considerably more complex. In these devices the pressure and temperature of the end gas is changing rapidly during the induction period. This causes the value of τ is varying as a function of time from a very large value (practically infinite at standard atmospheric pressure and temperature) to one many orders of magnitude smaller. Under such conditions it is worthwhile to consider the sensitivity of the observed time of autoignition (t_c) to uncertainty in the ignition delay ($\Delta\tau$). The primary contribution to uncertainty in the ignition delay is made by the simplification of complex fuel behavior to an equation with the form of Eq. 4.4. Thus studying the effect of errors in τ on t_c provides guidance on how Eq. 4.4 can be fit to experimental ignition delay data to maximize the accuracy of autoignition prediction.

Suppose, in the interest of simplicity, that ignition delays measured on a rapid compression machine are completely accurate and are known for all combinations of temperature and pressure. One method of determining the expected time of autoignition (t_c) would begin by measuring the pressure and temperature in the end gas of a firing engine over time. At each instant in time the ignition delay for the current pressure and temperature could then be identified from the RCM measurements. This matching process would allow the time history of τ to be constructed and the value of the autoignition integral (I) to be determined where,

$$I(t) = \int_{t_0}^t \frac{1}{\tau(t)} dt. \quad (4.10)$$

When the condition $I(t_c) = 1$ is met the autoignition integral predicts that autoignition will occur. This process can be visualized by plotting the reciprocal of the ignition delay as a function of time and identifying the time at which the area under the curve equals one (cf. Figure 4-5).

Now suppose that instead of measured ignition delay data an equation with the form of Eq. 4.4 is used. As discussed earlier equations of this type do not reproduce the ignition delay characteristics of real fuels and thus some difference ($\Delta\tau$) is anticipated between the ignition delay measured on an ideal RCM and the simplified model. This difference in ignition delay will in turn result in a

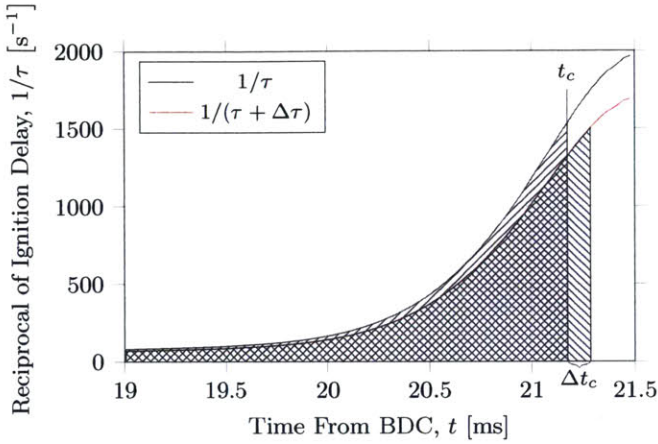


Figure 4-5: The reciprocal of the ignition delay is accumulated until the area under the curve equals unity. Errors accumulated up to t_c must be balanced by an additional area between t_c and $t_c + \Delta t_c$.

difference in the time at which autoignition is predicted (Δt_c). If the same autoignition integral procedure is pursued it can be shown that the predicted time of autoignition becomes $t_c + \Delta t_c$ where,

$$1 = \int_{t_0}^{t_c + \Delta t_c} \frac{1}{\tau(t) + \Delta\tau(t)} dt. \quad (4.11)$$

To identify the scaling characteristics of Δt_c one may separate the integral in Eq. 4.11 into the intervals (t_0, t_c) and $(t_c, t_c + \Delta t_c)$ which can be rearranged to form,

$$1 - \int_{t_0}^{t_c} \frac{1}{\tau + \Delta\tau} dt = \int_{t_c}^{t_c + \Delta t_c} \frac{1}{\tau + \Delta\tau} dt. \quad (4.12)$$

Linearizing the right hand side, which occupies the small time interval $(t_c, t_c + \Delta t_c)$, one arrives at the expression

$$1 - \int_{t_0}^{t_c} \frac{1}{\tau + \Delta\tau} dt \approx \frac{1}{\tau + \Delta\tau} \Big|_{t_c} \Delta t_c + \frac{\partial \left(\frac{1}{\tau + \Delta\tau} \right)}{\partial t} \Big|_{t_c} (\Delta t_c)^2. \quad (4.13)$$

Neglecting the second order Δt_c term identifies the approximate scaling relationship

$$\Delta t_c \approx \frac{1 - \int_{t_0}^{t_c} \frac{1}{\tau + \Delta\tau} dt}{\frac{1}{\tau + \Delta\tau} \Big|_{t_c}}. \quad (4.14)$$

Or more simply,

$$\Delta t_c \approx (\tau + \Delta\tau)|_{t_c} \left(1 - \int_{t_0}^{t_c} \frac{1}{\tau + \Delta\tau} dt \right). \quad (4.15)$$

The first term of this expression is the modeled ignition delay at autoignition and the second term is a measure of the relative error between the actual and modeled autoignition integrals over the

interval (t_0, t_c) . Replacing the one in Eq. 4.15 with Eq. 4.10 evaluated at t_c yields,

$$\Delta t_c \approx (\tau + \Delta\tau)|_{t_c} \left(\int_{t_0}^{t_c} \frac{1}{\tau} - \frac{1}{\tau + \Delta\tau} dt \right) \quad (4.16)$$

which is identical to,

$$\Delta t_c \approx (\tau + \Delta\tau)|_{t_c} \left(\int_{t_0}^{t_c} \frac{\Delta\tau}{\tau} \frac{1}{\tau + \Delta\tau} dt \right). \quad (4.17)$$

Formulating Δt_c in this way provides substantial insight into the factors that contribute to errors in the predicted time of autoignition. The first parenthetical term in Eq. 4.17 is the modeled value of the ignition delay at autoignition. This term is reduced when ignition delays are small which causes the rate of change of the autoignition integral to be large. The size of this term is dominated by τ which depends primarily to the operating pressures and temperatures at autoignition, making it an impractical method of controlling uncertainty in the predicted autoignition time. However, the second term presents just such an opportunity. The most effective method of minimizing the integral that makes up the second term is to reduce the relative uncertainty ($\Delta\tau/\tau$) when τ is small. In other words a high level of uncertainty when the ignition delay is small is significantly more damaging to predicting the autoignition time than the same level of uncertainty when the ignition delay is large. This can be observed graphically by plotting contours on which the integrand of this term is constant as a function of τ and $\Delta\tau$ (cf. Figure 4-6).

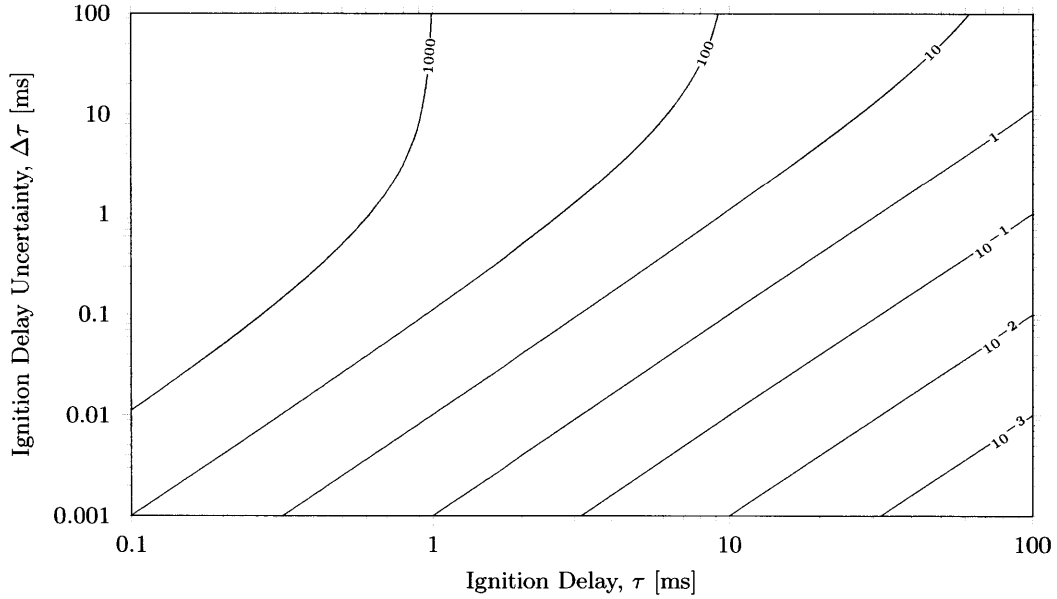


Figure 4-6: Contour plot of $(\Delta\tau/\tau)(1/(\tau+\Delta\tau))$ which is the controllable factor that influences uncertainty in ignition delay prediction (Δt_c). The upper left portion of the map represents the most damaging situation per unit integration time and the lower right is the least damaging. Contours are spaced logarithmically with units of ms^{-1} .

In the previous analysis an integral was identified that is proportional to the error induced in the

predicted autoignition time. These errors were caused by errors in the ignition delay. Defining U as

$$U \equiv \int_{t_0}^{t_c} \frac{\Delta\tau}{\tau} \frac{1}{\tau + \Delta\tau} dt, \quad (4.18)$$

the task of reducing the amount of error that propagates from $\Delta\tau$ to Δt_c can be restated as determining $\min(U)$. At this point it is informative to specify an approximate time history of the ignition delay and examine the behavior of U in response to changes in $\Delta\tau$. In the analysis that follows experimental data obtained with the LNF engine is used to aid in the description of uncertainty concepts. The quantitative values developed by this procedure are intended to provide some insight into the relative size of various parameters and should not be taken as representative of the autoignition processes in general. With this in mind experimental measurements indicate that under a specific set of operating conditions the time history of the ignition delay is approximately,

$$\tau(t) \approx 10^9 e^{-t} \quad [\text{ms}], \quad (4.19)$$

where both t and τ are measured in ms. If a simple functional relationship between τ and $\Delta\tau$ is assumed, for example $\Delta\tau = c\tau$, then the value of c can be determined that results in a particular value of U , thereby establishing a relationship between $\Delta\tau$ and τ that causes a certain level of uncertainty in Δt_c . Pursuing this analysis for $U = 0.01$ and several forms of the $\Delta\tau$ function (cf. Table 4.1) allows plots of $\Delta\tau$ to be constructed that result in the same value of Δt_c (cf. Figure 4-7). It is clear from these charts that a modest improvement in the accuracy at the lowest values of the ignition delay is rewarded with considerable headroom for inaccuracy at larger ignition delay values. For example, if the error is reduced from a constant value of 0.02 ms to a value of 0.01 ms for ignition delays from 1 ms to 2 ms the error can be increased to 0.1 ms at $\tau = 10$ ms and near 1 ms at $\tau = 100$ ms without changing the error in t_c . Superimposing these functions onto the contour plot generated in the previous paragraph shows that the integrand of U grows very rapidly as τ becomes small if $\Delta\tau$ is constant, less quickly if $\Delta\tau \propto \tau$ and is nearly constant if $\Delta\tau \propto \tau^2$. This normalization of the contributions made to Δt_c over all values of τ suggests that if experimental ignition delay data is to be used to predict autoignition in engines special attention must be given to the conditions under which the smallest ignition delays are observed.

Uncertainty Functions	
Constant	$\Delta\tau_1(\tau) = c_1$
Proportional	$\Delta\tau_2(\tau) = c_2\tau$
Quadratic	$\Delta\tau_3(\tau) = c_3\tau^2$

Table 4.1: Uncertainty types as functions of τ .

Returning to the difficulty posed by experimental data that does not agree with the simplified model of the ignition delay it is now clear that the region that should be weighted most heavily during the identification of the unknown constants in Eq. 4.4 is governed by the highest temperatures and

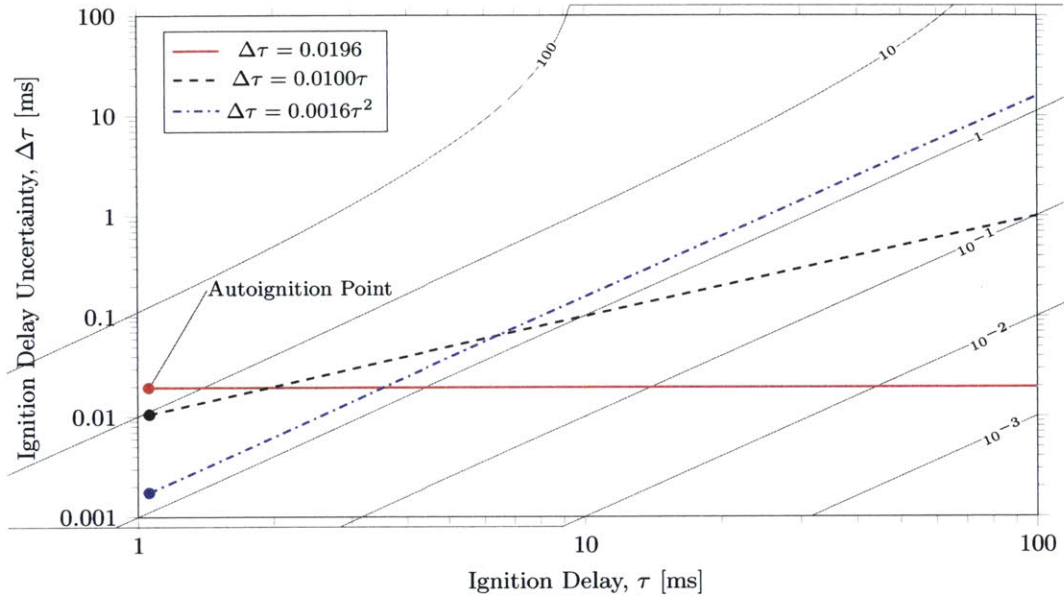


Figure 4-7: Three functional relationships between τ and $\Delta\tau$ are explored that result in identical values of U from Eq. 4.18 and therefore are expected to result in similar errors in autoignition prediction. A slight improvement in accuracy near the autoignition conditions allows considerably more latitude for errors at higher ignition delays. A comparison of these functions with contours over which the integrand of U is constant indicate that when $\Delta\tau \propto \tau^2$ the integrand of U is nearly independent of τ and thus errors are accumulated uniformly over time.

pressures generally reached before autoignition. These temperatures and pressures, and the ignition delays they produce, depend broadly on the characteristics of the engine and the regime in which it is operated. Surrounding this ignition delay *target region* the weighting can be reduced in proportion to $(\tau - \tau_{target})^{-2}$. Weighting the data in this way will provide good performance for autoignition prediction by ensuring that contributions to prediction error are appropriately balanced between high and low ignition delay values. To demonstrate this technique a line was fit to the semi-log plot of ignition delay data measured by Fieweger^[22] for PRF 90 at 40 bar (cf. Figure 4-8). An ignition delay of 2.5 ms was selected as a representative ignition delay at autoignition based on measurements in a CFR engine^[17]. The weights used to determine the best fit line were thus specified as $(\tau - 2.5 \text{ ms})^{-2}$. Using these weights resulted in the identification of a line which, when converted to the form of Eq. 4.4, has the equation,

$$\tau(T) = 1.9 \times 10^{-5} e^{\frac{4100}{T}} \quad [\text{s}]. \quad (4.20)$$

This can be compared to the well known ignition delay expression developed by Douaud and Eyzat^[17] for PRF blends in CFR engines,

$$\tau_{DE}(p, T) = 0.01869 \left(\frac{ON}{100} \right)^{3.4017} p^{-1.7} e^{\frac{3800}{T}} \quad [\text{s}], \quad (4.21)$$

where ON is a volume fraction of isoctane between 80 and 100, p is the pressure in kgf cm^{-2} and T is the temperature in K. Plugging in $ON = 90$ and $p = 40 \text{ bar} \times 1.020 \frac{\text{kgf cm}^{-2}}{\text{bar}}$ reduces this equation to,

$$\tau_{DE}(40.8, T) \approx 2.4 \times 10^{-5} e^{\frac{3800}{T}} \quad [\text{s}], \quad (4.22)$$

which compares favorably with the expression developed from the weighted linear regression above despite the regression being based on somewhat sparse experimental data. The results of the error propagation analysis performed in this section can be summarized succinctly: to improve the accuracy of autoignition prediction in engines it is critical to ensure that the lowest ignition delay values generally encountered are known with the highest accuracy.

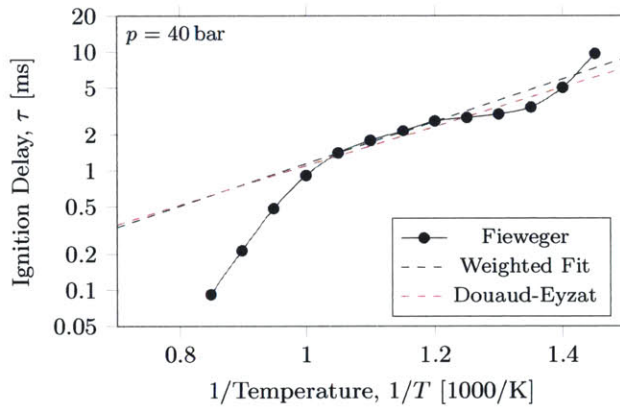


Figure 4-8: A fit to ignition delay data observed in shock tubes experimentally by Fieweger^[22] was computed by weighting the data according to $(\tau - 2.5 \text{ ms})^{-2}$. The center of the weighting function is dictated by the operating characteristics of a particular apparatus, with ignition delays of 2 ms to 3 ms being common near the time of autoignition in CFR engines^[17]. For an engine that operates at higher temperatures and pressures the weighting target would be shifted to the left resulting in a higher slope.

Direct Measurement and Application of the Autoignition Integral

As the analysis of error propagation and the form of Eq. 4.2 make clear, the application of the autoignition integral to a firing engine requires precise time-resolved knowledge of end gas temperature and pressure as well as the function $\tau(p, T)$ which depends on the fuel and end gas composition. In order for a direct approach – that is directly measuring $p(t)$, $T(t)$ and $\tau(p, T)$ – to be a practical method of predicting the time of autoignition it must be possible to reduce uncertainty in these measurements to levels that do not significantly alter the evaluation of the autoignition integral.

The piezoelectric cylinder pressure transducer is perhaps the most widely installed and used sensor in engine testing and calibration. Due to this widespread use sensor accuracy has been rigorously studied and steadily improved^[40]. Modern sensors such as the Kistler 6125 series sensor used in the LNF are linear to within 0.4 bar over the 100 bar calibrated range and the installation of a flame arrestor reduces the effects of short term thermal drift considerably^[56]. If the ignition delay

has the form of Eq. 4.4 then the sensitivity of τ to errors in p is approximately,

$$\begin{aligned}
\Delta\tau_p &\approx \frac{\partial\tau}{\partial p}\Delta p \\
&\approx ae^{\frac{c}{T}}(-b)p^{-b-1}\Delta p \\
&\approx ap^{-b}e^{\frac{c}{T}}(-b)p^{-1}\Delta p \\
&\approx -b\tau\frac{\Delta p}{p}.
\end{aligned} \tag{4.23}$$

If b is taken as 1.7 from Eq. 4.21, τ is set to 2.5 ms and $\Delta p/p$ is half a percent, or 0.005 the resulting error in τ is $\Delta\tau_p = -0.021$ ms. This level of uncertainty in τ is acceptable at just under one percent. It is interesting to note that the uncertainty induced by pressure measurement errors is proportional to τ which from the previous analysis is better than having an error that is independent of τ as may be caused by pegging errors.

Measuring the temperature of the end gas in a firing engine is considerably more difficult than measuring cylinder pressure. The traditional method relies upon precise measurement of the speed of sound. This technique often necessitates modification of the cylinder block or cylinder head in order to accommodate the requisite actuators and transducers. This type of modification has widespread effects on engine performance and heat transfer in the area of the transducer may cause the measured temperature to differ somewhat from the temperature in the autoignition region. Generally accuracy not much better than ± 30 K is to be expected^[44]. An alternative method based on laser interferometry provides improved performance in the range of ± 15 K, however it too requires extensive modification of the cylinder head or block^[27, 35]. An issue that affects both of these systems is that measurements are localized to a specific region which may or may not be the region in which autoignition is most likely to occur. This spatial uncertainty in the end gas temperature may be similar in magnitude to the measurement uncertainty^[19]. If an error propagation analysis is performed for T using the ignition delay form of Eq. 4.4 one finds that

$$\begin{aligned}
\Delta\tau_T &\approx \frac{\partial\tau}{\partial T}\Delta T \\
&\approx ap^{-b}e^{\frac{c}{T}}(-c)T^{-2}\Delta T \\
&\approx -\tau\frac{c}{T}\frac{\Delta T}{T}.
\end{aligned} \tag{4.24}$$

Using the value $c = 3800$ from Eq. 4.21, a representative end gas temperature of 850 K, a temperature measurement uncertainty of 30 K and an ignition delay of 2.5 ms results in $\Delta\tau_T = -0.395$ ms. This is an order of magnitude larger than the error induced by the pressure uncertainty and equates to a fifteen percent error in τ .

The final component of the direct approach is determining the functional relationship between cylinder pressure, end gas temperature and the ignition delay. This often requires a completely

separate apparatus such as a RCM, combustion bomb or shock tube. If these facilities are available the function can be determined by performing a series of experiments at the air-fuel ratio and residual fraction expected to exist in the end gas of the engine. However, having identified the importance of accurate measurement at low ignition delay values the use of both the RCM and combustion bomb present practical challenges. The design of most RCMs is such that compressing the end gas occurs in a timespan on the order of 1 ms to 2 ms which is coincides with the ignition delays of interest. On the other hand the combustion bomb presents the same instrumentation, accuracy and repeatability challenges encountered with engines. Experiments performed in shock tubes^[22, 28], in which an air-fuel mixture is compressed by a shock wave, present the most pragmatic method of directly measuring ignition delays in the range of 1 ms to 3 ms. With repeated tests ignition delay measurement accuracy on the order of 0.01 ms is conceivable, however the slow cycle times and relatively intricate operation of a shock tube limits the amount of data that could be realistically aggregated.

The results of shock tube or RCM experiments are often visualized by plotting the logarithm of τ isobars against $1/T$ (cf. Figure 4-8). These plots, particularly when they contain several isobars, are convenient for analyzing the ignition delay characteristics of the air-fuel mixture. However, plotting the data in this way tends to obscure the characteristics of the ignition delay that are relevant to predicting autoignition in engines. This is because the end gas is nearly adiabatic and isentropic and thus crosses many isobars during compression and combustion. If the end gas is modeled as an isentropic and adiabatic compression of an ideal gas the pressure and temperature are related by

$$p = p_i \left(\frac{T}{T_i} \right)^{\frac{\gamma}{\gamma-1}} \quad (4.25)$$

where p_i and T_i are initial values of the pressure and temperature and γ is the ratio of specific heats. If this expression is substituted into the ignition delay model of Eq. 4.4 one may write

$$\begin{aligned} \tau &= a \left(p_i \left(\frac{T}{T_i} \right)^{\frac{\gamma}{\gamma-1}} \right)^{-b} e^{\frac{c}{T}} \\ &= a \left(p_i T_i^{\frac{-\gamma}{\gamma-1}} \right)^{-b} \left(\frac{1}{T} \right)^{\frac{b\gamma}{\gamma-1}} e^{\frac{c}{T}} \\ &= a' \left(\frac{1}{T} \right)^{b'} e^{\frac{c}{T}}, \end{aligned} \quad (4.26)$$

where

$$a' = a \left(\frac{p_i^{\gamma-1}}{T_i^\gamma} \right)^{\frac{-b}{\gamma-1}} \quad (4.27)$$

and

$$b' = \frac{b\gamma}{\gamma - 1}. \quad (4.28)$$

Taking the logarithm of both sides of this new expression for τ yields,

$$\log(\tau) = \log(a') + b' \log\left(\frac{1}{T}\right) + c \log(e) \left(\frac{1}{T}\right), \quad (4.29)$$

which when linearized about a temperature T_L is approximately,

$$\log(\tau) \approx \log(a') + b' \log\left(\frac{1}{T_L}\right) + \left(\frac{b'T_L}{\ln(10)} + c \log(e)\right) \left(\frac{1}{T}\right). \quad (4.30)$$

Comparing the temperature dependence of this equation to the expression for an isobar derived in Eq. 4.5 one observes that the slope has been incremented by the amount $b'T_L / \ln(10)$ which is positive. Thus if experimental data of ignition delay and temperature is restructured to present curves of constant entropy instead of constant pressure the slopes of these curves will be increased. This causes the negative temperature coefficient region to appear less pronounced. It is these isentropic curves that must be matched well by an ignition delay model that is intended to predict autoignition in engines not the isobaric contours.

This analysis of the direct approach highlights several difficulties, some of which can be addressed by improved equipment and others that are difficult to circumvent. First, in order for the direct approach to be reliable the accuracy of end gas temperature measurement is the area most in need of improvement. To reach the same level of uncertainty induced by the pressure transducer measured temperatures must be accurate to within $\pm 1\text{ K}$ at 850 K , which is technically challenging. Another sizable challenge of a completely different type is presented by the aggregation of the ignition delay data necessary to apply the direct approach. The ignition delay is a nonlinear function of pressure, temperature and composition and thus this three dimensional space must be mapped with a high level of accuracy to be of practical use. The long cycle times for experiments using shock tubes sets realistic limits on the degree of resolution that can be achieved in each of these three dimensions. The difficulty of circumventing these issues was the motivation for seeking an alternative method of identifying the ignition delay that was well suited for use with the autoignition integral.

4.2 Computational Formulation of the Knock Integral and Ignition Delay

The direct measurement of cylinder pressure, temperature, composition and ignition delay presents many practical challenges and is often beyond the capabilities of an individual test apparatus or facility. Instead, a method of inferring several of these values from more readily obtained measurements is preferable. The cylinder pressure transducer is perhaps the most frequently used measurement in engine development and testing, which makes its installation in experimental engines almost uni-

versal. As mentioned in the discussion of the direct approach, the accuracy of modern transducers is quite high, however care must be exercised in their installation to minimize the effects of short term thermal drift due to the arrival of the flame at the transducer face. The installation of flame arrestors and proper transducer selection and calibration techniques greatly reduce the levels of spurious readings generated by thermal stresses^[49]. While considering the accuracy of the pressure transducer it is also important to recognize that the measured pressure is the pressure at a distinct location, generally near the center of the cylinder (cf. Figure 4-9). In the presence of shocks, which may occur during autoignition, the pressure at remote points may differ substantially from the indicated value. In comparison the facilities for measuring end gas temperature and composition are complex, expensive and as a result uncommon. For this reason it is desirable to attempt to infer these values instead of measure them directly.

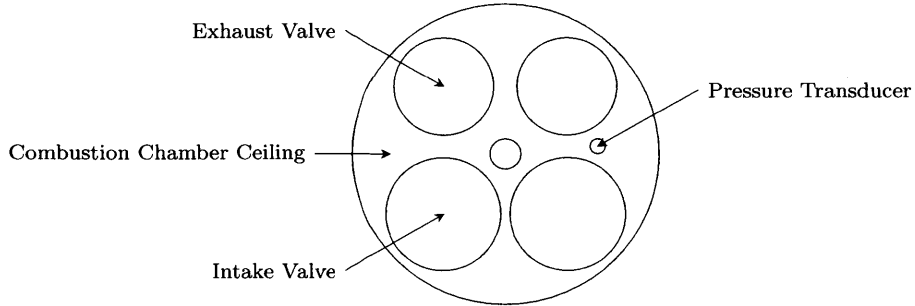


Figure 4-9: The cylinder pressure transducer is located in the cylinder head between the intake and exhaust valves.

Many methods may be used to infer the contents of the cylinder when the intake valve is closed and the method employed depends somewhat on the configuration of the experimental apparatus and available sensing systems. The availability of exhaust air-fuel ratio and external EGR rate measurements leaves the mass fraction of residual burned gasses (w_r) as the largest unknown element of the charge composition. For the present research a calibrated engine model (Gamma Technologies GT-Suite) was provided with steady state experimental data and used to estimate the mass fraction of the residual gasses. The residuals were assumed to possess the same composition as the exhaust, which is an assumption that may underestimate their hydrocarbon content. Once the composition of the charge and the pressure history are known a reasonable estimate of the end gas temperature – in particular the adiabatic core of the end gas – is obtained by assuming that the end gas is compressed isentropically and adiabatically by a combination of the piston motion and the expansion of burning gasses. The specific heat ratio (γ) used in this computation may be computed based the tabulated properties of the charge constituents. In order to apply this adiabatic and isentropic compression model an initial temperature must be known. A reasonable temperature to select is the mean temperature of the charge at intake valve closing (T_{IVC}) which may also be extracted from the calibrated engine model. At the conclusion of this procedure the cylinder pressure history ($p(t)$) has been measured directly and estimates have been made of the end gas temperature history ($T(t)$) and

composition. If the ignition delay function $\tau(p, T)$ is known for the end gas composition in question then the autoignition integral may be evaluated. Since this generally not the case experimental data must be used to determine the ignition delay function.

Identifying the ignition delay function using a shock tube or rapid compression machine is a time-consuming and somewhat limited endeavor. Test durations on the order of minutes are common for a single data point and the ability of these devices to replicate changes in residual fraction are limited. As the subject of the present research is the exploration of combinations of air-fuel ratio and EGR rate on autoignition the test matrix for a shock tube or RCM based determination of the ignition delay function is prohibitively large, particularly because these devices require several experiments at different pressures and temperatures to generate enough data to describe the behavior of a single charge composition. To address these experimental issues a new method of identifying the ignition delay function was developed using data collected in a firing engine. The basis of this approach is to use knowledge of the end gas state and observations of autoignition to infer the functional relationship between the end gas state and the ignition delay. This process has been named (somewhat unimaginatively) the inferred ignition delay (IID) method. To state the approach somewhat differently the ignition delay arguments, principally cylinder pressure (p) and end gas temperature (T), are measured or estimated and observations of the onset time of autoignition t_c are made. This leaves the ignition delay function as the only unknown in the autoignition integral

$$\int_{t_0}^{t_c} \frac{1}{\tau(p, T)} dt = 1. \quad (4.31)$$

Using autoignition observations under many different operating conditions a function $\tau(p, T)$ can be identified that minimizes the error between the observed and modeled time of autoignition. A critical feature of this approach is that it implicitly assumes the Livengood-Wu method of autoignition correlation is valid.

Selecting a Functional Form of the Ignition Delay

Several forms of $\tau(p, T)$ have been proposed in the literature, most of which can be written as either,

$$\tau_1(p, T) = a_1 p^{-b_1} e^{\frac{c_1}{T}} \quad (4.32)$$

or

$$\tau_2(p, T) = a_2 \left(\frac{p}{T} \right)^{-b_2} e^{\frac{c_2}{T}}, \quad (4.33)$$

where a_n , b_n and c_n are empirical constants for a specific charge composition. As discussed in the previous section neither of these equations possess sufficient complexity to describe the behavior of real fuels, instead they are applied as convenient approximations that are accurate over a limited

range of temperatures and pressures. Of the two common forms the latter was selected for this work based on the following interpretation of the pressure to temperature ratio using the ideal gas law:

$$pV = nRT \Rightarrow \frac{p}{T} = \frac{n}{V}R. \quad (4.34)$$

This implies that the pressure to temperature ratio is proportional to concentration. As concentration is more fundamentally relevant to the rate of chemical reactions this selection of correlating parameter was preferred over the correlation of pressure alone. Furthermore it can be shown that if the relationship between temperature and pressure is that of an adiabatic and isentropic process,

$$\begin{aligned} \frac{p}{T} &= \frac{p}{T_i} \left(\frac{p}{p_i} \right)^{\frac{1-\gamma}{\gamma}} \\ &= \frac{p^{\frac{1}{\gamma}-1+1}}{T_i p_i^{\frac{1}{\gamma}-1}} \\ &= p^{\frac{1}{\gamma}} \left(\frac{p_i^{\gamma-1}}{T_i^\gamma} \right)^{\frac{1}{\gamma}}, \end{aligned} \quad (4.35)$$

where p_i and T_i are an initial pressure and temperature respectively. This can be rearranged to arrive at,

$$\left(\frac{p}{T} \right)^\gamma = p \left(\frac{p_i^{\gamma-1}}{T_i^\gamma} \right). \quad (4.36)$$

Because the parenthetical term on the right of this expression is constant for all pressures and temperatures along an adiabatic and isentropic compression the two mathematical forms of the ignition delay have similar pressure and temperature dependence. Solving for the parameters of Eq. 4.32 in terms of the parameters of Eq. 4.33 yields,

$$a_1 = a_2 \left(\frac{p_i^{\gamma-1}}{T_i^\gamma} \right)^{\frac{-b_2}{\gamma}} \quad (4.37)$$

$$b_1 = \frac{b_2}{\gamma} \quad (4.38)$$

$$c_1 = c_2 \quad (4.39)$$

Thus the only differences between these two functional forms arises when changes are made to the level of throttling or turbocharging and intercooling. Such changes to the operating conditions alter the entropy of the charge prior to intake valve closing.

To apply Eq. 4.33 to a firing engine an additional term must be included to account for changes in burned gas fraction due to residual gas and exhaust gas recirculation. The residual gasses, which are assumed to be compositionally identical to exhaust gas, increase the temperature of the charge

and act as a diluent. It is possible that such a change could alter the pre-exponential constant, the concentration term or both. As such a general dilution term $(1 - w_d)^{-d}$ was added to the ignition delay function to arrive at,

$$\tau(p, T, w_d) = a(1 - w_d)^{-d} \left(\frac{p}{T}\right)^{-b} e^{\frac{c}{T}}. \quad (4.40)$$

This equation has four unknowns a , b , c and d for a specific fuel under stoichiometric conditions, and includes the effects of dilution with burned gasses in the form of either residuals or recirculated exhaust gasses via the diluent mass fraction w_d . The effect of increasing w_d is to shift the ignition delays upward (to higher ignition delays) while maintaining the same temperature and p/T dependence. The diluent mass fraction is used for convenience (over the diluent mole fraction) which is a substitution that is justified when the ratio of the diluent to charge molecular weights (MW_d/MW_{total}) is nearly independent of the dilution rate, which is generally the case for dilution by EGR or residuals. Based on the definitions of EGR rate (w_{egr}) and residual fraction (w_r) the amount of burned gas in the charge during stoichiometric operation is,

$$w_d = w_r + w_{egr}, \quad (\lambda = 1). \quad (4.41)$$

Detecting the Time of Autoignition Inception

Having selected a form of the ignition delay expression the next and final prerequisite to applying the inferred ignition delay (IID) approach is to establish a method of determining the time of knock from experimental data. Based on the formulation of the IID method is clear that the accuracy of the ignition delay function relies heavily on accurate observation of the time at which knock occurs within the engine. This requirement presents some difficulty because autoignition is an accelerating chemical reaction and as such requires a finite and somewhat variable time to develop. Measurement of knock onset in a firing engine is further complicated because isolated pockets of end gas tend to ignite independently at different times^[45] and thus the pressure rise observed at the transducer depends on the location and mass of each autoignition region. Estimates of the time required for pressure waves to propagate to a centrally located cylinder pressure transducer from the periphery of the cylinder can be obtained using representative pressures, temperatures and geometry:

$$\Delta t_p = \frac{r_{cyl}}{c} \approx \frac{43 \text{ mm}}{1000 \text{ m s}^{-1}} \approx 43 \text{ } \mu\text{s}, \quad (4.42)$$

where r_{cyl} is the cylinder radius, c is the average speed of sound along a radial ray and Δt_p is the approximate propagation time. Experimental evidence has shown that the majority of autoignition sites that arise in engines start as deflagrations. This means that the rate at which end gas is consumed (and thus the rate at which energy is released and pressure is increased) accelerates from

an initially small value to a much larger value over a measurable timescale that depends on the turbulent flame speed. A suitable knock onset detection algorithm must therefore possess the ability to locate a specific point within the autoignition transient, while remaining immune to random acoustic noise associated with combustion or various mechanical components.

A frequently employed method of detecting knocking cycles involves checking if the high-pass filtered cylinder pressure exceeds an arbitrary threshold. While this technique well suited to detecting the presence of a knocking cycle it is inadequate for identifying the time of knock onset. The primary reason for this inadequacy is the inherent delay between the start of autoignition and the threshold crossing (cf. Figure 4-10). Selecting a lower threshold reduces the delay, however the threshold can only be reduced to a value of approximately 500 mbar before normal pressure fluctuations occurring during combustion begin to trigger threshold crossings prematurely, this immediately results in large errors in the identified knock onset time. To assess the reliability of a range of knock onset detection algorithms the start of autoignition was manually identified for approximately four thousand cycles by selecting the first time at which significant deviation from the nominal cylinder pressure trajectory, followed by ringing was observed (cf. Figure 4-11). Several trial algorithms were developed based on various filtering and thresholding schemes however their performance proved extremely sensitive to the arbitrarily selected threshold. To avoid the selection of a threshold altogether a different type of algorithm was developed that attempts to locate a change in the magnitude of high frequency oscillations instead of a specific magnitude.

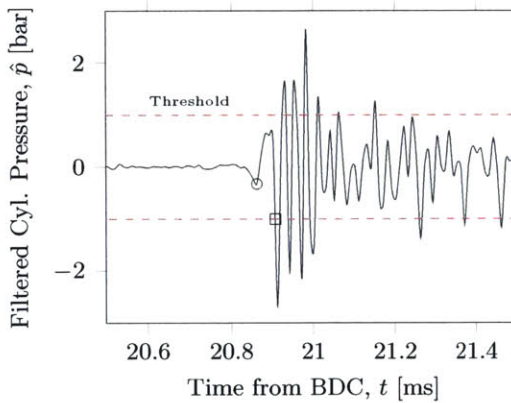


Figure 4-10: The high-pass filtered cylinder pressure (\hat{p}) oscillates during an autoignition event. The first 1 bar threshold crossing, indicated by the square, occurs roughly 50 μ s after anomalous pressure fluctuations are first observed.

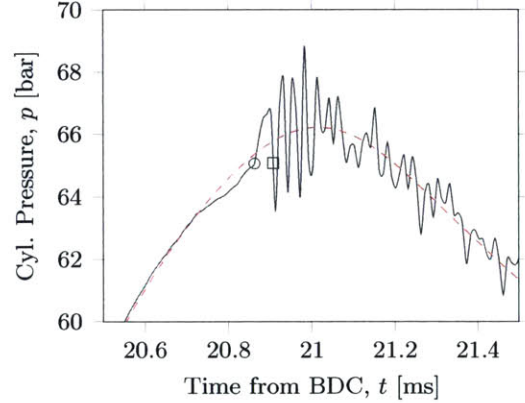


Figure 4-11: Comparing the measured cylinder pressure (p) to the low-pass filtered cylinder pressure aids in the manual identification of knock onset time, indicated by the circle, which is placed at the first sign of pressure rise beyond the smoothed curve that is followed by oscillatory ringing.

The proposed knock onset detection algorithm – which for ease of reference will be referred to as the oscillatory step detection (OSD) algorithm – uses cylinder pressure measurements to estimate the time at which autoignition occurs. First, the cylinder pressure data is filtered using a phase-preserving digital high-pass filter with a cutoff frequency of 2.5 kHz. Filtering removes the pressure

variations associated with normal compression and combustion leaving acoustic noise. Next the cumulative integral of the absolute value of the pressure oscillations is computed,

$$i_o(t) = \int_{t_0}^t |\hat{p}| dt, \quad (4.43)$$

where \hat{p} is the filtered cylinder pressure. The integrand of this expression ($|\hat{p}|$) can be considered a measure of the energy embodied in the high frequency pressure oscillations and thus i_o is representative of the total high frequency energy observed up to a given point in time. The expression presented in Eq. 4.43 is not to be confused with a similar integral from the literature referred to as the integral of the modulus of pressure oscillations (IMPO)^[14, 46]. The definition of IMPO, which is intended to provide a scalar knock metric, evaluates the same integral over a fixed crank angle window near TDC and thus provides no information regarding the temporal inception of autoignition.

An examination of the i_o profile of a knocking cycle allows three distinct stages of autoignition to be identified (cf. Figure 4-12). During normal combustion (prior to autoignition) the level of high frequency oscillation is stable and relatively small. The detected oscillations may be due to irregularities in the turbulent flame, mechanical vibrations or electrical noise in the sensed signal. The precise oscillation levels detected during this phase, which are reflected in the slope of i_o , vary from one cycle to the next. As autoignition begins the level of oscillation, and thus the slope of i_o increases rapidly. The magnitude of this change in slope and the time interval over which it occurs vary considerably under steady conditions, however the slope of i_o generally assumes a relatively constant value for 100 μ s to 300 μ s as autoignition occurs. Following the autoignition phase the slope of i_o steadily decays towards pre-autoignition levels as the high frequency pressure oscillations are damped out. The oscillatory step detection (OSD) algorithm has been developed to detect the transition between these stages of autoignition rather than particular levels of oscillation, a strategy which provides more robust performance in the presence of cycle-to-cycle variations in combustion and autoignition.

The OSD algorithm locates the start of autoignition by fitting linear segments with a step change in slope to the plot of i_o over a time interval near the point of maximum filtered pressure (cf. Figure 4-13). This is accomplished by defining a bilinear fit function

$$i_{o,fit}(t) = \begin{cases} c_0 - c_1(t - t_{ke}), & \text{if } t < t_{ke} \\ c_0 + c_2(t - t_{ke}), & \text{if } t \geq t_{ke} \end{cases} \quad (4.44)$$

which has four unknown constants c_0 , c_1 , c_2 and t_{ke} . These constants are determined by minimizing the root mean squared (RMS) error between i_o and $i_{o,fit}$ on an interval that ranges from 250 μ s before the earliest sign of autoignition to 100 μ s after the time at which $\max(|\hat{p}|)$ is observed. The time at which these lines intersect (t_{ke}) is defined as the onset time of autoignition. The value of t_{ke}

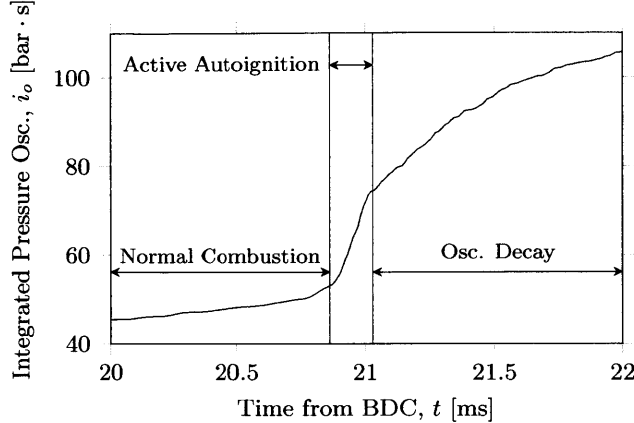


Figure 4-12: The three stages of autoignition are distinguishable on an i_o contour. During normal combustion i_o has a low, consistent slope which increases rapidly to a maximum value during the active autoignition stage. Following the active stage of autoignition the pressure oscillations are damped out, causing the slope to decay towards the value present during normal combustion.

so determined is not particularly sensitive to the choice of the lower bound of the fit interval because the slope of i_o during this period is relatively stable. However, the best results are obtained if the end time of the interval is selected before the oscillations have decayed significantly. The formulation of knock onset as the time at which a change in oscillatory energy is observed renders the OSD algorithm insensitive to the level of combustion noise, allowing it to work equally well for light (low intensity) and heavy (high intensity) knock. The algorithm is essentially locating the start of unusually large, sustained pressure oscillations, which is a criterion that is virtually synonymous with the definition of knock in automotive engines. Comparing the results of this algorithm to the results of manual knock onset identification yields a mean difference of 20 μ s (2 samples at 100 kHz) and a standard deviation in difference of 37 μ s (4 samples at 100 kHz) (cf. Figure 4-14). It is inaccurate to call the difference between the manually identified and OSD identified knock onset points an *error* because no claim can be made that either method locates the true start of autoignition. Instead the key feature of this comparison is that the algorithm has a tight standard deviation about the manually identified points and therefore it provides results that are generally in agreement with intuition regarding the start of knock and it is not unduly influenced by variations in combustion noise or knock intensity. This is clearly not the case for the thresholding approach which over the same dataset exhibits a mean difference of -72 μ s and a standard deviation of 300 μ s.

Summary of the Inferred Ignition Delay Approach

With practical methods of determining the cylinder pressure, end gas temperature, residual fraction and the observed knock onset time in place what remains is to develop a method of using this data to identify the ignition delay function. Owing to the speed at which modern computers can analyze systems of equations a nonlinear optimization approach was utilized to determine suitable values of

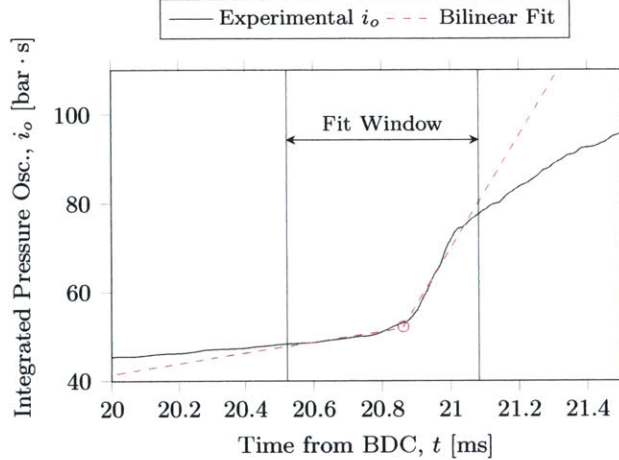


Figure 4-13: Two intersecting lines are fit to the i_{po} contour for a cycle in the region surrounding the maximum filtered pressure. The intersection of the two fit lines is identified as the time of knock onset as indicated by a circle. Note that adjustment of the fit window to incorporate only normal combustion and active autoignition does not materially affect the identified knock onset time.

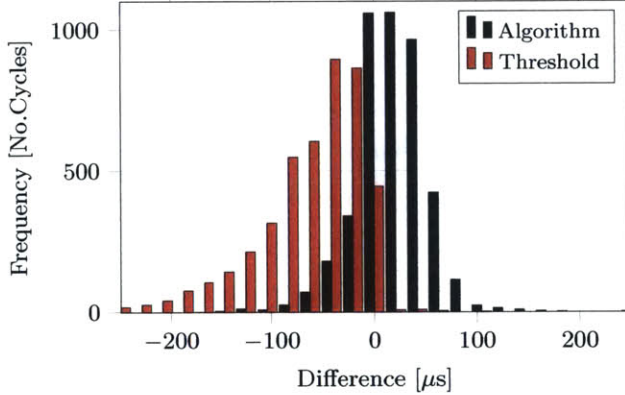


Figure 4-14: The difference between manually and automatically identified knock onset time for the proposed algorithm ($\mu = 20 \mu s$, $\sigma = 37 \mu s$) and the thresholding approach ($\mu = -72 \mu s$, $\sigma = 300 \mu s$).

the ignition delay constants a , b , c , and d from Eq. 4.40 based on the criterion of minimizing the RMS error between the observed knock onset time (from the OSD algorithm) and the modelled knock onset time (from the autoignition integral). Minimizing the RMS error in autoignition prediction time provides the major benefit of automatically determining the ignition delay function that provides the best autoignition prediction performance which, as discussed in the section on uncertainty, depends not only on the characteristics of the air-fuel mixture but the on the range of ignition delays generally observed in a particular engine. The following list summarizes the steps that make up the IID method as it has been applied in the present research across a range of steady state operating conditions:

1. Assume initial values of a , b , c and d . Using these values the function $\tau(p, T, w_d)$ is known.
2. For each set of steady state experimental data, compute the mean cylinder pressure trace, intake manifold air temperature, exhaust equivalence ratio, EGR rate and fuel flow rate.

3. Estimate the mean charge temperature at intake valve closing (T_{IVC}) and the residual fraction (w_r) using a calibrated engine model along with the mean parameters from step 2.
 4. For each experimental cycle within the steady state operating point perform the following steps:
 - (a) Assume that the mean values, T_{IVC} and w_r , computed in step 3 are the actual values and use them to compute the temperature history of the end gas by modeling the compression as an isentropic and adiabatic process.
 - (b) Compute the time history of $\tau(p, T, w_d)$ and the value of the autoignition integral as a function of time,
- (4.45)
- Locate, using interpolation, the time at which the value of the ignition integral first exceeds unity, this is the modelled knock onset time (t_{km}).
- (c) compute the experimental knock onset time (t_{ke}) using the OSD algorithm developed for this purpose. The error between observed and modelled knock may then be computed as,

$$e_k = t_{ke} - t_{km}. \quad (4.46)$$

Using this definition $e_k > 0$ implies that the model predicts knock before it is observed.

5. Compute the RMS value of the aggregated errors over all cycles and all steady state conditions then make adjustments to the values of a , b , c , and d to reduce the RMS error. Repeat the procedure from the first step until a minimum error is reached.

The optimization procedure described above was performed using the `fmincon` nonlinear minimization tool in MATLAB with a cost function

$$f(x) = \sqrt{\frac{1}{N} \sum_{n=1}^N \mathbf{e}_k^2} \quad (4.47)$$

where \mathbf{e}_k is a vector of length N containing the errors for each knocking cycle (e_k) in the set of experimental data used to determine the ignition delay expression.

4.3 Stoichiometric Knock Integral Correlation

The empirical constants presented in the following analysis were identified by performing the inferred ignition delay (IID) routine using experimental data at several speed, load, spark timing and EGR rate settings (cf. Table 4.2). Only data collected under stoichiometric conditions is considered at

this stage. Minimization of the RMS error between the modeled and observed time of autoignition over the 4219 knocking cycles that make up this dataset – specifically these are the cycles for which $\max |\hat{p}| \geq 1$ bar – yielded the empirical constants and ignition delay function:

Constant	Value	Unit
a	2.71×10^{-8}	s bar ^{1.73} K ^{-1.73}
b	1.73	-
c	5190	K
d	0.618	-

$$\tau(p, T, w_d) = 2.71 \times 10^{-8} (1 - w_d)^{-0.618} \left(\frac{p}{T} \right)^{-1.73} e^{\frac{5190}{T}} \quad [\text{s}], \quad (4.48)$$

where p is the cylinder pressure in bar, T is the end gas temperature in K and τ is returned in s.

Engine Speed [rpm]	GIMEP [bar]	Spark Timing [° bTDC]	EGR Rate	λ
1250	8 to 9	25 to 35	0 to 0.08	1
1500	10 to 14	10 to 42	0 to 0.125	1
1750	10 to 14	18 to 45	0 to 0.125	1
2000	11 to 14	22 to 42	0 to 0.125	1

Table 4.2: Experimental conditions for τ determination consist of 4219 individual knocking cycles from 336 unique steady state operating points.

A useful method of visualizing the accuracy of this ignition delay function is to plot the predicted time of autoignition against the time at which autoignition was observed for all knocking cycles, i.e. cycles with $\max |\hat{p}| \geq 1$ (cf. Figure 4-15), or to create an analogous plot on a crank angle resolved basis to eliminate the dependence of the data on engine speed (cf. Figure 4-16). Overall very good agreement between experimental and modeled knock onset time was observed with an R^2 value of 0.9993, mean error of 26 μs and standard deviation of 53 μs (cf. Figure 4-17). The positive mean error observed in the data is consistent with autoignition occurring at a point some distance from the pressure transducer, which results in a systematic error related to the propagation time of pressure oscillations. Using the propagation time approximation of Eq. 4.42 the distance between the autoignition site and pressure transducer that would result in the observed mean shift is approximately 26 mm, which is very close to the minimum distance between the pressure transducer and the cylinder wall (20 mm). In terms of crank angles the mean error is 0.20° and the standard deviation in error is 0.48°. Thus this ignition delay expression, when used in conjunction with the autoignition integral and corrected for acoustic propagation time is capable of predicting autoignition to within $\pm 1^\circ$ with 95% confidence.

In order to assess the sensitivity of the correlation to uncertainty in the measured or estimated quantities a perturbation of 5 K was introduced to the estimated charge temperature at intake valve closing (T_{IVC}). The modeled onset time of autoignition was then recomputed for all knocking cycles. This perturbation resulted in a mean shift in the error distribution from 26 μs to $-20 \mu\text{s}$ a net change of $-46 \mu\text{s}$. Similarly the independent introduction of a systematic pressure error of 0.1 bar resulted

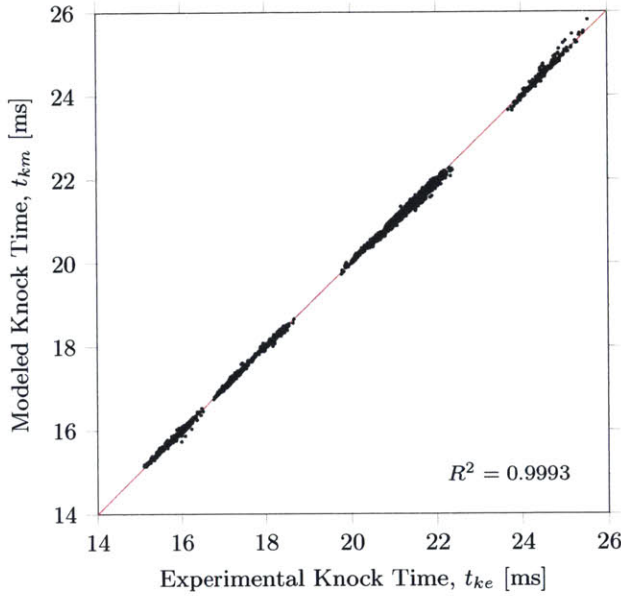


Figure 4-15: Correlation between the experimentally observed knock time (t_{ke}) correlates well with the knock time predicted by the autoignition model (t_{km}). Each cluster of points represents a different engine speed. Total of 4219 knocking cycles ($\max |\dot{p}| \geq 1$) under 336 steady state operating conditions.

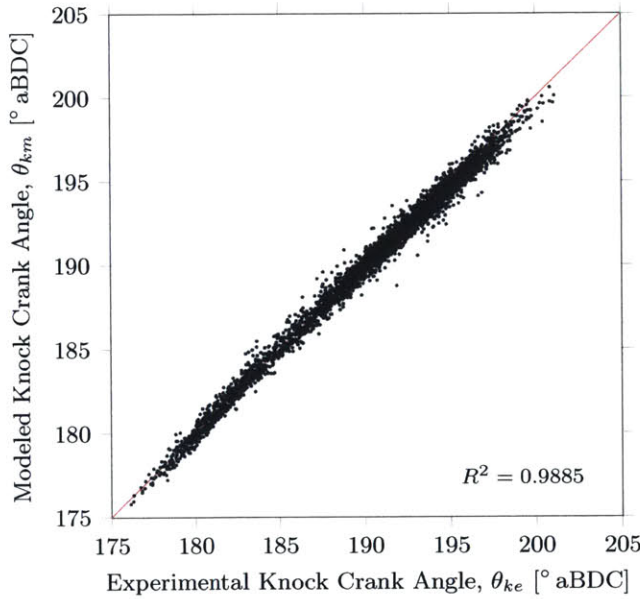


Figure 4-16: The data presented on a time basis (cf. Figure 4-15) may be plotted in terms of crank angles to collapse differences in timescale due to engine speed variation.

in a mean shift of 42 μs . Comparing these shifts to the distribution of errors in the correlated data one may estimate that a temperature uncertainty in T_{IVC} with a standard deviation of $\pm 5 \text{ K}$ is the most likely cause of the observed variations in prediction error. Cycle-to-cycle variation in the residual gas fraction is a likely cause of temperature fluctuations of this magnitude.

The range of temperatures and pressures over which the ignition delay has been inferred can be visualized by plotting the temperature and pressure at autoignition on a log p -log T diagram (cf. Fig-

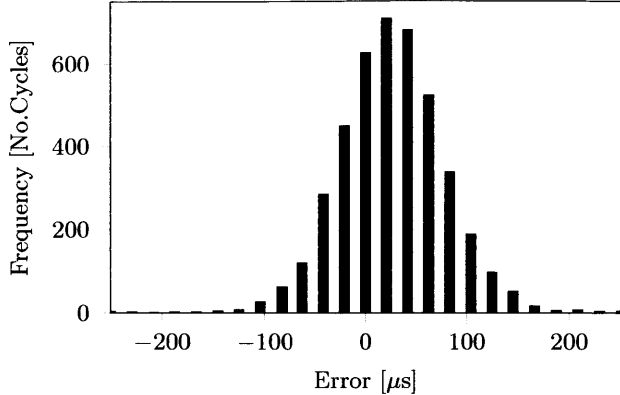


Figure 4-17: Histogram of error between modeled and experimental knock time. The distribution has a mean of 26 μs and a standard deviation of 53 μs . The positive mean value indicates that the model consistently predicts autoignition slightly before it is observed.

ure 4-18). Iso-delay contours constructed from Eq. 4.48 for the case $w_d = 0$ provide information on the ignition delays observed during experimental testing. For the experimental dataset studied here temperatures at autoignition range from 850 K to 1000 K and pressures at autoignition range from 48 bar to 81 bar. These values generally result in ignition delays between 0.5 ms and 1 ms at autoignition. Because the compression of the end gas is assumed to be adiabatic and isentropic the temperatures and pressures traversed to reach an autoignition state fall on a line with a slope of $(\gamma - 1)/\gamma$ on this log-log plot. Alternative contours for non-zero dilution rates may be constructed by computing the value of $(1 - w_d)^{-0.618}$ and multiplying the iso-delay contour levels by this value. For the data presented here the maximum dilution is 15% resulting in a multiplier of approximately 1.1 which does not alter the characteristics of this ignition delay contour plot appreciably.

The robustness of the ignition delay function was assessed by attempting to correlate the observed errors with various engine parameters. If the model and all of the measured or estimated parameters were accurate the observed errors would be random, and thus no correlation would be observed. This was precisely the case for engine speed, EGR rate, spark timing, GIMEP and several other engine parameters. However, it is interesting to examine several parameters that demonstrate weak correlation with error to identify aspects of the model or method that are potentially inaccurate. When error is plotted against CA50 the scatter is confined to a narrow band for CA50 values less than 5° aTDC (cf. Figure 4-19). However, as combustion phasing is retarded beyond this point the error band appears to curve upward indicating a systematic error in which the model predicts autoignition before it is observed. Such an error would occur if under these circumstances the ignition delay was smaller than the value that would result in accurate autoignition prediction. Recalling the alternative functional representations of τ given by Eq. 4.32 and Eq. 4.33 the primary difference between these forms was an additional dependence on the initial state of the charge as given by

$$C^* = \frac{p_i^{\gamma-1}}{T_i^\gamma} \quad (4.49)$$

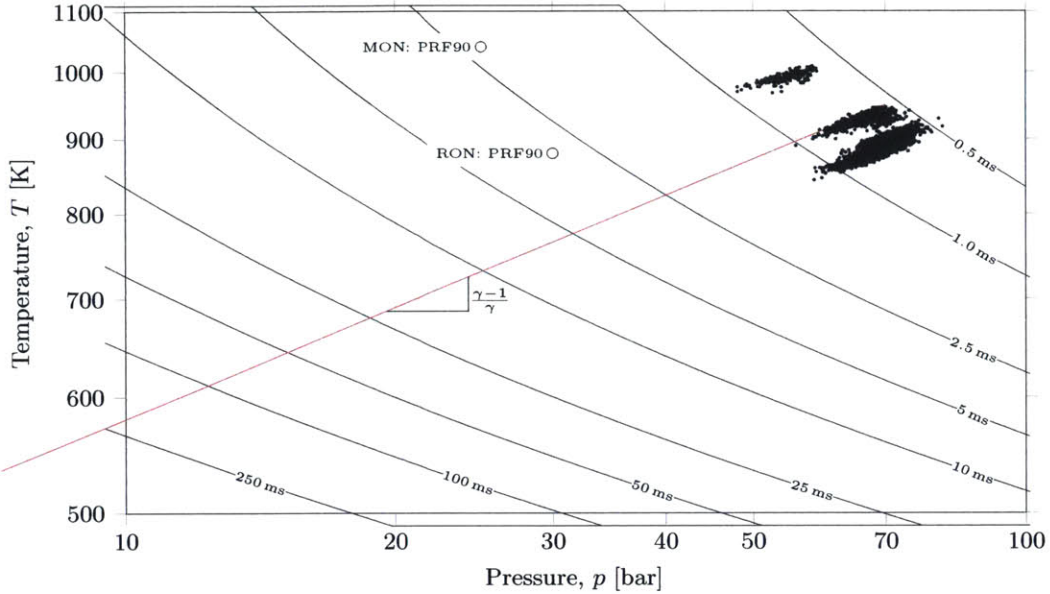


Figure 4-18: Iso-delay contours are plotted for 0.5 ms to 250 ms on the p - T plane with $w_d = 0$. The pressures and temperatures observed at autoignition are indicated as points and a representative p - T trajectory for an adiabatic and isentropic compression is shown. Ignition delays ranging from 0.5 ms to 1 ms are most common at the autoignition conditions. Alternative iso-delay contours for non-zero dilution rates may be constructed by multiplying the contour levels by $(1 - w_d)^{-0.618}$.

where p_i and T_i are the initial pressure and temperature of the charge respectively. It was deemed judicious to test for a correlation between this parameter and the error in modeled autoignition time to ensure that the correct functional form of the ignition delay has been selected. An analysis of the error revealed no correlation with the C^* parameter. Instead the strongest correlation detected was between the error and the ignition delay at knock (τ_k) (cf. Figure 4-20). For values of τ_k less than 0.7 ms the autoignition integral tends to predict autoignition later than it actually occurs, such an error would be caused by overestimating the ignition delay. Conversely at τ_k values greater than 0.7 ms the ignition delay appears to be overestimated. Such behavior is to be expected based on the observation that on $\log(\tau)$ - $1/T$ plots the relationship between the temperature and ignition delay of real fuels near ignition delays of 1 ms is generally concave down. Thus the linear form of the ignition delay used will tend to overestimate the ignition delays that are smaller and underestimate the ignition delays that are larger than the most frequently encountered values. Over the range of ignition delays that occur using Haltermann HF0437 in the GM LNF the error induced by this nonlinear fuel behavior is modest.

For completeness the same set of experimental data was correlated using an ignition delay expression with the form of Eq. 4.32 the resulting constants and ignition delay expression are

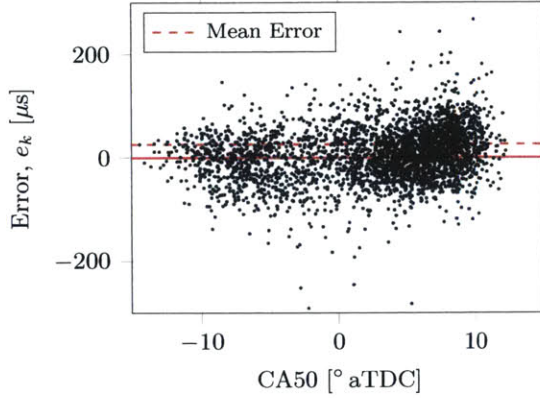


Figure 4-19: Error in the knock integral correlation is initially uncorrelated with CA50 for early combustion phasing, however near MBT combustion phasing the errors begin to deviate from the mean value. This can be traced back to the longer induction times when the engine is operated with late combustion phasing.

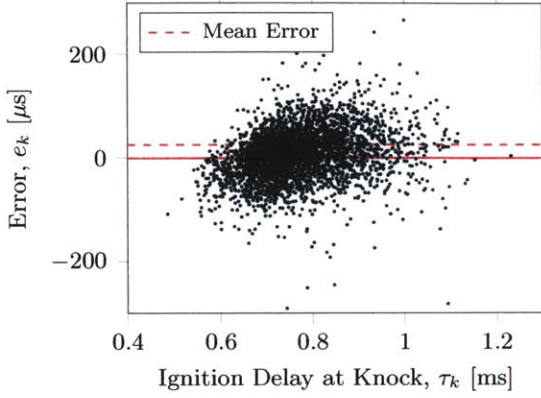


Figure 4-20: The best correlation is found between the ignition delay at knock and the error. Such a correlation most likely arises due to oversimplification of the mathematical form of the ignition delay. Recalling the typical shapes of ignition delay measurements (cf. Figure 4-4) the direction of the observed errors is consistent with the expected overestimation of smaller ignition delays and underestimation of larger delays.

Constant	Value	Unit
a	0.0131	s bar ^{1.72}
b	1.72	-
c	3940	K
d	1.14	-

$$\tau(p, T, w_d) = 0.0131(1 - w_d)^{-1.14} p^{-1.72} e^{\frac{3940}{T}} \quad [\text{s}]. \quad (4.50)$$

This expression has a similar mean error (8 μs) and standard deviation (50 μs) and exhibits the same type of correlation between the error and τ_k . The observation that both forms of the ignition delay expression seem to work equally well indicates that the autoignition process is not sensitive to the C^* parameter defined in the previous paragraph, or in other words the dependence of the ignition delay on volume concentration may be simplified to a dependence on pressure alone without loss of accuracy. The pressure and temperature dependence of this and the previous form of the ignition delay expression may be compared directly on a p - T map (cf. Figure 4-21) which demonstrates the level of similarity between the iso-delay contours. From a computational perspective the latter form of the ignition delay – as given by Eq. 4.32 – is superior owing to the clear separation between the b and c parameters. In comparison nonlinear optimization of Eq. 4.33 requires that the optimization algorithm find a balance between the b and c parameters due to the more complex temperature dependence of $T^b e^{c/T}$.

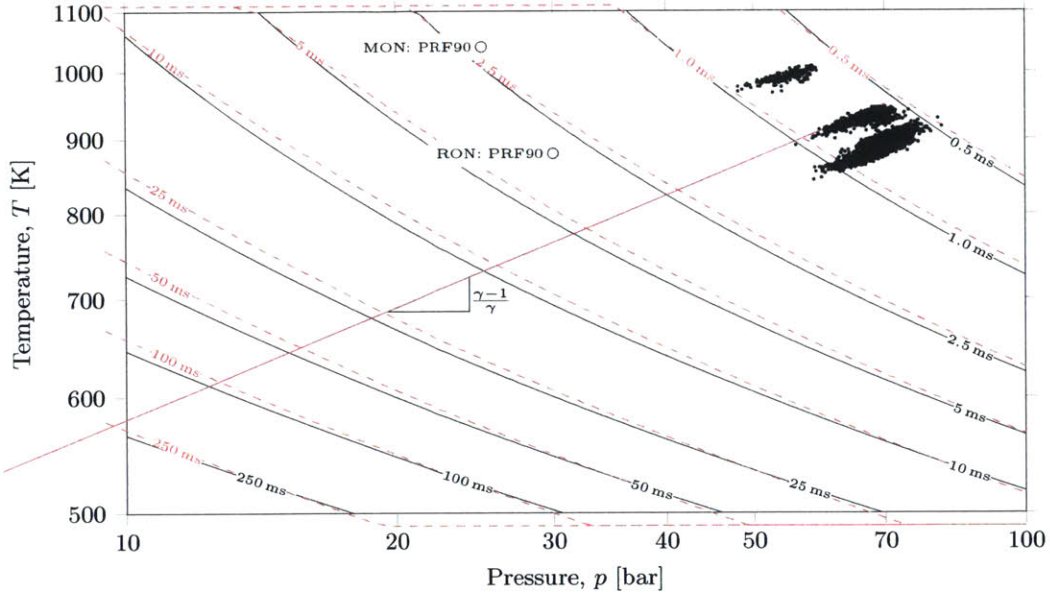


Figure 4-21: The iso-delay contours on the p - T map are very similar for Eq. 4.48 (black) and for Eq. 4.50 (red, dashed). They are particularly similar near the conditions at autoignition which are shown as points.

4.4 Non-Stoichiometric Knock Integral Correlation

The next stage in enhancing the knock integral correlation is to introduce variations in air-fuel ratio in conjunction with variations in EGR rate. When considering the correlation of air-fuel ratio in the presence of recirculated exhaust gasses it is clear that neither the metered EGR rate nor the equivalence ratio are *directly* related to the resultant composition of the charge and thus would make poor choices as correlating variables. Instead these two parameters interact to create a charge that consists of a mixture of air (m_a), fuel vapor (m_f), fully burned gasses (m_b) and partially oxidized fuel (m_p) which for the present will be assumed to consist of CO, H₂ and N₂ with negligible amounts of unburned hydrocarbons. Here the phrase “fully burned gases” is meant to refer to the mixture of N₂, CO₂ and H₂O that is produced by the stoichiometric combustion of the fuel. In the previous section dilution of the charge with fully burned gasses was included in the ignition delay correlation via the diluent mass fraction w_d . Thus the first task at hand is to identify the relationship between w_d , the EGR rate (w_{egr}) and the air-fuel equivalence ratio (λ). After a relationship for w_d has been developed corrections to the ignition delay correlation may be introduced that account for the amounts of excess air ($\lambda \geq 1$) or the amount of partially oxidized fuel ($\lambda < 1$) that make up the remainder of the cylinder contents. Neither of these components are pure diluents as they may participate in autoignition chemistry.

Composition Approximation

In the case of a stoichiometric charge the amount of fuel in the cylinder is precisely the amount required to react with all of the available air. When a EGR system is used and the engine is operated at a steady state stoichiometric condition it is reasonable to assume that the recirculation flow consists of fully burned gasses. This implies that the charge is made up of air and fuel in stoichiometric proportions and fully burned gases. Indeed this was the assumption of the previous section and the basis behind the definition of the diluent fraction w_d . The situation becomes somewhat more complex when the engine is operated lean ($\lambda > 1$) or rich ($\lambda < 1$).

During lean operation the amount of air trapped within the cylinder is in excess of the amount required to fully burn the available fuel. Thus a fraction of the air within the cylinder passes through the engine unaffected and enters the exhaust system. When a portion of the exhaust is recirculated some of the EGR mass flow will consist of air while the remainder will be made up of fully burned gases. In the first part of this analysis a parameter will be developed (δ) that represents the mass fraction of air in excess of the amount required to oxidize the available fuel. Next the δ parameter will be used to determine the mass fraction of fully burned gases contained within the charge (w_d). The simplest place to begin is the exhaust system. Here the air that was not oxidized during combustion is mixed with burned gases and if the exhaust from a single combustion event is considered the mass fraction of excess air in the exhaust ($w_{a,exh}$) is

$$w_{a,exh} = \frac{m_{a,e}}{m_{a,e} + m_b}, \quad (4.51)$$

where $m_{a,e}$ is the mass of excess air in the exhaust – or the mass of excess air in the cylinder – and m_b is the mass of burned gases. If one assumes that the mass flow rate of reactants into the cylinder is equal to the mass flow rate of products this expression may be related to the charge composition by

$$\frac{m_{a,e}}{m_{a,e} + m_b} = \frac{m'_a - m'_{a,s}}{m'_a + m'_f}, \quad (4.52)$$

where the prime notation (eg. m'_a) is used to indicate that m'_a need not represent the physical quantity of air in the charge but the total quantity of air (reduced or not) that has gone into the charge and the creation of its contents and $m'_{a,s}$ is the air requirement for the stoichiometric combustion of m'_f or mathematically,

$$m'_{a,s} = m'_f \left(\frac{m_a}{m_f} \right)_s, \quad (4.53)$$

where $\left(\frac{m_f}{m_a} \right)_s$ is the stoichiometric fuel-air ratio for the fuel being studied. Combining Eq. 4.52 with

Eq. 4.53 and manipulating yields

$$\frac{m'_a - m'_f \left(\frac{m_a}{m_f} \right)_s}{m'_a + m'_f} \cdot \frac{\frac{1}{m'_f}}{\frac{1}{m'_f} + 1} = \frac{\frac{m'_a}{m'_f} - \left(\frac{m_a}{m_f} \right)_s}{\frac{m'_a}{m'_f} + 1} = \frac{\lambda \left(\frac{m_a}{m_f} \right)_s - \left(\frac{m_a}{m_f} \right)_s}{\lambda \left(\frac{m_a}{m_f} \right)_s + 1} = \frac{\lambda - 1}{\lambda + \left(\frac{m_a}{m_f} \right)_s}. \quad (4.54)$$

Defining the parameter

$$\delta \equiv \frac{\lambda - 1}{\lambda + \left(\frac{m_f}{m_a} \right)_s}, \quad (4.55)$$

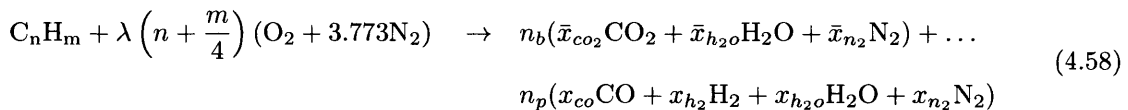
one arrives at the relationship

$$w_{a,exh} = w_{a,e} = \delta, \quad (4.56)$$

where $w_{a,e}$ is the mass fraction of excess air in the cylinder. Recognizing that the remainder of the exhaust and residuals are composed of burned gases the diluent fraction – which is to say the mass fraction of fully burned gasses in the charge – is given by

$$w_d = [w_r + w_{egr}](1 - \delta), \quad \text{if } \lambda \geq 1. \quad (4.57)$$

The situation that occurs during rich operation is considerably more complex, with the primary components of the exhaust being CO₂, H₂O, N₂, CO and H₂. The system of equations that governs the exhaust composition during rich operation is well known^[29], however the intent of the present analysis is to develop an approximate formulation of the composition that can be employed in conjunction with the ignition delay correlation. If sufficient resources are available the more rigorous and precise solution to the combustion equation may be substituted for the method presented here. The combustion reaction may be written by separating the portion that has the exact composition of stoichiometric exhaust as follows:



where \bar{x}_i are the mole fractions of component i in stoichiometric exhaust, n_b is the number of fully burned moles, n_p is the number of partially burned moles and x_i is the molar fraction of component i in the partially burned mixture. The unknowns in this chemical equation are n_b , n_p , x_{co} , x_{h_2} , x_{h_2o} and x_{n_2} . Performing a chemical balance of H, C, O and N provides four of the necessary six equations. Additionally the mole fractions of the partially burned mixture must sum to unity thus

$$x_{co} + x_{h_2} + x_{h_2o} + x_{n_2} = 1. \quad (4.59)$$

The final equation used to close the system is based on the water-gas shift mechanism which is

generally implemented by assuming

$$\frac{n_{h_2} n_{co}}{n_{co_2} n_{h_2}} = 3.5 \quad (4.60)$$

which may be rearranged to provide the relationship

$$\frac{(n_b \bar{x}_{h_2o} + n_p x_{h_2o}) x_{co}}{n_b \bar{x}_{co_2} x_{h_2}} = 3.5. \quad (4.61)$$

This system of equations may be solved allowing the composition of the burned gases to be determined. Suppose that the exhaust from a single combustion event is separated into the fully burned portion (m_b) and partially burned portion (m_p) along the lines of Eq. 4.58. The mass fraction of partially burned mixture in the exhaust is given by

$$w_p = \frac{m_p}{m_p + m_b} \quad (4.62)$$

If the total mass of the reactants and products remains unchanged the denominator of this expression may be altered to reflect the composition of the charge prior to combustion

$$w_p = \frac{m_p}{m'_a + m'_f} = \frac{\frac{m_p}{m'_a}}{1 + \frac{m'_f}{m'_a}} = \frac{\frac{m_p}{m'_a}}{1 + \frac{1}{\lambda} \left(\frac{m_f}{m_a} \right)_s} = \frac{\lambda \frac{m_p}{m'_a}}{\lambda + \left(\frac{m_f}{m_a} \right)_s} \quad (4.63)$$

here the prime notation is again used to indicate that m'_a represents the mass of air in the charge in addition to the mass of air required to form any of its oxidized components. If an approximate air-fuel ratio of the partial oxidation is defined as

$$\frac{m'_{ap}}{m'_{fp}} = \left(\frac{m_a}{m_f} \right)_p \quad (4.64)$$

where m'_{ap} and m'_{fp} are the masses of air and fuel respectively used to create the partially oxidized products then the ratio in the numerator of Eq. 4.63 may be expressed as

$$\frac{m_p}{m'_a} = \frac{m'_{fp} \left(1 + \left(\frac{m_a}{m_f} \right)_p \right)}{\lambda m'_f \left(\frac{m_a}{m_f} \right)_s} = \frac{1 + \left(\frac{m_a}{m_f} \right)_p \psi}{\left(\frac{m_a}{m_f} \right)_s}, \quad (4.65)$$

where $\psi \equiv m_{fp}/m_f$, or in words ψ is the mass fraction of the fuel that is used to create the partially oxidized products. An examination of the results of numerical solutions to Eq. 4.58 indicate that for a limited range of air-fuel ratios ψ may be approximated by

$$\psi \approx 2.4(1 - \lambda), \quad \text{if } 0.8 < \lambda < 1. \quad (4.66)$$

Combining this approximation with Eq. 4.63 and Eq. 4.65 yields

$$w_p = \frac{\psi}{\lambda + \left(\frac{m_f}{m_a}\right)_s} \frac{1 + \left(\frac{m_a}{m_f}\right)_p}{\left(\frac{m_a}{m_f}\right)_s} = \frac{2.4(1 - \lambda)}{\lambda + \left(\frac{m_f}{m_a}\right)_s} \frac{1 + \left(\frac{m_a}{m_f}\right)_p}{\left(\frac{m_a}{m_f}\right)_s}. \quad (4.67)$$

Recalling the definition of δ this equation may be simplified to

$$w_p = -2.4\delta \frac{1 + \left(\frac{m_a}{m_f}\right)_p}{\left(\frac{m_a}{m_f}\right)_s}. \quad (4.68)$$

Based on the numerical simulation an estimate of the characteristic air to fuel ratio of the partially oxidized products is

$$\left(\frac{m_a}{m_f}\right)_p \approx 6.75, \quad (4.69)$$

which when combined with the stoichiometric air-fuel ratio of 14.6 indicates that

$$w_p \approx -1.27\delta, \quad \text{if } 0.8 < \lambda < 1. \quad (4.70)$$

Taking care to note that δ is negative during rich operation. This approximation provides an estimate of the partially burned mass fraction that is accurate to within $\pm 5\%$ over the air fuel ratio range of interest. It can therefore be used to correct the amount of fully burned gas that dilutes a charge when the engine is operated under rich conditions with EGR. The diluent (fully burned) mass fraction in the charge during rich operation is given by

$$w_d = [w_r + w_{egr}](1 + 1.27\delta), \quad \text{if } 0.8 < \lambda < 1. \quad (4.71)$$

It may also be shown that the amount of fuel above and beyond the amount that could be consumed by stoichiometric combustion with air is given by

$$w_{f,e} = -\delta \left(\frac{m_f}{m_a}\right)_s, \quad (4.72)$$

when $w_{egr} = w_r = 0$.

In summary, the composition of the charge has been decomposed into three distinct parts: a diluent component (w_d) which is composed of inert burned gases in the ratios created by stoichiometric combustion, a stoichiometric mixture which consists of air and fuel in the chemically correct ratios, and either a fraction of excess air ($w_{a,e}$, when lean) or excess fuel ($w_{f,e}$ when rich). The formulae that model the composition have been tabulated for reference (cf. Table 4.3).

Exhaust	Stoichiometric	Lean	Rich
Fully Burned (w_b)	1	$1 - \delta$	$1 - 1.27(-\delta)$
Excess Air (w_a)	–	δ	–
Partially Burned (w_p)	–	–	$1.27(-\delta)$
Charge	Stoichiometric	Lean	Rich
Fully Burned (w_d)	$w_r + w_{egr}$	$[w_r + w_{egr}](1 - \delta)$	$[w_r + w_{egr}](1 - 1.27(-\delta))$
Partially Burned (w_p)	–	–	$[w_r + w_{egr}](1.27(-\delta))$
Excess Air ($w_{a,e}$)	–	δ	–
Excess Fuel ($w_{f,e}$)	–	–	$(-\delta) (m_f/m_a)_s - w_p (m_f/m_a)_p$

Table 4.3: Composition of the exhaust and charge for lean, stoichiometric and rich operation with EGR. Note that δ is negative for the fuel rich case.

Ignition Delay Extension

There are many methods in which changes in charge composition may be introduced into the ignition delay correlation. The method pursued in the present work is to consider excess fuel and excess air as diluents to be compared with burned gasses. The amounts of excess air and fuel are therefore included in the dilution term of the previously developed ignition delay correlations. During lean operation the additional component of the charge is air with a mass fraction equal to δ , introducing this additional dilution component with a constant of proportionality k_l yields a general form of the ignition delay

$$\tau(p, T, w_d) = 2.71 \times 10^{-8} (1 - w_d - k_l \delta)^{-0.618} \left(\frac{p}{T} \right)^{-1.73} e^{\frac{5190}{T}}, \quad \text{if } \lambda \geq 1. \quad (4.73)$$

For the rich case there are two components of interest. The charge contains fuel in excess of the amount that could be consumed with the available air and partially burned gasses. Under most conditions the mass fraction of partially burned gasses in the charge – specifically the mixture of CO, H₂, H₂O and N₂ represented by w_p – makes up less than 5% of the charge by mass, with the large majority of this being the inert N₂ and H₂O. As such w_p is expected to behave in a manner similar to the diluent w_d . To simplify the formulation of the ignition delay these terms were treated interchangeably. To account for the additional fuel added under rich conditions the approximation $w_{f,e} \approx (-\delta) (m_f/m_a)_s$ was used which is obtained by assuming the fuel value of the recirculated gases is negligible. Introducing these new terms into the ignition delay equation developed in the previous section one arrives at

$$\tau(p, T, w_d) = 2.71 \times 10^{-8} (1 - w_d - w_p - k_r(-\delta))^{-0.618} \left(\frac{p}{T} \right)^{-1.73} e^{\frac{5190}{T}}, \quad \text{if } \lambda < 1. \quad (4.74)$$

where the stoichiometric air-fuel ratio has been absorbed into the unknown proportionality constant k_r . A similar development may be used with the alternative form of the ignition delay to arrive at

the analogous expressions

$$\tau(p, T, w_d) = \begin{cases} 0.0131(1 - w_d - k_l \delta)^{-1.14} p^{-1.72} e^{\frac{3940}{T}}, & \text{if } \lambda \geq 1, \\ 0.0131(1 - w_d - w_p - k_r(-\delta))^{-1.14} p^{-1.72} e^{\frac{3940}{T}}, & \text{if } \lambda < 1. \end{cases} \quad (4.75)$$

The constants k_r and k_l were determined by nonlinear optimization using a data set that consisted of a range of non-stoichiometric operating points (cf. Table 4.4). The optimization routine indicated that acceptable values of k_l and k_r are close to unity and very nearly equal. Using the values $k_r = k_l = 0.95$ allows the ignition delay to be expressed for all air fuel ratios as

$$\tau(p, T, w_d) = 2.71 \times 10^{-8} (1 - w_d - w_p - 0.95|\delta|)^{-0.618} \left(\frac{p}{T}\right)^{-1.73} e^{\frac{5190}{T}} \quad (4.76)$$

The proportionality constant $k = 0.95$ indicates that during lean operation excess air is less effective as a diluent than burned gasses. This is to be expected based on the observation that the oxygen within excess air may participate in autoignition chemistry. During fuel rich operation this value indicates that the ignition delay is quite sensitive to the quantity of excess fuel, which tends to have the same effect as a diluent. There is evidence to suggest that this relationship between excess fuel and increased ignition delays – which has been observed in heptanes – is caused by the reduction of oxygen concentration^[55].

Engine Speed [rpm]	GIMEP [bar]	Spark Timing [° bTDC]	EGR Rate	λ
1250	8 to 9	10 to 42	0 to 0.10	0.8 to 1.3, $\lambda \neq 1$
1500	10 to 14	10 to 42	0 to 0.10	0.8 to 1.3, $\lambda \neq 1$
1750	10 to 14	18 to 45	0 to 0.10	0.8 to 1.3, $\lambda \neq 1$
2000	11 to 14	22 to 42	0 to 0.10	0.8 to 1.3, $\lambda \neq 1$

Table 4.4: Table of operating points for optimization of k_r and k_l , this data set consists of 4537 non-stoichiometric knocking cycles.

Correlation between the experimental and modeled knock onset time is good (cf. Figure 4-22). However the mean error of 32 µs and standard deviation of 59 µs are somewhat higher than the stoichiometric data (cf. Figure 4-23). Examination of the error as a function of the ignition delay at knock reveals that the model systematically predicts autoignition before it occurs when the ignition delay is larger than normal at autoignition and after it occurs when the ignition delay is smaller than normal (cf. Figure 4-24). As discussed in the previous section this is most likely caused by differences between the fuel behavior and the mathematical model of the ignition delay. The error does not appear to correlate with equivalence ratio, engine speed or other operational parameters.

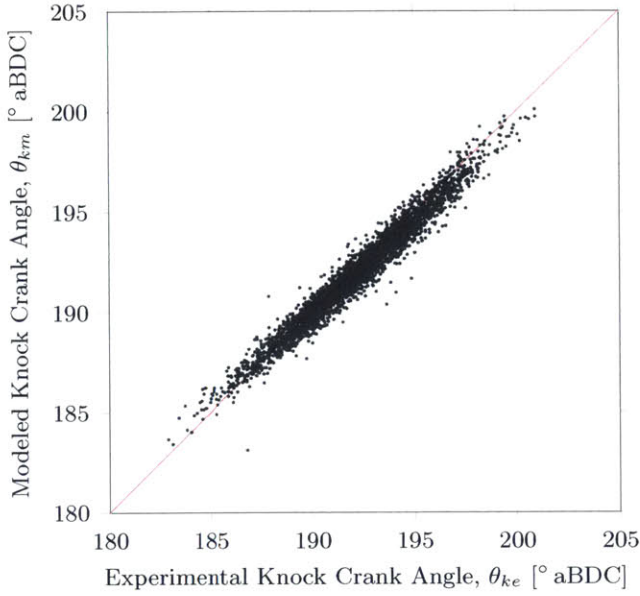


Figure 4-22: Correlation between the experimentally observed knock crank angle (θ_{ke}) and the crank angle of knock predicted by the autoignition model (θ_{km}). This correlation is not as strong as the stoichiometric correlation indicating that there is some work still to do in the identification of appropriate correlating parameters.

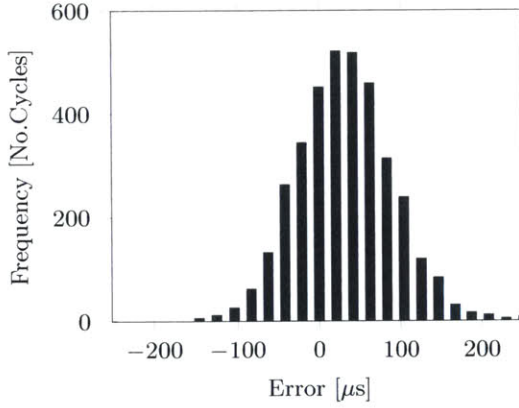


Figure 4-23: Histogram of error between modeled and experimental knock time. The distribution has a mean of 32 μ s and a standard deviation of 59 μ s. The positive mean value indicates that the model consistently predicts autoignition slightly before it is observed.

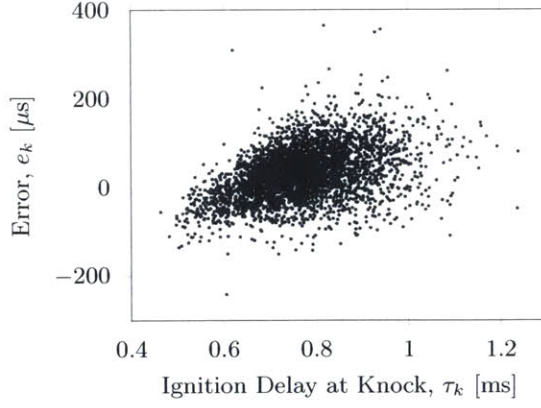


Figure 4-24: The error in autoignition prediction is correlated with the ignition delay at knock. This correlation is consistent with a mathematical ignition delay model that overestimates the ignition delay when it is lower than typical values at autoignition and overestimates ignition delay values that are larger.

4.5 Statistical Autoignition Model

The variations that occur from one cycle to the next within an engine are an inescapable reality of engine design and operation. Some factors, such as the rate of flame kernel development, are extremely difficult to control^[33, 37]. Others, like variation in the precise amount of fuel delivered present more well defined challenges. Some of the key factors that drive variation in autoignition are heat release schedule, residual fraction, charge temperature at IVC, charge air-fuel ratio and

trapped charge mass. Of these only variations in the heat release schedule and trapped charge mass (through the cylinder pressure measurements) are included in the present analysis with cycle specific accuracy. The remaining parameters are only included as constant mean values for a given steady state operating point. One may question whether or not the inclusion of heat release variation alone is sufficient. Surely conditions exist under which variations in residual fraction or charge temperature may be critical, however, as evidenced by the accuracy of the knock integral correlation the vast majority of conditions are only minimally affected by the unmeasured variations. Furthermore the conditions under which variations in residual fraction, charge temperature and other factors become significant are generally avoided to meet the concurrent demands for a smooth-running, low-emission engine. Thus there seems to be little need to introduce the complex systems required to provide additional cycle resolved measurements because the overall knock characteristics of the engine are not particularly sensitive to the variations that occur within the operational regimes of the most concern. However, the cycle-to-cycle variations do result in a considerable variation in the intensity of individual autoignition events. The goal of the present discussion is to develop a method to estimate the variations in knock intensity that may be expected under particular steady state conditions.

The cycle specific use of cylinder pressure measurements and the computation of a pseudo-cycle specific end gas temperature using this pressure measurement are a critical component of accurate knock prediction. The combustion phasing, as measured by CA50, varies considerably at steady state. The variation in CA50 at a given operating point is largely - although not wholly - responsible for the presence of both knocking and non-knocking cycles under steady conditions (cf. Figure 4-25). This suggests that one potential strategy to delay the onset of autoignition may be to reduce the levels of cycle-to-cycle variation that result in changes to CA50. In particular changes to the ignition system could potentially allow the knock limited CA50 to be improved on the order of 2° . Improvement beyond this level calls for methods that investigate not only the stochastic occurrence of knock but also the severity of each event.

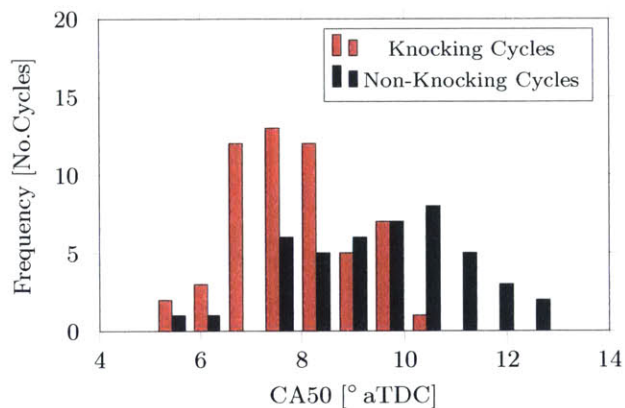


Figure 4-25: Variation in CA50 alone is insufficient to describe the presence of both knocking and non-knocking cycles at a steady state operating point.

Knock Intensity Observations

In order to link the severity of knock to the physical and objective limits of an engine it is helpful to define a measure of the *knock intensity*. The purpose of this metric is to quantify how energetic and potentially damaging each individual knock event has been. The method of knock intensity computation used in this work is widely applied^[46, 61] and is straightforward to implement. The knock intensity (KI) is computed by finding the maximum value of the high-pass filtered cylinder pressure for each cycle. The filter used is identical to the filter described in section Sec. 4.2, a digital high-pass filter with a cutoff frequency of 2.5 kHz. Using \hat{p} to identify the filtered cylinder pressure the knock intensity can be expressed as

$$KI = \max(|\hat{p}|), \quad (4.77)$$

where the absolute value is used to locate the filtered pressure measurement with the largest amplitude regardless of sign. Using this definition the knock intensity inherits the units of the pressure measurements, in this case values of KI will be reported in bar. The threshold for classifying a cycle as knocking varies in the literature but for the present work a threshold of 1 bar has been used. High frequency pressure fluctuations in the range of 0.2 bar to 0.5 bar are typical of normal combustion. The mechanisms through which autoignition mechanically damages the internal components of an engine are complex and depend on local geometry, temperatures and pressures which are not accurately reflected in the bulk cylinder pressure transducer measurements^[38, 24]. Crevices, in particular the piston top land crevice, may be subjected to local pressures in excess of 300 bar during an autoignition event, causing microscopic cracking and pitting of aluminum piston surfaces^[47]. Thermal effects such as the spherodization of carbon in cast iron parts result in geometrical changes and hardening, particularly of the piston rings. This thermal damage has been observed in engines running with KI values of 5 bar, resulting in moderate closure of the piston ring gap^[47]. Another aspect of the knock limits imposed on production engines is the contribution of knock to limits on noise, vibration and harshness (NVH). The contribution of knock to NVH is measured well by KI as it measures pressure variations at acoustic frequencies. For the purpose of uniformity and generality the knock intensity will be defined for all cycles, and thus the knock criterion can be restated as $KI \geq 1$ bar.

If the knock intensity of each cycle is plotted under steady conditions a substantial amount of variation is observed (cf. Figure 4-26). As noted earlier, some of this variation can be attributed to fluctuations in CA50 (cf. Figure 4-27). The variation in both knock intensity and CA50 appear to be stochastic, thus a probabilistic approach to describing the cycle-to-cycle variation was pursued. If the knock intensity data collected at one steady state operating point is binned and the probability density of each bin is computed, the resulting histogram may be compared to the probability density

functions of various distribution types. This analysis indicates that the knock intensity probability distribution is modeled well using a lognormal distribution (cf. Figure 4-28). The lognormal distribution is characterized by a probability density function that possesses zero probability for values at or below zero and a long tail to the right of a probability density peak. These boundary conditions match the constraints on knock intensity which is not defined for negative numbers. The lognormal distribution can be most readily understood by its definition based on the normal distribution, which states that if the variable z is lognormally distributed then $\log(z)$ is normally distributed. If the parameters μ and σ are computed using

$$\begin{aligned}\mu &= \text{mean}(\log(z)), \\ \sigma &= \text{std}(\log(z)),\end{aligned}\tag{4.78}$$

then the probability density function is

$$f(z; \mu, \sigma) = \frac{1}{z\sigma\sqrt{2\pi}} e^{-\frac{(\ln(z)-\mu)^2}{2\sigma^2}}.\tag{4.79}$$

It is worth emphasizing that μ and σ are not the mean and standard deviation of the lognormally distributed variable (z) but of its logarithm ($\log(z)$), they are often called the location and scale parameters respectively. The cumulative distribution function associated with this probability density function is

$$F(z; \mu, \sigma) = \frac{1}{2} \left[1 + \text{erf} \left(\frac{\ln(z) - \mu}{\sigma\sqrt{2}} \right) \right],\tag{4.80}$$

where $\text{erf}()$ denotes the error function^[6]. Using a lognormal model for knock intensity simplifies the analysis of cycle-to-cycle variation by reducing the behavior under specific steady state operating conditions to two parameters, the location parameter (μ) and the scale parameter (σ).

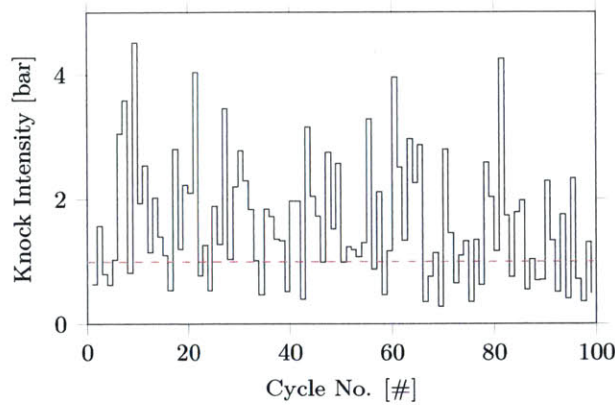


Figure 4-26: Variation of knock intensity from one cycle to the next.

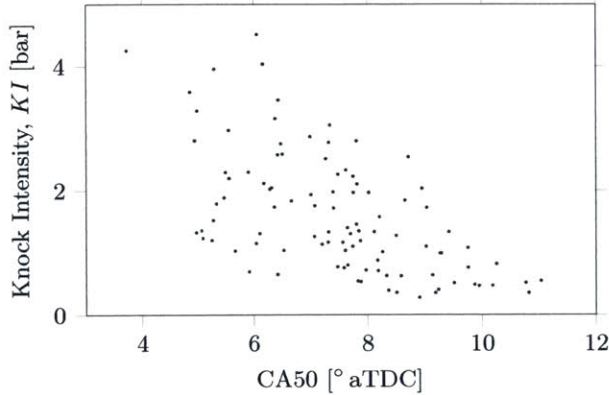


Figure 4-27: Some of the variation in knock intensity may be attributed to variation in CA50. However, as evidenced by the vertical spread, combustion phasing alone does not account for all of the CA50 variation.

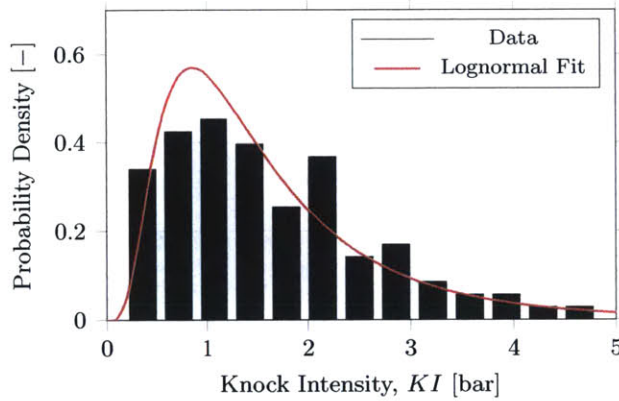


Figure 4-28: The probability density histogram of experimental data agrees well with a lognormal fit.

The Search for Parameters that Affect Knock Intensity

The isolation of the location parameter and the scale parameter from experimental data gathered at steady state generates the possibility to develop a correlation between these parameters and known experimental conditions. This correlation would allow the distribution of knock intensity values to be estimated in advance of experimental testing, saving considerable time and effort and adding a valuable interpolating tool to sparsely sampled datasets. With numerous types of variations occurring from one cycle to the next the principle issue in developing a correlation of this type is to identify the parameter with the simplest and most robust relationship to μ and σ . The following hypothesis was developed to aid in this search:

In the case that inhomogeneities exist within the end gas there will be regions which, when considered individually, will have different values of the autoignition integral. Suppose that each of these regions autoignites when its local autoignition integral exceeds unity. If the knock intensity scales with the rate of autoignition then conditions under which the time derivative of the autoignition integral is high near the time of autoignition will exhibit a higher knock intensity.

Each component of this hypothesis is based on experimental evidence and merits individual elaboration. The first component states that the end gas is not homogeneous, a fact which has been demonstrated in many ways including computational fluid dynamics and direct observation of the charge through quartz windows. The inhomogeneities that are most significant to autoignition are temperature and composition, both of which enter the ignition delay computation. Measurements using LIF techniques have shown that the spatial variation in temperature of the end gas of a firing engine may be in the range of $\pm 15\text{ K}$ ^[19]. Although this uncertainty may seem small in comparison to typical mean temperatures of 850 K the ignition delay function is very sensitive to differences in temperature, particularly when the ignition delay is small. The next component of the hypothesis is that each region of the end gas will autoignite when its local autoignition integral exceeds one. This statement is justified if one has the ability to follow a portion of the end gas as it changes size and position in the cylinder but does not mix well with other regions. Given the timescales involved in the most critical stages of autoignition (combustion to shortly after TDC) it is unlikely that mixing appreciably alters the composition or temperature of the adiabatic core of macro-scale end gas pockets. Thus if each pocket is treated individually the autoignition integral should still apply to its core. The autoignition of several distinct regions has often been observed in optical engines^[45, 38, 36]. The next component of the hypothesis asserts that the knock intensity scales with the maximum rate of autoignition. Since autoignition generally occurs rapidly the angle through which the crank rotates during combustion is small. However, if the autoignition of the end gas occurs at rates comparable to those of normal combustion the autoignition region behaves as if it is locally unconstrained, expanding with little or no impact on the primary flame and minimal high frequency pressure oscillations. Under these conditions a portion of the energy released is shared with the entire cylinder by increasing the pressures throughout. As the rate of heat release during autoignition is increased the degree of expansion possible during the autoignition event becomes increasingly limited, resulting in higher more localized pressures which propagate throughout the cylinder at the speed of sound. In the limit of a detonation the fuel energy is released at near constant volume, resulting in the formation of a strong pressure wave. Thus although the precise scaling is complex and depends on many geometrical and compositional factors it appears plausible that autoignition rate and knock intensity are closely related quantities. The final component of the hypothesis connects the autoignition rate and mass to the bulk ignition integral slope. The development of this relationship is most readily accomplished by mathematical analysis.

Recall that based on the mean cylinder conditions the autoignition integral is defined as,

$$I(t) = \int_{t_0}^t \frac{1}{\tau(p, T, w_d)} dt \quad (4.81)$$

where t_0 is a time at which the ignition delay is very large ($I(t_0) \equiv 0$) and τ is the ignition delay function. The condition for autoignition is,

$$I(t_k) = 1, \quad (4.82)$$

where t_k is the time of autoignition. Suppose that shortly before t_k the local values of the autoignition integral at various points through the end gas are normally distributed with a mean value of $I_\mu(t)$ and a standard deviation of I_σ (cf. Figure 4-29). This implies that the fraction of potential autoignition sites that have crossed the autoignition limit at time t is given by,

$$w_i(t) = 1 - \frac{1}{2} \left[1 + \operatorname{erf} \left(\frac{1 - I_\mu(t)}{I_\sigma \sqrt{2}} \right) \right]. \quad (4.83)$$

Based on the definition of Eq. 4.81 it is reasonable to presume that

$$\begin{aligned} I_\mu(t) &= I(t) \approx I(t_k) + \frac{d}{dt} [I(t)]_{t_k} (t - t_k) \\ &\approx 1 + \frac{d}{dt} \left[\int_{t_0}^t \frac{1}{\tau} dt \right]_{t_k} (t - t_k) \\ &\approx 1 + \frac{1}{\tau_k} (t - t_k). \end{aligned} \quad (4.84)$$

Substituting this result into the previous expression one arrives at

$$w_i(t) = \frac{1}{2} \left[1 - \operatorname{erf} \left(\frac{\frac{1}{\tau_k} (t_k - t)}{I_\sigma \sqrt{2}} \right) \right]. \quad (4.85)$$

Taking the time derivative of this equation one finds that the normalized rate of ignition is given by,

$$\frac{dw_i}{dt}(t) = \frac{1}{\sqrt{2\pi}} \left[\frac{1}{\tau_k I_\sigma} \right] e^{-\left(\frac{(t_k-t)}{\tau_k I_\sigma \sqrt{2}}\right)^2}. \quad (4.86)$$

Evaluating this derivative at time t_k simplifies the expression significantly, yielding

$$\frac{dw_i}{dt}(t_k) = \frac{1}{I_\sigma \sqrt{2\pi}} \left[\frac{1}{\tau_k} \right]. \quad (4.87)$$

The result developed in Eq. 4.87 has several important implications. First, a connection may be developed between the normalized rate of autoignition – which is the rate of autoignition per unit end gas – and the rate at which heat is released. The mass of the unburned gasses (m_u) changes as a function of time and thus the total mass available for autoignition is decreasing as the flame consumes the end gas. At a given point in time the rate at which unburned gasses are crossing the

autoignition limit is therefore given by

$$\frac{dm_i}{dt} = m_u \frac{dw_i}{dt}, \quad (4.88)$$

where m_i is the mass of unburned mixture that is autoignited. The rate at which the mixture autoignites is very closely related to the rate of heat release. If the heat release per unit mass of end gas consumed is constant the rate of heat released by autoignition is

$$\frac{dQ_i}{dt} = \frac{dm_i}{dt} w_f Q_{LHV}, \quad (4.89)$$

where w_f is the mass fraction of fuel in the unburned mixture and Q_{LHV} is the lower heating value of the fuel. Combining these expressions the rate of heat release due to autoignition is approximately

$$\frac{dQ_i}{dt} = \frac{dw_i}{dt} \cdot m_u w_f Q_{LHV}. \quad (4.90)$$

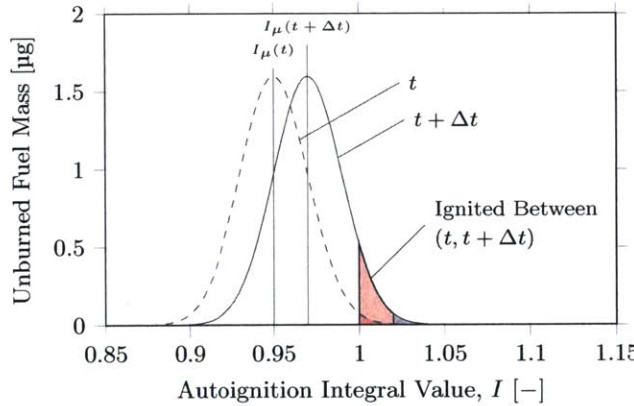


Figure 4-29: If the values of the autoignition integral for macro-scale end gas parcels are normally distributed a portion of the end gas will cross the autoignition limit in time Δt . The factors that govern the rate at which the available fuel crosses the autoignition limit are primarily the rate of change of I_μ and the distribution width I_σ .

At this stage recall that the metric of knock severity is the knock intensity (KI) which is defined as the maximum absolute value of the filtered cylinder pressure

$$KI \equiv \max |\hat{p}|. \quad (4.91)$$

The pressure oscillations captured by \hat{p} within the cylinder occur at frequencies that represent the fundamental vibratory modes of the gases contained within^[10]. If, for simplicity, a single sinusoidal frequency component is considered there is a definite relationship between the maximum amplitude

of the pressure oscillation and the maximum rate of change of pressure. Or mathematically

$$\max |\hat{p}| \propto \max \left| \frac{dp}{dt} \right| \quad (4.92)$$

at a particular frequency. The rate of pressure increase is ultimately due to the rate of combustion thus it is reasonable^[9] to suppose that

$$\max \left| \frac{dp}{dt} \right| \propto \max \left(\frac{dQ_i}{dt} \right) \quad (4.93)$$

Or ultimately that

$$KI \propto \max \left(\frac{dQ_i}{dt} \right). \quad (4.94)$$

Combining Eq. 4.90 with Eq. 4.94 The factors that affect the knock intensity may be identified. Under steady-state conditions variations in the fuel mass fraction (w_f) and heating value (Q_{LHV}) are expected to small and they are therefore removed from the proportionality to arrive at

$$KI \propto \max \left(\frac{dw_i}{dt} \cdot m_u \right). \quad (4.95)$$

The experimental data shows that there is little to no correlation between KI and m_u (cf. Figure 4-30). This implies that the intensity of autoignition is not particularly sensitive to the total unburned mass available. If this is the case the m_u term may be dropped from the proportionality, leaving only dw_i/dt . The maximum value of dw_i/dt occurs at t_k , thus substituting Eq. 4.87 into the equation above

$$KI \propto \frac{1}{I_\sigma \sqrt{2\pi}} \left[\frac{1}{\tau_k} \right]. \quad (4.96)$$

In words the result of this mathematical analysis indicates that changes in the knock intensity are driven by changes in the ignition delay at autoignition. This finding suggests that a correlation should exist between KI and $1/\tau_k$.

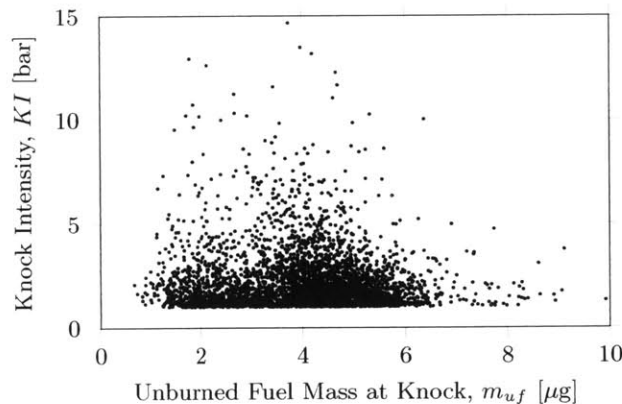


Figure 4-30: The intensity of knock does not appear to be correlated with the available mass of fuel at the inception of autoignition.

If a plot is constructed of the mean knock intensity at each steady state operating point against $1/\tau_k$ the data collapses well to show an apparently exponential increase in mean knock intensity with increasing $1/\tau_k$ (cf. Figure 4-31). Alternatively if the knock intensity and $1/\tau_k$ values of each cycle are computed and the frequency distributions are determined over a range of $1/\tau_k$ values one observes that as $1/\tau_k$ increases the distribution shifts towards higher knock intensities and the length of the distribution tail to the right increases (cf. Figure 4-32). This follows the behavior of a lognormal distribution with an increasing location parameter (μ).

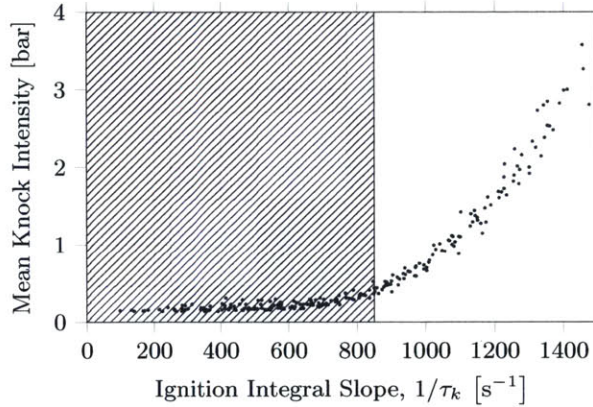


Figure 4-31: The mean knock intensity scales with the ignition integral slope ($1/\tau_k$), the mean knock intensity appears to increase exponentially.

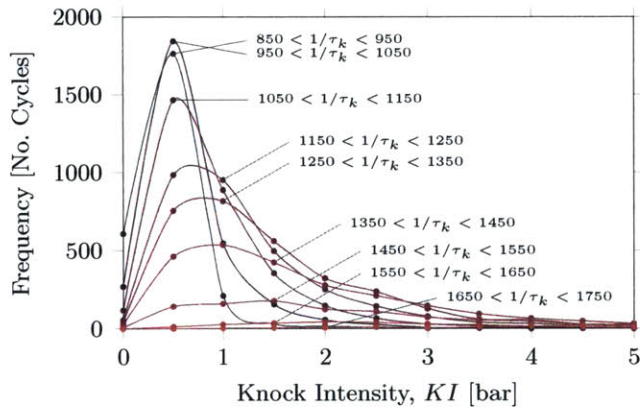


Figure 4-32: Frequency distributions for ranges of $1/\tau_k$. As $1/\tau_k$ increases the center of the distribution moves towards higher knock intensities and the length of the distribution tail to the right is increased. This behavior mirrors the behavior of a lognormal distribution with increasing scale parameter (μ).

Correlating Knock Intensity Distributions

As observed in the previous two sections knock intensity and the ignition delay at knock are strongly correlated and the distribution in knock intensity at steady state is modeled well using a lognormal distribution. Thus it is natural to suspect that the relationship between knock intensity and ignition delay for a single cycle may be reformulated to relate the knock intensity distribution to the ignition

delay at steady state. Such a relationship would allow the distribution of knock intensities to be identified under particular steady state conditions. For each steady state operating point included in the autoignition integral testing of section Sec. 4.2 a best fit lognormal distribution to the knock intensity was computed. Plotting the location parameter (μ) against the mean value of the ignition integral slope at knock ($\text{mean}(1/\tau_k) = 1/\bar{\tau}_k$) illuminates the relationship between these two variables (cf. Figure 4-33). On the left (shaded) side of the plot is an area of constant μ , this corresponds to the baseline noise levels observed during combustion with these operating points exhibiting a very low probability of observing a knocking cycle (cf. Figure 4-34). On the right side of the plot the location parameter appears to increase linearly with $\text{mean}(1/\tau_k)$. In this region there is a moderate to high likelihood that knocking cycles will be observed. At the border between the shaded and unshaded areas lies a transitional region where the probability of observing a knocking cycles is low. Thus to predict the intensity and distribution of knocking cycles it suffices to consider only the unshaded data. A linear function was fit to the data between 800 s^{-1} and 1400 s^{-1} which resulted in the following empirical correlation

$$\mu \left(\frac{1}{\bar{\tau}_k} \right) = 3.64 \times 10^{-3} \left(\frac{1}{\bar{\tau}_k} \right) - 4.15. \quad (4.97)$$

This fit exhibits an R^2 value of 0.98 in the range $(800, 1400)$. The scale parameter can also be broken down into the same knocking and non-knocking regimes (cf. Figure 4-35). On the left, where there are no knocking cycles, the scale parameter is a low consistent value that is indicative of minimal variations in the high frequency pressure fluctuations, these variations are most likely due to acoustic noise created by mechanical components of the engine. In the unshaded area of the plot, where knocking cycles exist, the scale parameter assumes a stable value that is larger than the non-knocking value. This shift reflects a change in the mechanism behind cycle-to-cycle variation in KI , with the shaded side representing variations that are inherent to the engine or sensing system and the unshaded side representing variations that are inherent to the knock intensity. Beyond the transition region between these low and high values a best fit constant of 0.635 was computed,

$$\sigma = 0.635. \quad (4.98)$$

scale parameter data exhibits somewhat more scatter than the location parameter data. Nevertheless the range of scatter in σ only has a small impact on the predicted probability distributions and thus approximating σ as a constant value is deemed a viable simplifying assumption. Using these two empirical fits it is possible to generate a knock intensity probability density function based on a mean value of $1/\tau_k$. The utility of this relationship could be enhanced by demonstrating that the mean ignition integral slope over all experimental cycles ($\text{mean}(1/\tau_k)$) could be replaced by $1/\tau_{k,m}$, the slope of the autoignition integral at knock for a mean cycle. To check if this is the case the slope

of the autoignition integral at knock for a mean cycle was compared to $\text{mean}(1/\tau_k)$. Experimental data indicates that correlation between these two values is reasonable and thus the ignition delay at knock for a mean cycle can be used to estimate the knock intensity distribution at a steady state operating point.

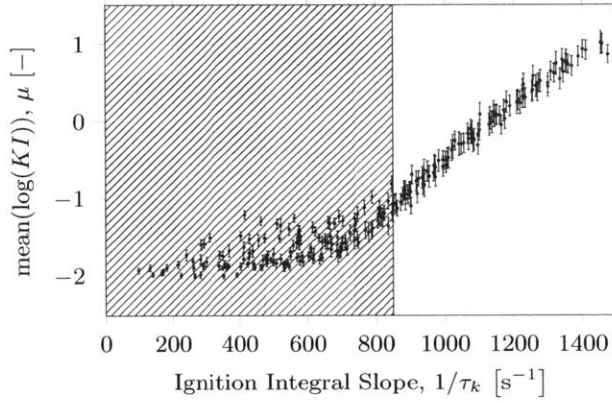


Figure 4-33: Correlation between the ignition integral slope and location parameter is nearly linear for knocking cycles.

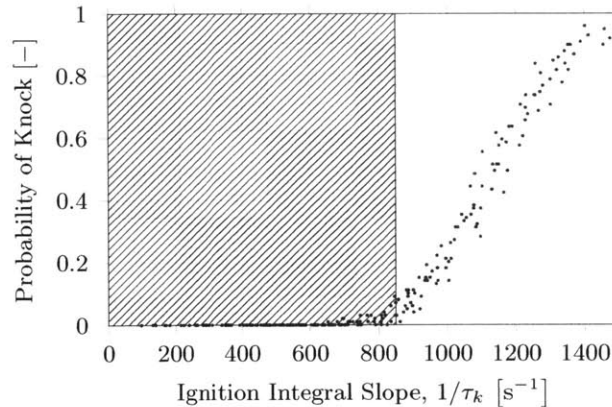


Figure 4-34: Cycles below with an ignition integral slope of below 800s^{-1} are very unlikely to knock, thus the data in this range is of limited use.

Predictive Capability of Statistical Knock Intensity Model

A particularly useful manipulation of the correlations developed for the knock intensity uses the cumulative distribution function of a lognormal distribution to predict the likelihood that a cycle will exceed a specific knock intensity threshold. Using the cumulative distribution function of Eq. 4.80 for a knock intensity threshold KI_t yields

$$F(KI_t, 1/\tau_{k,m}) = \frac{1}{2} \left[1 + \text{erf} \left(\frac{\ln(KI_t) - \mu(1/\tau_{k,m})}{\sigma\sqrt{2}} \right) \right]. \quad (4.99)$$

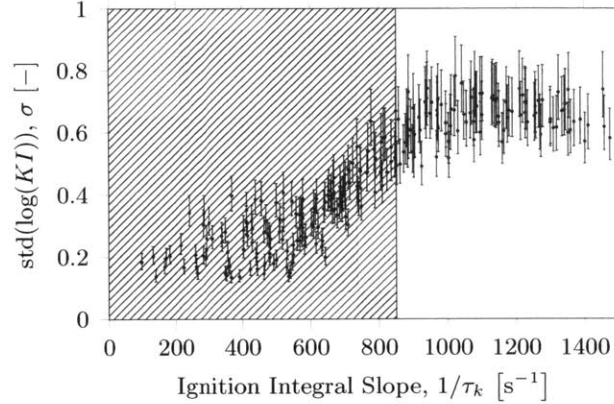


Figure 4-35: The scale parameter is approximately constant for values of the ignition integral slope greater than 800 s^{-1} .

Thus given a mean cycle – from which $\tau_{k,m}$ may be computed – and a threshold knock intensity (KI_t) the probability that a cycle will exceed the threshold is given by

$$p_k(KI_t, 1/\tau_{k,m}) = 1 - F(KI_t, 1/\tau_{k,m}). \quad (4.100)$$

Which may be written without external reference as

$$p_k(KI_t, 1/\tau_{k,m}) = \frac{1}{2} \left[1 - \operatorname{erf} \left(\frac{\ln(KI_t) - \mu(1/\tau_{k,m})}{\sigma\sqrt{2}} \right) \right]. \quad (4.101)$$

This predicted probability may be compared to the observed percentage of cycles that exceed the same threshold at a particular steady state operating condition in a firing engine. If a value of KI_t is selected – take for example $KI_t = 1 \text{ bar}$ – then the probability function p_k has a single unknown, namely $\tau_{k,m}$. Plotting p_k against $1/\tau_{k,m}$ with $KI_t = 1 \text{ bar}$ generates a characteristic sigmoidal shape (cf. Figure 4-36). Layering experimental observations of the percentage of cycles that exceed KI_t over this curve confirms the predicted shape and transition regions agree. A similar construction can be carried out with the threshold increased to 5 bar, which also demonstrates strong agreement with the experimental data (cf. Figure 4-37). The reliability of these knock intensity correlations indicates that a useful measure of knock risk is the slope of the autoignition integral at knock or equivalently, the reciprocal of the ignition delay at knock. The formation of damage metric based on the knock intensity, pressure at knock and temperature at knock would allow the damage potential to be quantified at the stage of idealized cycle analysis. Tuning of engines to function on a damage based knock limit has the potential to improve efficiency and performance on portions of the operating map that have a low probability of producing damaging knock in comparison to the potential changes in efficiency. Stated mathematically opportunities exist to improve efficiency at a low risk where $\frac{\partial \eta}{\partial (1/\tau_k)}$ is large.

By a similar method to the analysis of the cumulative distribution function above an estimate of

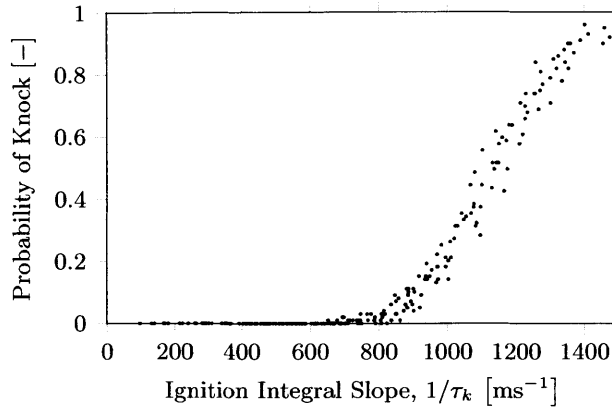


Figure 4-36: The probability that a cycle will exceed 1 bar in knock intensity grows according to the cumulative density function $p_k = 1 - F(1, 1/\tau_{k,m})$.

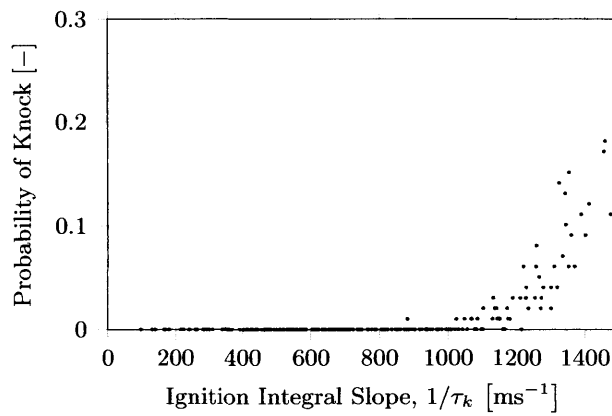


Figure 4-37: Similarly the probability that a cycle will exceed 5 bar in knock intensity is modeled by $p_k = 1 - F(5, 1/\tau_{k,m})$.

the knock intensity probability density may be obtained using Eq. 4.79 in conjunction with Eq. 4.97 and Eq. 4.98 to arrive at

$$f(KI; 1/\tau_{k,m}) = \frac{1}{KI\sigma\sqrt{2\pi}} e^{-\frac{(\ln(KI) - \mu)^2}{2\sigma^2}}, \quad (4.102)$$

which may be compared to a histogram of knock intensity data collected at the same steady state condition. The ability to estimate the probability and intensity of knock based on the mean cycle alone provides a valuable tool for assessing the limits of knock and understanding the parameters that affect its intensity and frequency. Destructive testing has shown that the damage incurred by knock is related to knock intensity and frequency. If such a model was formulated mathematically the damage potential of the predicted distribution could be assessed as a scalar value.

Chapter 5

Summary and Conclusions

The goal of this research effort has been to identify and quantify some of the key factors that contribute to the performance of EGR as a method of improving engine efficiency and knock tolerance, particularly at high loads and low engine speeds. As a critical preliminary step several key features of the behavior of EGR systems under high loads in turbocharged engines were identified. Subsequent to this analysis a new approach to developing knock integral correlations was developed and employed to extend predictions of ignition delay to a range of air-fuel ratios and EGR rates. Finally a statistical model based on cycle-to-cycle variations within the cylinder was developed in order to predict the statistical variation in the intensity of autoignition.

5.1 Pre-Catalyst and Post-Catalyst EGR

An examination of the behavior of alternative EGR installations was performed in which a system was designed and built capable of extracting exhaust gasses from a location either upstream or downstream of the catalyst. A series of tests performed at 0% EGR, i.e. with the EGR valve completely blocked, indicated a substantial change in the operating characteristics of the engine, specifically in burn duration, efficiency and manifold pressure when compared to the original engine. These changes were traced to breathing modifications due to alteration of blowdown, turbocharger and scavenging characteristics by the introduction of the EGR loop volume. The effects were different when the EGR loop originated from before or after the catalyst. Due to the feedback mechanism introduced by the turbocharger recovering identical conditions with different EGR installations presents a formidable challenge not addressed in this work. Instead incremental changes in efficiency and knock tolerance from the zero EGR case were compared across alternative EGR installations.

No appreciable difference in knock tolerance was observed between pre-catalyst and post-catalyst EGR installations with both improving efficiency predominantly through knock abatement at low engine speeds. To confirm this negative finding gaseous addition experiments were performed in

which a portion of the fuel was replaced with a gaseous fuel known to exist in pre-catalyst EGR. The effects of hydrogen, carbon monoxide and nitric oxide were studied and of the three only carbon monoxide exhibited the potential to improve engine performance mainly by decreasing burn duration. This effect however is very small, with a maximum change in burn duration of under 1° for the highest levels of carbon monoxide attainable using EGR unless the engine is operated very rich, in which case the excess fuel will dominate the knock tolerance improvements. Nitric oxide was observed to have a mildly detrimental effect on autoignition tolerance, reducing the knock limited CA50 by approximately 1° under adverse conditions. In order to observe appreciable changes in engine behavior the amounts of these three gasses required were well in excess of the amounts realizable with EGR.

5.2 Knock Modeling and Prediction

A thorough examination of the knock integral approach to autoignition prediction in engines was performed including a sensitivity analysis which identified the criticality of minimizing uncertainty in the ignition delay near the conditions of autoignition – when the ignition delay τ is small. A weighting scheme was developed by which experimental ignition delay data may be weighted to reduce errors in autoignition prediction. This analysis indicates that the feature most critical to accurate autoignition prediction in engines is a correlation that accurately identifies the ignition delay at the pressures and temperatures that generally exist immediately prior to autoignition within a particular engine. The more accurate this prediction is the less important errors at other ignition delays become.

To take advantage of this finding an experimental approach was developed that relies on measurements obtained during the operation of an engine. First a suitable form of the ignition delay correlation is selected. This work has demonstrated that either

$$\tau(p, T) = ap^{-b}e^{\frac{c}{T}} \quad (5.1)$$

or

$$\tau(p, T) = a \left(\frac{p}{T} \right)^{-b} e^{\frac{c}{T}} \quad (5.2)$$

work equally well for this purpose. Next a reliable method of identifying the start of autoignition (t_k) during a firing cycle was established. The method developed is based on the identification of the start of high frequency pressure oscillations and is referred to as the oscillatory step detection (OSD) approach. With these two prerequisites in place and a method of either measuring or estimating the pressures and temperatures of the end gas a minimum of three knocking cycles at different conditions are required to identify the three unknowns in one of the equations above using the autoignition

integral

$$1 = \int_{t_0}^{t_k} \frac{1}{\tau(p, T)} dt. \quad (5.3)$$

Instead of using the minimum number of knocking cycles many knocking cycles were used over a wide range of conditions and the coefficients of the ignition delay correlation were optimized using nonlinear optimization tools to minimize the RMS error between the predicted and observed time of autoignition. This method tends to adjust the ignition delay correlation so developed for the highest level of autoignition prediction accuracy.

The optimization method used to extend the ignition delay to account for dilution of the charge with burned gasses which were included as the parameter $w_d = w_r + w_{egr}$ which represents the mass fraction of unburned gases in the charge. Under stoichiometric conditions the ignition delay correlations

$$\tau(p, T, w_d) = 0.0131(1 - w_d)^{-1.14} p^{-1.72} e^{\frac{3940}{T}} \quad [\text{s}] \quad (5.4)$$

or alternatively

$$\tau(p, T, w_d) = 2.71 \times 10^{-8}(1 - w_d)^{-0.618} \left(\frac{p}{T}\right)^{-1.73} e^{\frac{5190}{T}} \quad [\text{s}] \quad (5.5)$$

where p is cylinder pressure in bar and T is end gas temperature in K both predict the autoignition behavior to within $\pm 1^\circ$ of crank rotation under a wide range of operating speeds, loads and diluent fractions.

Next the ignition delay correlation was extended to non-stoichiometric conditions in conjunction with dilution. It was shown that the empirical correlation

$$\tau(p, T, w_d) = \begin{cases} 2.71 \times 10^{-8}(1 - w_d - 0.95|\delta|)^{-0.618} \left(\frac{p}{T}\right)^{-1.73} e^{\frac{5190}{T}}, & \text{if } \lambda < 1 \\ 2.71 \times 10^{-8}(1 - w_d(1 - \delta) - 0.95|\delta|)^{-0.618} \left(\frac{p}{T}\right)^{-1.73} e^{\frac{5190}{T}}, & \text{if } \lambda \geq 1 \end{cases} \quad (5.6)$$

where

$$\delta \equiv \frac{\lambda - 1}{\lambda + \left(\frac{m_f}{m_a}\right)_s}, \quad (5.7)$$

provides accurate prediction results across various air-fuel ratios.

The next aspect of autoignition examined was the statistical variation in the intensity of autoignition. It was shown mathematically that if one assumes that local variations in composition and temperature are considered to result in a local value of the autoignition integral and these local autoignition integral values are normally distributed that the maximum rate at which regions are driven to autoignite depends on the ratio $1/\tau_k$ where τ_k is the mean ignition delay at knock. Plotting many parameters against $1/\tau_k$ collapses the data considerably and this feature was used to create a statistical model of variations in knock intensity (KI) which is defined as the maximum magnitude of high frequency pressure oscillations. At steady state the distribution of KI values is modeled well

by a lognormal distribution and the parameters of these distributions (μ and σ) correlate with $1/\tau_k$. It was shown that over a range of conditions the location parameter is approximately

$$\mu\left(\frac{1}{\tau_k}\right) = 3.64 \times 10^{-3} \left(\frac{1}{\bar{\tau}_k}\right) - 4.15, \quad (5.8)$$

and the scale parameter is nearly constant at

$$\sigma = 0.635. \quad (5.9)$$

These two empirical correlations may be used to predict – among other things – the probability that a particular threshold knock intensity (KI_t) will be exceeded which is given by

$$p_k(KI_t, 1/\tau_k) = \frac{1}{2} \left[1 - \text{erf} \left(\frac{\ln(KI_t) - \mu(1/\tau_k)}{\sigma\sqrt{2}} \right) \right]. \quad (5.10)$$

Such a model has wide utility as a method of estimating the likelihood and magnitude of knock based on the thermodynamic state of the end gas when the autoignition integral exceeds unity.

5.3 Recommendations for Future Work

A considerable number of the difficulties encountered in the comparison of pre-catalyst to post-catalyst sourced EGR could be avoided if an EGR loop was developed with the following features:

- An externally driven supercharger instead of standard turbocharger to avoid feedback of exhaust changes to intake state
- A *hot-side* EGR valve that is located upstream of any tubing or EGR cooler
- A means of adjusting valve timing to maintain a constant fraction of trapped residuals and ensure scavenging is avoided

With these three features in place differences in engine behavior due to the configuration of the EGR system should be largely eliminated providing an equal basis on which pre-catalyst and post-catalyst EGR may be compared over a wide range of conditions. This would allow any of the more minute difference between pre-catalyst and post-catalyst EGR to be identified.

The ignition delay correlation approach developed here provides a relatively low-complexity method of identifying an ignition delay correlation for a particular engine-fuel combination. In order to enhance the accuracy and generality of the ignition delay correlation it is necessary to conduct testing in a range of engines that operate with different end gas conditions. This generality may come at the expense of accuracy within an individual engine, however the uncertainty analysis indicates that an engine-specific correction factor, which multiplies the entire ignition delay expression

may be effectively used to improve autoignition prediction accuracy. Ultimately the combination of a fuel-specific ignition delay correlation and engine (and possibly fuel) specific correction factors may prove a useful tool for engine development and modeling.

In the development of the statistical model of autoignition it was identified that opportunities exist to improve efficiency with the lowest risk of autoignition damage where $\frac{\partial \eta_f}{\partial (1/\tau_k)}$. A simulation study of end gas conditions and the autoignition integral may illuminate regions that offer favorable a favorable risk-benefit trade off as well as methods of increasing this ratio where knock limits are frequently encountered.

Bibliography

- [1] Abd-Alla, G. H. "Using Exhaust Gas Recirculation in Internal Combustion Engines: a Review". *Energy Conversion and Management* 43.8 (May 2002), pp. 1027–1042. DOI: 10.1016/S0196-8904(01)00091-7.
- [2] Alger, T., Mangold, B., Roberts, C., and Gingrich, J. *The Interaction of Fuel Anti-Knock Index and Cooled EGR on Engine Performance and Efficiency*. SAE Technical Report 2012-01-1149. Warrendale, PA, Apr. 2012. DOI: 10.4271/2012-01-1149.
- [3] Alger, T., Chauvet, T., and Dimitrova, Z. *Synergies between High EGR Operation and GDI Systems*. SAE Technical Report 2008-01-0134. Warrendale, PA, Apr. 2008. DOI: 10.4271/2008-01-0134.
- [4] Alger, T., Gingrich, J., and Mangold, B. *The Effect of Hydrogen Enrichment on EGR Tolerance in Spark Ignited Engines*. SAE Technical Report 2007-01-0475. Warrendale, PA, Apr. 2007. DOI: 10.4271/2007-01-0475.
- [5] Alger, T. and Mangold, B. *Dedicated EGR: A New Concept in High Efficiency Engines*. SAE Technical Report 2009-01-0694. Warrendale, PA, Apr. 2009. DOI: 10.4271/2009-01-0694.
- [6] Andrews, L. C. *Special Functions of Mathematics for Engineers*. Oxford: Oxford University Press, 1998. ISBN: 978-0819426161.
- [7] Anzilotti, W. F. and Tomsic, V. J. "Combustion of hydrogen and carbon monoxide as related to knock". *Symposium (International) on Combustion* 5.1 (Jan. 1955), pp. 356–366. DOI: 10.1016/S0082-0784(55)80048-3.
- [8] Ayala, F. A., Gerty, M. D., and Heywood, J. B. *Effects of Combustion Phasing, Relative Air-fuel Ratio, Compression Ratio, and Load on SI Engine Efficiency*. SAE Technical Report 2006-01-0229. Warrendale, PA, Apr. 2006. DOI: 10.4271/2006-01-0229.
- [9] Bradley, D. "Hot Spots and Gasoline Engine Knock". *Journal of the Chemical Society, Faraday Transactions* 92.16 (1996), p. 2959. DOI: 10.1039/ft9969202959.
- [10] Brecq, G. and Le Corre, O. *Modeling of In-cylinder Pressure Oscillations under Knocking Conditions: Introduction to Pressure Envelope Curve*. SAE Technical Report 2005-01-1126. Warrendale, PA, Apr. 2005. DOI: 10.4271/2005-01-1126.
- [11] Brunt, M. F. J., Huang, C. Q., Rai, H. S., and Cole, A. C. *An Improved Approach to Saving Cylinder Pressure Data from Steady-State Dynamometer Measurements*. SAE Technical Report 2000-01-1211. Warrendale, PA, Mar. 2000. DOI: 10.4271/2000-01-1211.
- [12] Buda, F., Bounaceur, R., Warth, V., Glaude, P. A., Fournet, R., and Battin-Leclerc, F. "Progress Toward a Unified Detailed Kinetic Model for the Autoignition of Alkanes From C4 to C10 Between 600 and 1200 K". *Combustion and Flame* 142.1-2 (July 2005), pp. 170–186. DOI: 10.1016/j.combustflame.2005.03.005.
- [13] Campau, R. M. and Neerman, J. C. *Continuous Mass Spectrometric Determination of Nitric Oxide in Automotive Exhaust*. SAE Technical Report 660116. Warrendale, PA, Feb. 1966. DOI: 10.4271/660116.
- [14] Cavina, N., Corti, E., Minelli, G., Moro, D., and Solieri, L. *Knock Indexes Normalization Methodologies*. SAE Technical Report 2006-01-2998. Warrendale, PA, Sept. 2006. DOI: 10.4271/2006-01-2998.

- [15] Cox, R. A. and Cole, J. A. “Chemical aspects of the autoignition of hydrocarbon-air mixtures”. *Combustion and Flame* 60.2 (May 1985), pp. 109–123. DOI: 10.1016/0010-2180(85)90001-X.
- [16] Davis, R. S. and Patterson, G. J. *Cylinder Pressure Data Quality Checks and Procedures to Maximize Data Accuracy*. SAE Technical Report 2006-01-1346. Warrendale, PA, Apr. 2006. DOI: 10.4271/2006-01-1346.
- [17] Douaud, A. M. and Eyzat, P. *Four-Octane-Number Method for Predicting the Anti-Knock Behavior of Fuels and Engines*. SAE Technical Report 780080. Warrendale, PA, Feb. 1978. DOI: 10.4271/780080.
- [18] Duchaussoy, Y., Lefebvre, A., and Bonetto, R. *Dilution Interest on Turbocharged SI Engine Combustion*. SAE Technical Report 2003-01-0629. Warrendale, PA, Mar. 2003. DOI: 10.4271/2003-01-0629.
- [19] Einecke, S., Schulz, C., and Sick, V. “Measurement of temperature, fuel concentration and equivalence ratio fields using tracer LiF in IC engine combustion”. *Applied Physics B* 71.5 (Apr. 2014), pp. 717–723. DOI: 10.1007/s003400000383.
- [20] Elmqvist, C., Lindström, F., Ångström, H.-E., Grandin, B., and Kalghatgi, G. *Optimizing Engine Concepts by Using a Simple Model for Knock Prediction*. SAE Technical Report. Warrendale, PA, Oct. 2003. DOI: 10.4271/2003-01-3123.
- [21] Emanuel, N. M. and Gagarina, A. B. “Critical Phenomena in Chain Reactions with Degenerate Branching”. *Russian Chemical Reviews* 35.4 (Apr. 1966), pp. 260–278. DOI: 10.1070/RC1966v035n04ABEH001461.
- [22] Fieweger, K., Blumenthal, R., and Adomeit, G. “Self-Ignition of S.I. Engine Model Fuels: a Shock Tube Investigation at High Pressure”. *Combustion and Flame* 109.4 (June 1997), pp. 599–619. DOI: 10.1016/S0010-2180(97)00049-7.
- [23] Grandin, B., Ångström, H.-E., Stålhammar, P., and Olofsson, E. *Knock Suppression in a Turbocharged SI Engine by Using Cooled EGR*. SAE Technical Report 982476. Warrendale, PA, Oct. 1998. DOI: 10.4271/982476.
- [24] Grandin, B., Denbratt, I., Bood, J., Brackmann, C., and Bengtsson, P.-E. *The Effect of Knock on the Heat Transfer in an SI Engine: Thermal Boundary Layer Investigation using CARS Temperature Measurements and Heat Flux Measurements*. SAE Technical Report. Warrendale, PA, Oct. 2000. DOI: 10.4271/2000-01-2831.
- [25] Guibet, J.-C. and Faure-Birchem, E. *Fuels and Engines: Technology, Energy, Environment*. Vol. 1. Éditions Technip, Jan. 1999. ISBN: 978-2710807537.
- [26] Halstead, M. P., Kirsch, L. J., and Quinn, C. P. “The Autoignition of Hydrocarbon Fuels at High Temperatures and Pressures—Fitting of a Mathematical Model”. *Combustion and Flame* 30 (Jan. 1977), pp. 45–60. DOI: 10.1016/0010-2180(77)90050-5.
- [27] Hamamoto, Y., Tomita, E., and Jiang, D. “Temperature Measurement of End Gas Under Knocking Condition in a Spark-Ignition Engine by Laser Interferometry”. *JSAE Review* 15.2 (Apr. 1994), pp. 117–122.
- [28] He, X., Donovan, M. T., Zigler, B. T., Palmer, T. R., Walton, S. M., Wooldridge, M. S., and Atreya, A. “An experimental and modeling study of iso-octane ignition delay times under homogeneous charge compression ignition conditions”. *Combustion and Flame* 142.3 (Aug. 2005), pp. 266–275. DOI: 10.1016/j.combustflame.2005.02.014.
- [29] Heywood, J. B. *Internal Combustion Engine Fundamentals*. McGraw-Hill Series in Mechanical Engineering. New York: McGraw-Hill, Jan. 1988. ISBN: 978-0070286375.
- [30] Hoepke, B., Jannsen, S., Kasseris, E., and Cheng, W. K. “EGR Effects on Boosted SI Engine Operation and Knock Integral Correlation”. *SAE International Journal of Engines* 5.2 (Apr. 2012), pp. 547–559. DOI: 10.4271/2012-01-0707.
- [31] Hu, H. and Keck, J. *Autoignition of Adiabatically Compressed Combustible Gas Mixtures*. SAE Technical Report 872110. Warrendale, PA, Nov. 1987. DOI: 10.4271/872110.

- [32] Ivani,, Ayala, F., Goldwitz, J., and Heywood, J. B. *Effects of Hydrogen Enhancement on Efficiency and NO_x Emissions of Lean and EGR-Diluted Mixtures in a SI Engine*. SAE Technical Report 2005-01-0253. Warrendale, PA, Apr. 2005. DOI: 10.4271/2005-01-0253.
- [33] Johansson, B. *Influence of the Velocity Near the Spark Plug on Early Flame Development*. SAE Technical Report 930481. Warrendale, PA, Mar. 1993. DOI: 10.4271/930481.
- [34] Kawabata, Y., Sakonji, T., and Amano, T. *The Effect of NO_x on Knock in Spark-ignition Engines*. SAE Technical Report 1999-01-0572. Warrendale, PA, Mar. 1999. DOI: 10.4271/1999-01-0572.
- [35] Kawahara, N., Tomita, E., Ichimiya, M., Takasu, K., Tsuchida, N., and Goto, K. *Transient Temperature Measurement of Unburned Gas in an Engine Cylinder Using Laser Interferometry with a Fiber-Optic Sensor*. SAE Technical Report 2003-01-1799. Warrendale, PA, May 2003. DOI: 10.4271/2003-01-1799.
- [36] Kawahara, N., Tomita, E., and Sakata, Y. "Auto-Ignited Kernels During Knocking Combustion in a Spark-Ignition Engine". *Proceedings of the Combustion Institute* 31.2 (Jan. 2007), pp. 2999–3006. DOI: 10.1016/j.proci.2006.07.210.
- [37] Keck, J. C., Heywood, J. B., and Noske, G. *Early Flame Development and Burning Rates in Spark Ignition Engines and Their Cyclic Variability*. SAE Technical Report 870164. Warrendale, PA, Feb. 1987. DOI: 10.4271/870164.
- [38] König, G., Maly, R. R., Bradley, D., Lau, A. K. C., and Sheppard, C. G. W. *Role of Exothermic Centres on Knock Initiation and Knock Damage*. SAE Technical Report 902136. Warrendale, PA, Oct. 1990. DOI: 10.4271/902136.
- [39] KONO, M., SHIGA, S., KUMAGAI, S., and IINUMA, K. "Thermodynamic and Experimental Determinations of Knock Intensity by Using a Spark-Ignited Rapid Compression Machine". *Combustion and Flame* 54.1-3 (Dec. 1983), pp. 33–47. DOI: 10.1016/0010-2180(83)90020-2.
- [40] Kuratle, R. H. and Märki, B. *Influencing Parameters and Error Sources During Indication on Internal Combustion Engines*. SAE Technical Report 920233. Warrendale, PA, Feb. 1992. DOI: 10.4271/920233.
- [41] Leduc, P., Dubar, B., Ranini, A., and Monnier, G. "Downsizing of Gasoline Engine: an Efficient Way to Reduce CO₂ Emissions". *Oil & Gas Science and Technology* 58.1 (Jan. 2003), pp. 115–127. DOI: 10.2516/ogst:2003008.
- [42] Lee, J.-H., Hwang, S.-H., Lim, J.-S., Jeon, D.-C., and Cho, Y.-S. *A New Knock-Detection Method using Cylinder Pressure, Block Vibration and Sound Pressure Signals from a SI Engine*. SAE Technical Report 981436. Warrendale, PA, May 1998. DOI: 10.4271/981436.
- [43] Lezius, U., Schultalbers, M., Drewelow, W., and Lampe, B. "Improvements in knock control". *Control & Automation, 2007. MED '07. Mediterranean Conference on*. 2007, pp. 1–5. DOI: 10.1109/MED.2007.4433682.
- [44] Livengood, J. C. and Wu, P. C. "Correlation of autoignition phenomena in internal combustion engines and rapid compression machines". *Symposium (International) on Combustion* 5.1 (Jan. 1955), pp. 347–356. DOI: 10.1016/S0082-0784(55)80047-1.
- [45] Maly, R. R. "State of the art and future needs in S.I. engine combustion". *Symposium (International) on Combustion* 25.1 (Jan. 1994), pp. 111–124. DOI: 10.1016/S0082-0784(06)80635-1.
- [46] Naber, J., Blough, J. R., Frankowski, D., Goble, M., and Szpytman, J. E. *Analysis of Combustion Knock Metrics in Spark-Ignition Engines*. SAE Technical Report 2006-01-0400. Warrendale, PA, Apr. 2006. DOI: 10.4271/2006-01-0400.
- [47] Nates, R. J. and Yates, A. D. B. *Knock Damage Mechanisms in Spark-Ignition Engines*. SAE Technical Report 942064. Warrendale, PA, Oct. 1994. DOI: 10.4271/942064.
- [48] Pan, J., Sheppard, C. G. W., Tindall, A., Berzins, M., Pennington, S. V., and Ware, J. M. *End Gas Inhomogeneity, Autoignition and Knock*. SAE Technical Report 982616. Warrendale, PA, Oct. 1998. DOI: 10.4271/982616.

- [49] Rai, H. S., Brunt, M. F. J., and Loader, C. P. *Quantification and Reduction of IMEP Errors Resulting from Pressure Transducer Thermal Shock in an S.I. Engine*. SAE Technical Report 1999-01-1329. Warrendale, PA, Mar. 1999. DOI: 10.4271/1999-01-1329.
- [50] Ranini, A. and Monnier, G. *Turbocharging a Gasoline Direct Injection Engine*. SAE Technical Report 2001-01-0736. Warrendale, PA, Mar. 2001. DOI: 10.4271/2001-01-0736.
- [51] Rassweiler, G. M. and Withrow, L. *Motion Pictures of Engine Flames Correlated with Pressure Cards*. SAE Technical Report 380139. Warrendale, PA, Jan. 1938. DOI: 10.4271/380139.
- [52] Roth, D. B., Keller, P., and Becker, M. *Requirements of External EGR Systems for Dual Cam Phaser Turbo GDI Engines*. SAE Technical Report 2010-01-0588. Warrendale, PA, Apr. 2010. DOI: 10.4271/2010-01-0588.
- [53] Sazhina, E. M., Sazhin, S. S., Heikal, M. R., and Marooney, C. J. “The Shell autoignition model: applications to gasoline and diesel fuels”. *Fuel* 78.4 (Mar. 1999), pp. 389–401. DOI: 10.1016/S0016-2361(98)00167-7.
- [54] Shelef, M. and Gandhi, H. S. “Ammonia Formation in Catalytic Reduction of Nitric Oxide by Molecular Hydrogen. II. Noble Metal Catalysts”. *Industrial & Engineering Chemistry Product Research and Development* 11.4 (Dec. 1972), pp. 393–396. DOI: 10.1021/i360044a006.
- [55] Smith, J. M., Simmie, J. M., and Curran, H. J. “Autoignition of heptanes; experiments and modeling”. *International Journal of Chemical Kinetics* 37.12 (2005), pp. 728–736. DOI: 10.1002/kin.20120.
- [56] Soltis, D. A. *Evaluation of Cylinder Pressure Transducer Accuracy based upon Mounting Style, Heat Shields, and Watercooling*. SAE Technical Report 2005-01-3750. Warrendale, PA, Oct. 2005. DOI: 10.4271/2005-01-3750.
- [57] Tanaka, S., Ayala, F., and Keck, J. C. “A Reduced Chemical Kinetic Model for HCCI Combustion of Primary Reference Fuels in a Rapid Compression Machine”. *Combustion and Flame* 133.4 (June 2003), pp. 467–481. DOI: 10.1016/S0010-2180(03)00057-9.
- [58] Vermeer, D. J., Meyer, J. W., and Oppenheim, A. K. “Auto-Ignition of Hydrocarbons Behind Reflected Shock Waves”. *Combustion and Flame* 18.3 (June 1972), pp. 327–336. DOI: 10.1016/S0010-2180(72)80183-4.
- [59] Yates, A. D. B., Swarts, A., and Viljoen, C. L. *Correlating Auto-Ignition Delays And Knock-Limited Spark-Advance Data For Different Types Of Fuel*. SAE Technical Report 2005-01-2083. Warrendale, PA, May 2005. DOI: 10.4271/2005-01-2083.
- [60] Zaccardi, J.-M., Duval, L., and Pagot, A. *Development of Specific Tools for Analysis and Quantification of Pre-ignition in a Boosted SI Engine*. SAE Technical Report 2009-01-1795. Warrendale, PA, June 2009. DOI: 10.4271/2009-01-1795.
- [61] Zhen, X., Wang, Y., Xu, S., Zhu, Y., Tao, C., Xu, T., and Song, M. “The Engine Knock Analysis – an Overview”. *Applied Energy* 92 (Apr. 2012), pp. 628–636. DOI: 10.1016/j.apenergy.2011.11.079.

Acronyms

BDC bottom dead center. 40, 143

CA50 the crank angle of fifty percent heat release. 11–13, 16, 17, 57–61, 63–73, 100, 102, 111, 112, 114, 126, 143

CAFE corporate average fuel economy. 22, 143

COV coefficient of variation. 61, 143

DAQ data acquisition system. 43, 143

ECM engine control module. 10, 33–35, 37, 42, 43, 45, 143

EGR exhaust gas recirculation. 3, 7, 10–14, 19, 28, 29, 31, 33, 38, 39, 41–43, 47, 50–74, 89, 90, 92, 96, 97, 100, 103, 104, 107, 108, 125, 126, 128, 143

ETC exothermic center. 9, 29, 30, 143

GIMEP gross indicated mean effective pressure. 12, 13, 58, 60, 61, 63–69, 100, 143

IID inferred ignition delay. 90, 92, 96, 97, 143

IMPO integral of the modulus of pressure oscillations. 94, 143

IVC intake valve closing. 25, 62, 110, 143

LIF laser induced fluorescence. 29, 115, 143

MBT maximum brake torque. 12, 13, 16, 60, 61, 63, 65–67, 69, 71, 102, 143

MEP mean effective pressure. 43, 44, 143

MON motor octane number. 25, 35, 143

NDIR nondispersive infrared. 38, 39, 44, 45, 143

NIMEP net indicated mean effective pressure. 45, 143

NVH noise, vibration and harshness. 112, 143

OSD oscillatory step detection. 93–97, 126, 143

PRF primary reference fuel. 14, 24, 25, 35, 75–79, 84, 143

RCM rapid compression machine. 14, 26, 29, 31, 75, 76, 78–80, 87, 90, 143

RMS root mean squared. 94, 96, 98, 127, 143

RON research octane number. 25, 35, 143

TDC top dead center. 40, 41, 94, 115, 143

TEL tetraethyl lead. 23, 143

Appendix A

Fuel Properties

The fuel used in the experimental testing presented in this work was Haltermann HF0437 Tier III reference gasoline. The test specifications of this fuel follow.

PRODUCT:

**EPA TIER II EEE
FEDERAL REGISTER**

Batch No.: AH0321LT20

PRODUCT CODE:

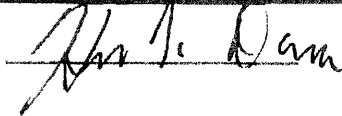
HF0437

Tank No.: 106

Date: 8/9/2012

TEST	METHOD	UNITS	HALTERMANN Specs			RESULTS
			MIN	TARGET	MAX	
Distillation - IBP	ASTM D86	°F	75		95	86
5%		°F				109
10%		°F	120		135	125
20%		°F				149
30%		°F				175
40%		°F				204
50%		°F	200		230	223
60%		°F				234
70%		°F				244
80%		°F				264
90%		°F	305		325	320
95%		°F				344
Distillation - EP		°F			415	411
Recovery		vol %		Report		96.9
Residue		vol %		Report		1.1
Loss		vol %		Report		2.0
Gravity	ASTM D4052	°API	58.7		61.2	59.0
Density	ASTM D4052	kg/l	0.734		0.744	0.743
Reid Vapor Pressure	ASTM D5191	psi	8.7		9.2	9.1
Carbon	ASTM D3343	wt fraction		Report		0.8647
Carbon	ASTM E191	wt fraction		Report		0.8633
Hydrogen	ASTM E191	wt fraction		Report		0.1339
Hydrogen/Carbon ratio	ASTM E191	mole/mole		Report		1.848
Stoichiometric Air/Fuel Ratio				Report		14.581
Oxygen	ASTM D4815	wt %			0.05	None Detected
Sulfur	ASTM D5453	wt %	0.0025		0.0035	0.0029
Lead	ASTM D3237	g/gal			0.01	None Detected
Phosphorous	ASTM D3231	g/gal			0.005	None Detected
Silicon	ASTM 5184	mg/kg			4	1.0
Composition, aromatics	ASTM D1319	vol %			35	28
Composition, olefins	ASTM D1319	vol %			10	1
Composition, saturates	ASTM D1319	vol %		Report		71
Particulate matter	ASTM D5452	mg/l			1	0.7
Oxidation Stability	ASTM D525	minutes	240			1000+
Copper Corrosion	ASTM D130				1	1a
Gum content, washed	ASTM D381	mg/100mls			5	<0.5
Fuel Economy Numerator/C Density	ASTM E191		2401		2441	2429
C Factor	ASTM E191			Report		0.9994
Research Octane Number	ASTM D2699		96.0			96.5
Motor Octane Number	ASTM D2700			Report		88.4
Sensitivity			7.5			8.1
Net Heating Value, btu/lb	ASTM D3338	btu/lb		Report		18489
Net Heating Value, btu/lb	ASTM D240	btu/lb		Report		18492
Color	VISUAL			Report		Undyed

APPROVED BY:



Appendix B

Selected Matlab Code

code/lvb_readarr.m

```
1 function arrout = lvb_readarr(fid,ndim,readfcn)
2 %%%%%%%%%%%%%%%%%%%%%%%%%%%%%%%%%%%%%%
3 %                                     %
4 %   lvb_readarr - read an array from a labview formatted binary file    %
5 %                                     %
6 %%%%%%%%%%%%%%%%%%%%%%%%%%%%%%%%%%%%%%
7 %
8 % lvb_readarr - version 0.9 - Jacob E. McKenzie - modified: 01/04/14
9 %
10 % inputs:
11 % - fid      [int]    : file identifier of binary file saved by labview
12 % - ndim     [int]    : number of array dimensions (2 or 3)
13 % - readfcn  [handle] : function handle of element read function
14 %
15 % output:
16 % - arrout [array] : cell or array of values read from binary file
17 %
18 % notes:
19 % - Current version contains no error checking.
20 % - In order to use this code the number of dimensions and data type
21 %   of the array must be known and the file must be cued up to the
22 %   beginning of the array descriptor.
23 %
24 % example:
25 % X = lvb_readarr(4,2,$lvb_readdbl);
26 % This attempts to read a two dimensional matrix from the file with an
27 % identifier of 4. Each element is read using lvb_readdbl function.
28 %
29 %%%%%%%%%%%%%%%%%%%%%%%%%%%%%%%%%%%%%%
30 %
31 % read the array size descriptor (number of elements in each dim)
32 aels = vrev(fread(fid,ndim,'int32>>double'))';
33 %
34 % read elements and place elements in either a cell or an array
35 arrout = readfcn(fid,prod(aels));
36 %
37 % permute the array such that it matches the labview orientation
38 if ndim == 2
39     arrout = reshape(arrout,aels);
40     arrout = permute(arrout,[2,1]);
41 else
42     if ndim == 3
43         arrout = reshape(arrout,aels);
```

```

44     arrout = permute(arrout,[2,1,3]);
45
46 end
47
48 end

```

code/lvb_readdbl.m

```

1 function dblout = lvb_readdbl(fid,n)
2 %%%%%%%%%%%%%%%%%%%%%%%%%%%%%%%%%%%%%%
3 %                                     %
4 %   lvb_readdbl - read a double from a labview formatted binary file %
5 %                                     %
6 %%%%%%%%%%%%%%%%%%%%%%%%%%%%%%%%%%%%%%
7 %
8 % lvb_readdbl - version 1.0 - Jacob E. McKenzie - modified: 01/04/14
9 %
10 % inputs:
11 % - fid      [int]    : file identifier for binary file saved by labview
12 % - n       [int]    : number of double precision floats to read
13 %
14 % output:
15 % - dblout [array] : 1 by n vector of doubles read from file
16 %
17 % notes:
18 % - Current version contains no error checking.
19 %
20 % example:
21 % A = lvb_readdbl(4,8);
22 % This attempts to read 8 double precision floats from the labview
23 % formatted binary file with a file identifier of 4. The values are
24 % returned as a 1 by 8 vector.
25 %
26 %%%%%%%%%%%%%%%%%%%%%%%%%%%%%%%%%%%%%%
27
28 dblout = fread(fid,n,'*double');
29
30 end

```

code/lvb_readnotes.m

```

1 function cslout = lvb_readnotes(fid,n)
2 %%%%%%%%%%%%%%%%%%%%%%%%%%%%%%%%%%%%%%
3 %                                     %
4 %   lvb_readnotes - read notes cluster from labview formatted binary file %
5 %                                     %
6 %%%%%%%%%%%%%%%%%%%%%%%%%%%%%%%%%%%%%%
7 %
8 % lvb_readnotes - version 1.0 - Jacob E. McKenzie - modified: 01/04/14
9 %
10 % inputs:
11 % - fid      [int]    : file identifier for binary file saved by labview
12 % - n       [int]    : number of notes to read
13 %
14 % output:
15 % - cslout [cell] : n by 5 cluster of notes about engine data
16 %
17 % notes:
18 % - Current version contains no error checking.
19 % - Each note consists of three strings followed by a double and a final
20 %   string. In order these entries represent:
21 %     1) A descriptive name of the note
22 %     2) A note name that qualifies as a matlab variable
23 %     3) A description of the note, or the notes content if it is a text note
24 %     4) A double precision note value

```

```

25 %      5) A string describing the units of the numeric value (4)
26 %
27 % example:
28 % C = lvb_readnotes(4,8);
29 %   This attempts to read 8 notes from a data file that has a file
30 %   identifier of 4. In this case C is an 8 by 5 cluster.
31 %
32 %%%%%%%%%%%%%%%%%%%%%%%%%%%%%%%%%%%%%%
33 %
34 clsout{m,5} = [];
35 for i = 1:n
36     clsout(i,1:3) = lvb_readstr(fid,3);
37     clsout(i,4)   = lvb_readdbl(fid,1);
38     clsout(i,5)   = lvb_readstr(fid,1);
39 end
40
41 end

```

code/lvb_readstr.m

```

1 function strout = lvb_readstr(fid,n)
2 %%%%%%%%%%%%%%%%%%%%%%%%%%%%%%%%%%%%%%
3 %
4 %   lvb_readstr - read a string from a labview formatted binary file %
5 %
6 %%%%%%%%%%%%%%%%%%%%%%%%%%%%%%%%%%%%%%
7 %
8 % lvb_readstr - version 1.0 - Jacob E. McKenzie - modified: 01/04/14
9 %
10 % inputs:
11 % - fid    [int] : file identifier for binary file saved by labview
12 % - n      [int] : number of strings to read
13 %
14 % output:
15 % - strout [array] : 1 by n cell array of strings
16 %
17 % notes:
18 % - Current version contains no error checking.
19 %
20 % example:
21 % X = lvb_readstr(4,2);
22 %   This attempts to read two strings from the file with an identifier of
23 %   4. The strings are then returned as a 1 by 2 cell vector X.
24 %
25 %%%%%%%%%%%%%%%%%%%%%%%%%%%%%%%%%%%%%%
26 %
27 % initialize string array
28 strout{n} = [];
29
30 % for each string read the length (strlen), then read strlen chars
31 for i = 1:n
32     strlen = fread(fid,1,'*int32');           % length in bytes
33     strout{i} = fread(fid,strlen,'*char'); % read strlen chars
34 end
35
36 end

```

code/sal_mfb.m

```

1 function [xb, ca10, ca50, ca90] = sal_mfb(cyl_p, cyl_v, spk, varargin)
2 %%%%%%%%%%%%%%%%%%%%%%%%%%%%%%%%%%%%%%
3 %
4 %   sal_mfb - calculate burn curve based on cylinder pressure data %
5 %
6 %%%%%%%%%%%%%%%%%%%%%%%%%%%%%%%%%%%%%%

```

```

7 %
8 % sal_mfb - version 0.94 - Jake McKenzie - modified: 05/22/14
9 %
10 % inputs:
11 %   - cylinder pressure [bar]: pegged, crank angle resolved
12 %   - cylinder volume [m^3]: cylinder volume, crank angle resolved
13 %   - spk                  [cad]: angle at spark bTDCcomp
14 %   - mode                 [str]: fit/computation mode
15 %   - ivc                  [cad]: angle at intake valve closing aBDCcomp
16 %   - evo                  [cad]: angle at exhaust valve opens bBDCexch
17 %
18 % outputs:
19 %   - xb                  [1] : cumulative fraction of fuel burned
20 %   - ca10                [cad]: crank angle of 10% burn
21 %   - ca50                [cad]: crank angle of 50% burn
22 %   - ca90                [cad]: crank angle of 90% burn
23 %
24 % notes:
25 %   the end of fit should be earlier than both tdc and the start of
26 %   combustion. The start of combustion is often defined as spark timing
27 %   and the end of combustion may be defined as say 20 deg before exhaust
28 %   valve opening. Both cyl_p and cyl_v must contain one cycle (720 crank
29 %   angles) at any encoder resolution. All angles are measured aBDC
30 %   compression. Only one mode is currently supported.
31 %
32 %%%%%%%%%%%%%%%%%%%%%%%%%%%%%%%%%%%%%%
33 %
34 %% parameter defaults (used if they are not defined in function call) %%
35 %%%%%%%%%%%%%%%%%%%%%%%%%%%%%%%%%%%%%%
36 ivc_default = 40; % aBDC compression
37 evo_default = 20; % bBDC gas exchange
38 mode_default = 'default';
39
40 %% extract optional arguments %%
41 %%%%%%%%%%%%%%%%%%%%%%%%%%%%%%%%%%%%%%
42 narginchk(3,6);
43 switch nargin
44 case 4
45     ivc = ivc_default;
46     evo = evo_default;
47     mode = varargin{1};
48 case 5
49     ivc = varargin{2};
50     evo = evo_default;
51     mode = varargin{1};
52 case 6
53     ivc = varargin{2};
54     evo = varargin{3};
55     mode = varargin{1};
56 otherwise
57     ivc = ivc_default;
58     evo = evo_default;
59     mode = mode_default;
60 end
61
62 %% pre processing %%
63 %%%%%%%%%%%%%%%%%%%%%%%%%%%%%%%%%%%%%%
64
65 nsamp = length(cyl_p)/720;           % number of samples per cad
66 scfi = round(nsamp*(ivc+10));        % start of compression fit index
67 eefi = round(nsamp*(360-evo-10));    % end of expansion fit index
68 cyl_p = smooth(cyl_p,nsamp*3);       % smooth pressure trace (to remove knock)
69
70
71
72 %% locate start of combustion %%
73 %%%%%%%%%%%%%%%%%%%%%%%%%%%%%%%%%%%%%%
74
75 %% mode 'default' - search for start of combustion by fitting
76 ftln = nsamp*(180-spk)-scfi; % fit length (initial value)
77 ftinc = nsamp*2;              % fit increment
78 inbound = 1;

```

```

79
80 while(inbound)
81   [gamc, S] = polyfit(log10(cyl_v(scfi:scfi+ftln)),log10(cyl_p(scfi:scfi+ftln)),1);
82   [ft, delta] = polyval(gamc,log10(cyl_v(scfi+ftln:scfi+ftln+ftinc)),S);
83
84   if(max(abs(ft+2*delta) < abs(log10(cyl_p(scfi+ftln:scfi+ftln+ftinc)))) & (delta > 0.0025))
85     inbound = 0;
86   else
87     ftln = ftln+ftinc;
88   end
89 end
90 soci = scfi+ftln-nsamp*5; % padding of 5CA
91
92 %% mode 2 - start of combustion is spark
93 % soci = nsamp*(180-spk);
94 % game = polyfit(log10(cyl_v(scfi:soci)),log10(cyl_p(scfi:soci)),1);
95
96
97
98 %% debug plot
99 % figure.plot(log10(cyl_v(scfi:scfi+ftln)),log10(cyl_p(scfi:scfi+ftln)),'-k',...
100 %               log10(cyl_v(scfi+ftln:scfi+ftln+ftinc)),ft+2*delta,'-g',...
101 %               log10(cyl_v(scfi+ftln:scfi+ftln+ftinc)),ft+2*delta,'-g',...
102 %               log10(cyl_v(scfi+ftln:scfi+ftln+ftinc)),log10(cyl_p(scfi+ftln:scfi+ftln+ftinc)),'-r')
103
104
105 %% locate end of combustion %%
106 %%%%%%%%%%%%%%%%%%%%%%%%%%%%%%%%%%%%%%
107
108 %% mode 1 - search for end of combustion by fitting
109 % ftln = nsamp*30; % fit length (initial value)
110 % ftinc = nsamp*2; % fit increment
111 % inbound = 1;
112 %
113 % while(inbound)
114 %   [game, S] = qpolyfit(log10(cyl_v(eefi-ftln:eefi)),log10(cyl_p(eefi-ftln:eefi)),1);
115 %   [ft, delta] = polyval(game,log10(cyl_v(eefi-ftln-ftinc:eefi-ftln)),S);
116 %
117 %   if(ft+2*delta > log10(cyl_p(eefi-ftln-ftinc:eefi-ftln)) & (delta > 0.0025))
118 %     inbound = 0;
119 %   else
120 %     ftln = ftln+ftinc;
121 %   end
122 % end
123 % eoci = eefi-ftln+nsamp*10; % padding of 10CA
124
125
126 %% mode 2 - search for end of combustion at max of pV^1.15
127 [~, eoci] = max(cyl_p.*cyl_v.^1.15);
128 eoci = eoci+nsamp*20; %20 CAD padding
129 game = polyfit(log10(cyl_v(eoci:eefi)),log10(cyl_p(eoci:eefi)),1);
130
131 %% debug plot
132 % figure(1002).plot(log10(cyl_v(eefi-ftln:eefi)),log10(cyl_p(eefi-ftln:eefi)),'-k',...
133 %                     log10(cyl_v(eefi-ftln-ftinc:eefi-ftln)),ft+2*delta,'-g',...
134 %                     log10(cyl_v(eefi-ftln-ftinc:eefi-ftln)),ft+2*delta,'-g',...
135 %                     log10(cyl_v(eefi-ftln-ftinc:eefi-ftln)).log10(cyl_p(eefi-ftln-ftinc:eefi-ftln)),'-r')
136
137
138
139 %% calculate mass fraction burned - heywood pg. 385 %%
140 %%%%%%%%%%%%%%%%%%%%%%%%%%%%%%%%%%%%%%
141
142 gamma = linspace(-gamc(i),-game(i),length(cyl_p(soci:eoci)));
143 xb = zeros(size(cyl_p));
144 xbp = (cyl_p(soci:eoci).^(1./gamma).*cyl_v(soci:eoci)-cyl_p(soci).^(1./gamma)*cyl_v(soci))./...
145   (cyl_p(eoci).^(1./gamma)*cyl_v(eoci)-cyl_p(soci).^(1./gamma)*cyl_v(soci));
146 [~, i] = max(xbp);
147 xbp = xbp/xbp(i);
148
149 %% gamma iteration
150 gamma = -gamc(i) + (-game(i)+gamc(i))*xbp;

```

```

151 xb      = zeros(size(cyl_p));
152 xbp    = (cyl_p(soci:eoci).^(1./gamma).*cyl_v(soci:eoci)-cyl_p(soci).^(1./gamma)*cyl_v(soci))./...
153     (cyl_p(eoci).^(1./gamma)*cyl_v(eoci)-cyl_p(soci).^(1./gamma)*cyl_v(soci));
154 [-, i] = max(xbp);
155 xb(soci:soci+i-1) = xbp(1:i)/xbp(i);
156 xb(soci+i:end)    = 1;
157
158 %% find ca10, ca50 and ca90 using linear interpolation
159 ca10 = find((xb >= .10),1,'first');
160 ca50 = find((xb >= .50),1,'first');
161 ca90 = find((xb >= .90),1,'first');
162
163 ca10 = interp1(xb(ca10-1:ca10),[ca10-1, ca10],0.1)/nsamp;
164 ca50 = interp1(xb(ca50-1:ca50),[ca50-1, ca50],0.5)/nsamp;
165 ca90 = interp1(xb(ca90-1:ca90),[ca90-1, ca90],0.9)/nsamp;
166
167 %% warning output if burn duration is larger than 55 CA
168 % if((eoci-soci)/nsamp >= 65)
169 %     disp(['Warning: Combustion duration of ', num2str((eoci-soci)/nsamp), ' crank angles detected, could be erroneous']);
170 % figure(1003), hold on
171 % range = linspace((soci-1)/nsamp,(eoci-1)/nsamp,eoci-soci+1);
172 % [ax, h1, h2] = plotyy(range,cyl_p(soci:eoci),range,xb(soci:eoci));
173 % set(ax(2),'YLim',[0,1.25])
174 % plot([ca10,ca50,ca90],cyl_p([ca10,ca50,ca90]*nsamp+1),'or')
175 % hold off
176 % figure(1004),loglog(cyl_v,cyl_p,'-k',cyl_v([scfi,soci,eoci,eefi]),cyl_p([scfi,soci,eoci,eefi]),'or')
177 % end
178
179
180
181
182 %% diagnostic mode %%
183 %%%%%%%%%%%%%%%%%%%%%%%%%%%%%%%%%%%%%%
184 if strcmp(mode,'debug')
185     figure(999)
186     loglog(cyl_v,cyl_p,'-k'),cyl_v([scfi,soci,eoci,eefi]),cyl_p([scfi,soci,eoci,eefi]),'-or')
187
188 % mfb plot
189 figure(1000)
190 range = linspace((soci-1)/nsamp,(eoci-1)/nsamp,eoci-soci+1);
191 [ax, h1, h2] = plotyy(range,cyl_p(soci:eoci),range,xb(soci:eoci));
192 hold on
193 set(ax(2),'YLim',[0,1.25])
194 plot(round([ca10,ca50,ca90]),cyl_p(round([ca10,ca50,ca90])*nsamp+1),'or')
195 hold off
196
197 figure(1001)
198 hold on
199 plot(now-fix(now),(eoci-soci)/nsamp,'ok')
200 ylabel('Burn Duration, [CAD]')
201 hold off
202
203 pause
204 end
205
206 end

```

